



Norwegian University of
Science and Technology

Optimisation of Spray Pyrolysed $(\text{La}_{0.6}\text{Sr}_{0.4})_{0.99}\text{CoO}_3$ Cathodes for Solid Oxide Fuel Cells

Sigrud Sognli Høyem

Chemical Engineering and Biotechnology

Submission date: July 2016

Supervisor: Mari-Ann Einarsrud, IMTE

Co-supervisor: Guttorm Syvertsen-Wiig, CerPoTech AS

Norwegian University of Science and Technology
Department of Materials Science and Engineering

Declaration

I, Sigrid SOGNLI HØYEM, declare that the work presented in this document has been performed independently and in accordance with the rules and regulations of the Norwegian University of Science and Technology (NTNU).

Trondheim, 25 July 2016

Sigrid Sognli Høyem

Preface

This Master's thesis is submitted to the Norwegian University of Science and Technology (NTNU), as part of the requirements for the degree of Master of Science. The work presented here has been carried out at the Department of Materials Science and Engineering at NTNU between 4. February and 25. July 2016. Professor Mari-Ann Einarsrud has supervised the work, and Dr. Guttorm Syvertsen-Wiig has served as co-supervisor.

I would like to thank my supervisors for all the inspiration, help, and constructive feedback I received throughout the semester. I also want to thank Dr. Sophie Labonnote-Weber and MSc Leif Olav Jøsang at CerPoTech AS for answering any questions and being available for discussions related to my project. Additionally I would like to acknowledge the rest of my coworkers in the Inorganic Materials and Ceramics Research Group for the input on my presentations and results. A special thanks to Magnus Gryteselv for all feedback, and for keeping my spirit up. Finally, I would like to thank the technical staff at the department for equipment training and assistance.

Abstract

The effect of the precursor concentration and the concentration of citric acid (CA) on the properties of $(\text{La}_{0.6}\text{Sr}_{0.4})_{0.99}\text{CoO}_3$ (LSC), prepared by spray pyrolysis, has been studied. Precursor solutions with concentrations ranging from 67 to 222 g/L, and with CA:LSC ratios of 0.1, 0.5, and 1, were used to synthesise LSC powder. The samples were calcined at 750 °C for 6 hours, and subsequently milled for 48 hours. The powders were characterised by X-ray diffraction, scanning electron microscopy, thermogravimetric analysis, gas adsorption, and laser diffraction spectrometry.

The morphology of the as-prepared powders was found to vary with precursor concentration and amount of citric acid used. More evenly sized agglomerates, and thinner core shells were observed for powders produced from low concentration precursor solutions with high CA:LSC ratios.

Post calcination, all samples were found to be phase pure LSC with rhombohedral symmetry. The highest surface area, with a value of $21.2 \text{ m}^2\text{g}^{-1}$, was measured for the sample made from the precursor solution with the lowest concentration and highest CA:LSC ratio. The particle size distribution was found to be the most narrow for the high concentration sample with the highest CA:LSC ratio. This sample also had the lowest median particle size.

The crystallite size calculated from the XRD patterns varied from 42 to 45 nm. The particle size measured from SEM images had larger variations with the smallest value, 85 nm, measured for the sample from the high concentration batch with the lowest ratio of CA:LSC.

Symmetric cells with LSC cathodes on $\text{Ce}_{0.8}\text{Gd}_{0.2}\text{O}_2$ (CGO) electrolytes were fabricated by spray deposition and fired at various temperature programs. The deposited cathodes were uniform, with a thickness of 1-2 μm . A firing temperature of 800 °C with no annealing time was found to give good adhesion between cathode and electrolyte. The cell was analysed by electrochemical impedance spectroscopy in oxygen atmosphere at 600, 700, and 800 °C, and the area specific resistance was determined to 3.02, 1.27, and 0.32 Ωcm^2 respectively.

The results in this work indicate that LSC powders produced by spray pyrolysis are suitable as cathode materials for use in IT-solid oxide fuel cells.

Sammendrag

Effekten av variasjoner i forløperkonsentrasjoner og mengde tilsatt sitronsyre (CA) på egenskapene til $(\text{La}_{0.6}\text{Sr}_{0.4})_{0.99}\text{CoO}_3$ (LSC) pulver, produsert med spray pyrolyse, har blitt undersøkt. Forløperløsninger med konsentrasjoner mellom 67 og 222 g/L, og med CA:LSC ratioer 0.1, 0.5 og 1, ble brukt for å syntetisere LSC pulveret. Prøvene ble kalsinert ved 750 °C i 6 timer, og deretter malt i 48 timer. Pulveret ble karakterisert med røntgendiffraksjon, elektronmikroskop, termogravimetrisk analyse, gassadsorpsjon og laser diffraksjon.

Morfologien til det ubehandlede pulveret varierte med forløperkonsentrasjonen og mengden sitronsyre tilsatt. Jevnere agglomeratstørrelser og tynnere kjerneskill ble observert for pulver produsert fra løsningene med lavest konsentrasjon og høyeste mengde tilsatt sitronsyre.

Etter kalsinering bestod alle prøvene av faseren LSC med rhombohederisk symmetri. Det største overflatearealet, $21.2 \text{ m}^2\text{g}^{-1}$, ble målt for prøven produsert fra forløperen med lavest konsentrasjon og høyest CA:LSC ratio. Distribusjonen til partikkelstørrelsen var smalest, og hadde lavest median, for prøven laget av den høyeste forløperkonsentrasjonen, med størst tilsatt av sitronsyre.

Krystallitstørrelsen ble beregnet fra diffraksjonsmønstrene, og varierte mellom 42 og 45 nm. Partikkelstørrelsen bestemt fra SEM-bildene hadde større variasjoner. De minste partiklene ble målt til 85 nm for prøven laget fra en forløper med høy konsentrasjon og lav tilsatt av sitronsyre.

Symmetriske celler hvor en katode av LSC ble deponert på $\text{Ce}_{0.8}\text{Gd}_{0.2}\text{O}_2$ (CGO) elektrolytt ved spraying, ble brent på forskjellige temperaturprogram. Katodene var jevne og hadde en tykkelse på 1-2 μm . En temperatur på 800 °C uten holdetid, ble bestemt passende for å oppnå god heft mellom katode og elektrolytt. Den symmetriske cellen behandlet ved denne temperaturen ble analysert med elektrokjemisk impedansspektroskopi. Målinger ble utført ved 600, 700 og 800 °C, med oksygen som atmosfære, og den arealspesifikke motstanden ble bestemt til henholdsvis 3.02, 1.27 og 0.32 Ωcm^2 .

Resultatet indikerer at LSC-pulver, produsert med spray pyrolyse har høyt potensial som et katodematerial for bruk i brenselceller ved lave driftstemperaturer.

Contents

1	Background	1
1.1	Motivation	1
1.2	Aim of this work	2
2	Introduction	3
2.1	Solid oxide fuel cells	3
2.2	Strontium-doped lanthanum cobaltite	10
2.3	Gadolinium-doped ceria	15
2.4	Spray pyrolysis	16
2.5	Solution chemistry	19
3	Experimental	25
3.1	Preliminary investigations	25
3.2	Powder preparation	26
3.3	Samples	28
3.4	Powder characterisation	29
3.5	Preparation of symmetric cells	30
3.6	Characterisation of the symmetric cells	32
3.7	Electrochemical impedance spectroscopy	33
4	Results	35
4.1	Preliminary analysis	35
4.2	Powder appearance and yield	41
4.3	Weight loss of the as-prepared powder	42
4.4	Phase purity	43
4.5	Morphology	48
4.6	Specific surface area	51
4.7	Particle size calculations	52
4.8	Particle size distribution	53
4.9	Evaluation of milling procedure	54
4.10	Sintering kinetics	57
4.11	Characterisation of symmetric cells	58
4.12	Area specific resistance	63

5	Discussion	67
5.1	Phase purity	67
5.2	Yield and volume density	69
5.3	Morphology of the as-prepared powder	70
5.4	Particle size and surface area	71
5.5	Evaluation of airbrushing as a deposition method	73
5.6	Evaluation of firing temperature for symmetric cells	74
5.7	Area specific resistance	75
6	Concluding remarks and further work	77
6.1	Conclusion	77
6.2	Further work	78
	Bibliography	79
A	Element maps	85
B	Non-normalised Nyquist plots	89
C	Impedance data modelled by equivalent circuits	91

List of Abbreviations

EIS	Electrochemical Impedance Spectroscopy
LDS	Laser Diffraction Spectrometry
PSD	Particle Size Distribution
SEM	Scanning Electron Microscopy
SSA	Specific Surface Area
TGA	Thermo Gravimetric Analysis
XRD	X-Ray Diffraction
SOFC	Solid Oxide Fuel Cell
HT-SOFC	High Temperature-Solid Oxide Fuel Cell
IT-SOFC	Intermediate Temperature-Solid Oxide Fuel Cell
BSCF	Barium Strontium Cobalt Ferrite oxide
LCC	Lanthanum Calcium Cobalt oxide
LSC	Lanthanum Strontium Cobalt oxide
LSCF	Lanthanum Strontium Cobalt Ferrite oxide
LSGM	Lanthanum Strontium Gallium Manganite oxide
LSM	Lanthanum Strontium Manganite oxide
YSZ	Yttrium Stabilised Zirconia
ASR	Area Specific Resistance
MIEC	Mixed Electronic Ionic Conductor
TPB	Triple Phase Boundary

Chapter 1

Background

1.1 Motivation

One of the most important areas of research today is the improvement of energy production. This includes the development of more efficient technology, as well as a focus on the environmental issues related to our increasing energy consumption. The devices used to convert and store energy often consist of multiple complex components. The effectiveness of these devices is highly dependent on the chemical composition and structure of the materials used.

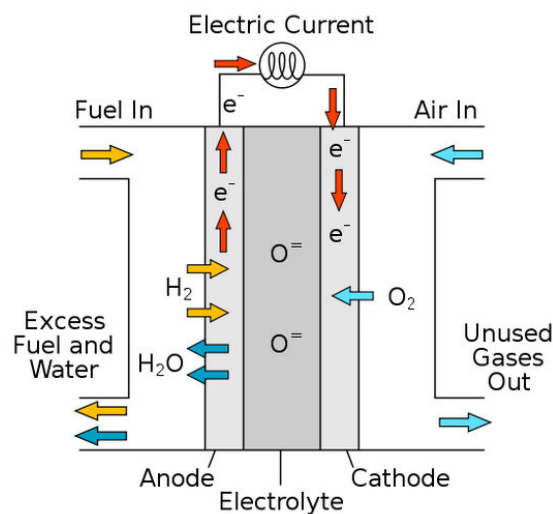


FIGURE 1.1: Schematic of a Solid-Oxide Fuel Cell.

The solid oxide fuel cell is an example of one of these technologies. It is a device where chemical energy is converted into electrical energy through a paired set of oxidation and reduction reactions. The fuel cell can be an entirely clean source of energy by utilising hydrogen gas as fuel. It can however also function as a transition device, relying on carbon based fuels until such a time as when this is no longer needed.

It is essential that the cell components keep their structural integrity and functional properties under the large variations in temperature experienced during production. The cathode, electrolyte, anode and interconnect of such a device must also be compatible with each other. As the components are produced using ceramic oxide powders, the properties of these powders have a vital effect on the resulting stability and efficiency of the individual components, and on the cell as a whole.^[1]

Wet chemical synthesis is a much used process that can be applied to a broad range of materials. This method offers good control and customisation of desired material properties and composition, and have advantages over solid state synthesis in this regard. Combining wet chemical synthesis with spray pyrolysis makes it possible to produce large amounts of powder in a continuous process, while still being able to use customised solutions.

The powders produced by spray pyrolysis consist of fine particles. However, due to the short residence time at elevated temperature, the particles are in most cases not fully reacted, and a high temperature heat treatment is needed to achieve a phase pure product. This heat treatment limits the production of nanoscale particles, as the higher temperatures induce particle growth. The ceramic oxide powders that are used in functional materials require small particles of a uniform distribution to achieve good material properties. This means that a subsequent milling step is necessary after heat treatment. Limiting the duration of these process steps, or avoiding them completely is preferable to lower production cost, and reduce the energy consumed during powder preparation.

Research has shown good effect on the resulting phase purity and particle morphology by the inclusion of simple organic complexing agents in the precursor solutions.^[2,3] These complexing agents increase the solubility of precursor solutions and prevent segregation during powder formation.

1.2 Aim of this work

The aim of this Master's thesis is to investigate the effect of the precursor concentration and the concentration of citric acid on the properties of $(\text{La}_{0.6}\text{Sr}_{0.4})_{0.99}\text{CoO}_3$ powders prepared by spray pyrolysis. The overall goal is to optimise the production parameters of the spray pyrolysis process to obtain a powder consisting of nanoscale particles with a large specific surface area. The particles should be of uniform morphology and have a homogeneous size distribution. The powders will be processed and tested for use as a cathode in solid oxide fuel cells. In addition, effects of variations in the precursor solution on phase purity, powder morphology, and surface area will be examined.

The thesis is a continuation of the author's specialisation project "Optimised microstructure of $\text{La}_{0.6}\text{Ca}_{0.4}\text{CoO}_3$ for solid oxide fuel cell cathodes",^[4] which was completed in December 2015.

Chapter 2

Introduction

2.1 Solid oxide fuel cells

Fuel cells have since they were discovered in 1839 by Sir William Grove^[5] had a promising potential for efficient power generation with a low environmental impact. It took over a hundred years before the understanding of solid electrolytes was sufficient to lead to the development of a solid oxide fuel cell (SOFC).^[6] Even though increased research in the area begun in the 1960s, it is first in recent years that SOFCs have reached the initial stages of commercialisation.^[7] This slow development can be attributed to issues related to stability, cost and complexity of production, operation, and maintenance, due to the high operating temperatures (800-1000 °C) needed for the current functional cells to be efficient.

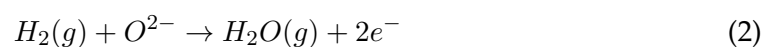
The high operating temperatures and associated issues concerning the mechanical and chemical stability of the components mean that the current cells are unable to compete with already existing technologies for energy production.^[1] To lower the cost and increase the efficiency and stability of the solid oxide fuel cell, research into possible materials for use in intermediate temperature (500-750 °C)^[8] solid oxide fuel cells (IT-SOFCs) are in focus.^[7,9,10]

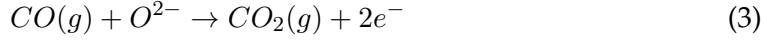
Operating principles

A solid-oxide fuel cell consists of a dense, oxide-ion conducting electrolyte sandwiched between an anode and a cathode, both of which are porous and connected to an external circuit, as can be seen in Figure 1.1. Fuel gas, in the form of pure hydrogen or carbon monoxide, is fed to the anode side, while air is fed to the cathode. Oxygen from the air is reduced at the cathode,

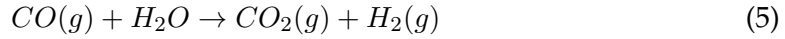
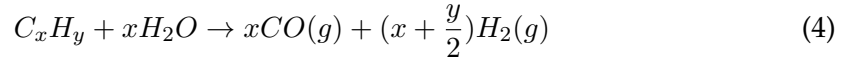


and the oxygen ions are transported through the electrolyte to the anode where the fuel is oxidised.





The electrons that are transferred through the outer circuit, from anode to cathode, can be forced to do work if an external load is connected. Due to the high operating temperature of regular SOFCs, other hydrocarbon gases, such as methane or propane, can be internally reformed through the steam reforming and the the water gas shift reactions,



This flexibility in choice of fuel, and the possibility for the SOFC to operate at high efficiency, converting abundant and cheap natural gas (and eventually hydrocarbons from biomass)^[11] to electricity, gives this technology a major advantage over other, low temperature technologies that lack this flexibility.^[10]

Cell design and general requirements

The most common designs for solid oxide fuel cells are the planar and tubular geometries, illustrated in Figure 2.1 (a) and (b) respectively. The tubular cell was designed by Siemens Westinghouse Power Corporation in the 1970s. Despite the different geometries, the cell components have similar material requirements for both designs. All components must have the required electronic and/or ionic conductivity to perform their individual cell functions. Target values for these properties for the electrolyte, anode and cathode are listed in Table 2.1.

TABLE 2.1: Ideal requirements for the oxygen diffusion coefficient, ionic conductivity, electronic conductivity, and porosity for the different components in a solid oxide fuel cell. Values gathered from various sources.^[7,10]

Component	Oxygen diffusion coefficient [cm ⁻² s ⁻¹]	Ionic conductivity [Scm ⁻¹]	Electronic conductivity [Scm ⁻¹]	Porosity [%]
Electrolyte	0	1 × 10 ⁻³	0	0
Anode	-	-	>100	20-40
Cathode	1 × 10 ⁻⁶	-	>100	30-40

Chemical and structural stability at high temperature is essential for all materials used in the cell. Additionally the components should have a matching thermal expansion coefficient to avoid delamination during production and operation. Finally, all materials should have a low reactivity with each other to ensure stability over time.^[9] These requirements are essential to ensure long cell life and to avoid degradation of the components during operation.

The illustrations in Figure 2.1 show one single cell, which provides power of the order of 1 W cm^{-2} . These individual modules are typically connected to form a fuel cell stack of adjustable size, depending on the power output required.^[12] This module based design makes fuel cells highly customisable, and possible to utilise for applications with various power requirements.

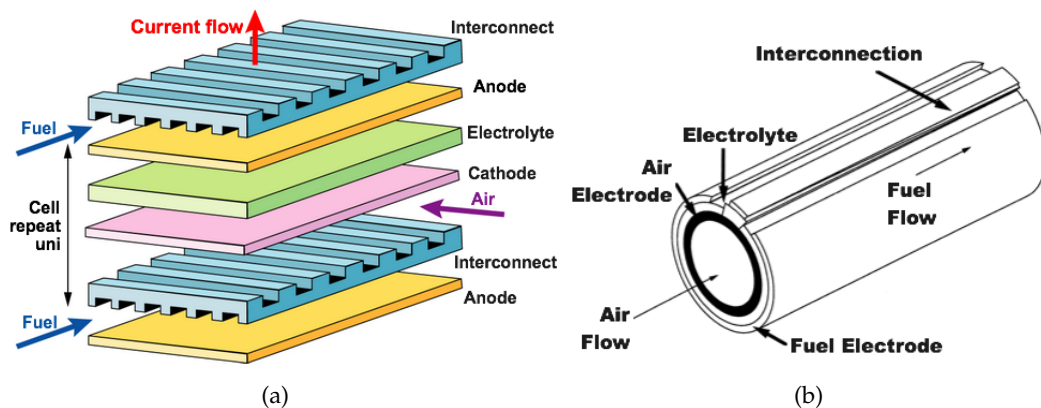


FIGURE 2.1: (a) Schematic of a planar Solid-Oxide Fuel Cell. Courtesy of University of Cambridge.^[13] (b) Tubular solid oxide fuel cell. Illustration from Singhal.^[9]

Two of the main loss mechanisms that limit cell efficiency are the resistivity of the components, and the polarisation effects due to poor electrocatalysis at interfaces. Minimising these losses is important to optimise fuel cells and can be done by addressing exchange kinetics, transport properties and microstructure.^[12]

Intermediate temperature solid oxide fuel cells

Where high temperature solid oxide fuel cells can be integrated with large scale, stationary gas turbines, very high efficiencies can be achieved. For smaller scale applications, a transition to intermediate temperature SOFCs is preferable due to the reduced costs of operation. A list of some advantages and disadvantages of both HT-SOFCs and IT-SOFCs can be seen in Table 2.2.

TABLE 2.2: Comparison of some advantages and disadvantages of high (HT) and intermediate (IT) temperature solid oxide fuel cells.^[7,10] The table is reprinted from Høyem.^[4]

Cell type	Advantages and Disadvantages
HT-SOFC	<ul style="list-style-type: none"> + No external reformer needed. + High conductivities in already established materials. + Compatible materials with matching thermal coefficients exist. + Faster reaction kinetics. + Lower ohmic resistances. - Material degradation. - Issues regarding stability of the cell. - Longer start-up time.
IT-SOFC	<ul style="list-style-type: none"> + Reduced system cost. + Expands choice of materials. + Reduced corrosion rates. + Possibilities to use metal interconnects for increased conductivity. + More rapid start-up and shut-down. + Improved durability. + Unlocks wider range of potential applications. + Less dependent on matching thermal expansion coefficient. - Lower conductivity. - Deactivation of catalysts. - External fuel processor needed to use hydrocarbons as fuel.

Electrolyte

The electrolyte should be fully dense and have a high ionic conductivity (over $1 \times 10^{-3} \text{ Scm}^{-1}$)^[10] so the oxygen ions can migrate from the cathode to the anode. It is also important that the material has a low electronic conductivity, to ensure that electrons can not pass through. Additionally, it is essential that there is no open porosity, to prevent diffusion of gas from one fuel stream to the other. An image of the typical microstructure of a SOFC is shown in Figure 2.2, where the high density of the electrolyte is clearly visible. Finally, since the electrolyte is exposed to both reducing and oxidising conditions, the material used should be chemically stable in both environments.

The fluorite oxides are a group of materials that have the required properties to be effective as an electrolyte. Out of these yttrium stabilised zirconia (YSZ) is the most widely used.^[7] The inclusion of yttrium stabilises the cubic phase of zirconia at high temperatures, which generates oxygen vacancies. The material does however require very high operating temperatures ($\geq 800 \text{ }^\circ\text{C}$) to achieve a sufficient ionic conductivity.

The need for such high temperatures can be partly countered by developing application methods for very thin, uniform electrolyte films of 10 μm or less. Other possible electrolytes include Gd-doped ceria^[14] (CGO), or Sr- and Mg-doped LaGaO_3 ^[15] (LSGM). Both of these are options for IT-SOFCs due to their relatively high oxide ion conductivity at temperatures in the 400-600 $^\circ\text{C}$ range. Values for the ionic conductivities of the mentioned materials are listed in Table 2.3.

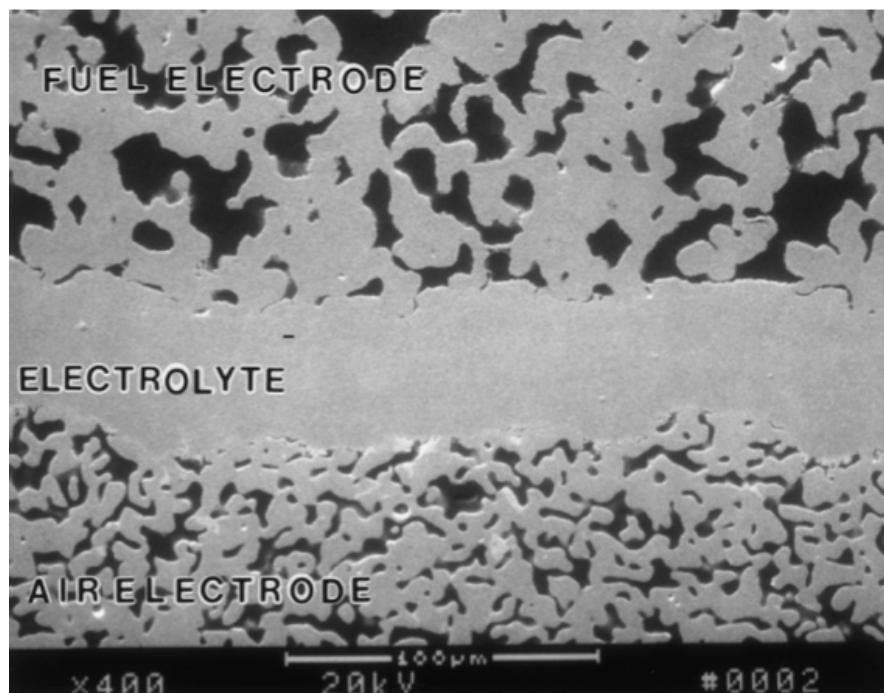


FIGURE 2.2: Microstructure of cross section of a Siemens Westinghouse solid oxide fuel cell. The porosity of the electrodes and the density of the electrolyte is clearly visible. Illustration from Singhal.^[9]

Anode

The anode should be stable in a reducing environment, have high mechanical stability, and have good electronic conductivity ($\geq 100 \text{ Scm}^{-1}$)^[10]. Additionally, sufficient porosity to allow transport of the fuel gas to, and transport of the product away from the interface, is necessary. The mechanical stability is critical, as the most common cell designs are anode-supported.

The reducing conditions and the demand for high electronic conductivity permits metals, for instance nickel, to be used as anodes. However, there is a large mismatch in thermal expansion between a metal and the commonly used electrolytes. To reduce

this mismatch, but retain the properties of nickel, it is possible to utilise a composite of the electrolyte material and the metal.^[9] For this cermet to function as an anode, it must have an optimised microstructure of connected metal particles to ensure electronic conduction through the matrix. Additionally the microstructure should maximise the area of the active triple phase boundary (TPB).^[10] As the illustration of the TPB region shown in Figure 2.3 illustrates, the TPB is the region where the electrolyte, electrode and fuel gas meet, and is the electrochemically active region of the cell.

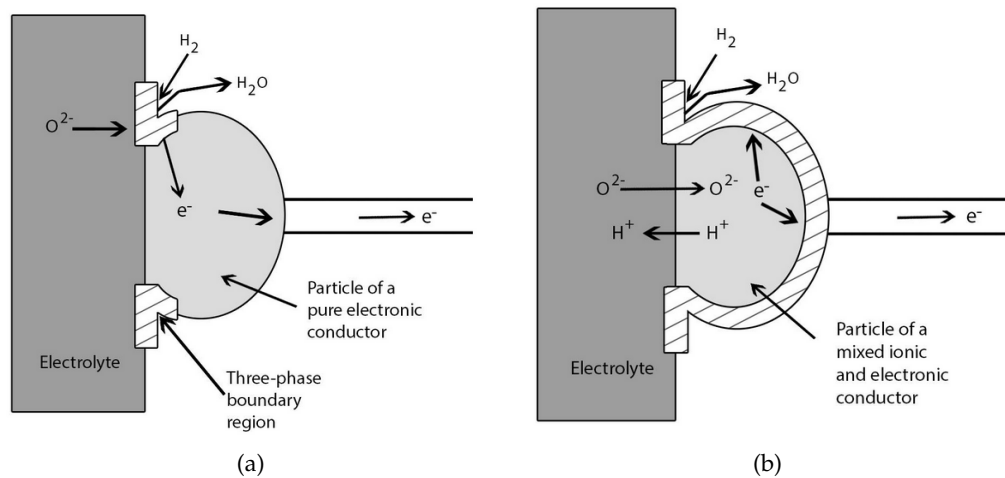


FIGURE 2.3: The triple phase boundary for (a) an electronic conductor, and (b) a mixed ionic electronic conductor. Illustration adapted from Larminie.^[16]

Using a cermet solves many of the initial problems related to the use of metal in anodes. However, there are still issues connected to the coarsening of nickel at high temperatures, which in turn degrades the anode during cell operation. There also exist some problems caused by carbon deposition and sulphur poisoning due to the internal reforming of hydrocarbons in high temperature SOFCs.^[7] Despite these issues, the Ni-YSZ cermet is the current anode choice for IT-SOFCs, although some perovskite structured oxides are under investigation as possible alternatives.^[17]

Cathode

Potential material candidates for use as cathodes in SOFCs need to be good electronic conductors, ideally with a conductivity above 100 Scm^{-1} and oxygen diffusion coefficients above $10^{-6} \text{ cm}^2\text{s}^{-1}$.^[7] It is also essential that the materials are stable under oxidising conditions. Many good materials have been found to make high temperature cells that are efficient. However, most of these materials experience a significant increase in electrochemical resistance as the temperature decreases. One of the reasons

for the higher cell resistance is that the electrode polarisation resistance on the cathode side, increases at lower temperatures.

To overcome problems related to this increase in resistance, investigations are being made into the possible use of mixed ionic and electronic conductors (MIECs) as cathode materials.^[1] Fabricating cathodes from MIECs would extend the active oxygen reduction site to include the entire exposed cathode surface, rather than being limited to the triple phase boundary where the cathode and gas meets the electrolyte, as illustrated in Figure 2.3.

TABLE 2.3: Overview of the properties of commonly investigated materials for SOFCs. All values are for temperatures of approximately 600 °C, except for the one marked with an asterisk, which shows the ionic conductivity of YSZ at 1000 °C. It is important to note that the values are highly on the synthesis route and resulting microstructure of the materials investigated. The table is modified from Høyem.^[4]

Material	Oxygen diffusion coefficient [cm ⁻² s ⁻¹]	Ionic conductivity [Scm ⁻¹]	Electronic conductivity [Scm ⁻¹]	Thermal Expansion coefficient [K ⁻¹]	Reference
Conventional materials					
8 mol% YSZ	1×10^{-6}	0.1 *	-	10.5×10^{-6}	[20, 21]
Ni-YSZ	1×10^{-6}	-	~ 4000	$\sim 12.0 \times 10^{-6}$	[22]
LSM	5×10^{-18}	-	120-130	12.0×10^{-6}	[23–25]
Electrolyte alternatives					
LSGM	-	0.03	-	12.2×10^{-6}	[26, 27]
CGO	-	6.7×10^{-2}	-	13.5×10^{-6}	[14]
Cathode alternatives					
LSCF	1.7×10^{-10}	-	300-330	15.3×10^{-6}	[28–30]
BSCF	3.3×10^{-7}	-	30-35	24×10^{-6}	[31–33]
LCC	-	-	~ 1000	19.5×10^{-6}	[20, 34]
LSC	2×10^{-9}	-	1300-1800	21.3×10^{-6}	[25, 35–37]

As for all other components used in SOFCs, the electrochemical performance will depend on the microstructure of the cathode. This in turn depends on the properties of the starting powders, as the morphology of the starting powder has a direct effect on the porosity and active surface area of the final component. In order to increase cathode efficiency, it therefore becomes essential to optimise the synthesis routes and morphology of the ceramic powders to be used in cathodes. The lowest polarisation resistances can be obtained using nanoscale grains with large surface areas.^[18,19]

Lanthanum manganite doped with alkaline or rare earth elements is the most commonly used cathode material. This group of materials has high electronic conductivity due to electron-hole hopping between the valence states of Mn, enhanced by doping with divalent ions.^[9] For high temperature SOFCs, (La,Sr)MnO_{3-δ} (LSM) is considered to be the state of the art cathode, due to its excellent conductive properties, good thermal stability and compatibility with the YSZ electrolyte. LSM does however experience the typical increase in polarisation resistance at lower temperatures, as mentioned previously, and is therefore unsuited for use as a cathode in an IT-SOFC.^[7]

A study by Teraoka^[38] investigated a wide range of lanthanum-doped cobaltites of composition La_{0.6}A_{0.4}Co_{0.8}B_{0.2}O_{3-δ}, and this class of material has since been heavily focused when searching for new potential cathodes for IT-SOFCs. One suggested substitution for LSM is the cobaltite analog, (La,Sr)CoO_{3-δ} (LSC). A material with a reported polarisation resistance as low as 0.023 Ω cm² at a temperature of 600 °C.^[39] However this material has some issues regarding its high thermal expansion coefficient and its reactivity with YSZ, and should therefore be investigated in combination with other possible electrolytes.

Other options for cathodes include various compositions of La_{1-x}Sr_xCo_{1-y}Fe_yO_{3-δ} (LSCF) and Ba_{1-x}Sr_xCo_{1-y}Fe_yO_{3-δ} (BSCF), where La is replaced by Ba.^[7] However, both materials experience some issues related to the use of Sr as a dopant, due to its tendency for surface segregation. This segregation results in a deactivation of the active sites for the oxygen reduction reaction, which causes increased cathode resistance.

The values for the required properties of some of the potential cathode materials are listed in Table 2.3, together with the corresponding values for the electrolyte and anode commonly used in IT-SOFCs to give a complete picture.

2.2 Strontium-doped lanthanum cobaltite

Perovskites have long been the most widely used cathode materials for SOFCs. The crystal structure of the general ABO_{3-δ} cubic unit cell can be seen in Figure 2.4, where the 12-fold coordination of the A cation with oxygen anions is seen in (a), while the 6-fold coordination of the B cation is illustrated in (b).

The perovskite structure is highly flexible, and can be customised by substituting a varying degree of one or both cations. The stability and structure of the crystal lattice varies with relative sizes of the cations as well as the degree of doping. This relationship is described by the Goldschmidt tolerance factor,

$$\tau = \frac{(r_A + r_O)}{\sqrt{2}(r_B + r_O)} \quad (6)$$

where r_x ($x = A, B, O$) is the ionic radii of atoms at the respective sites. A structure that has a tolerance factor of 1 is ideal, and the cubic perovskite is considered stable between values of 0.9 and 1.0.^[40]

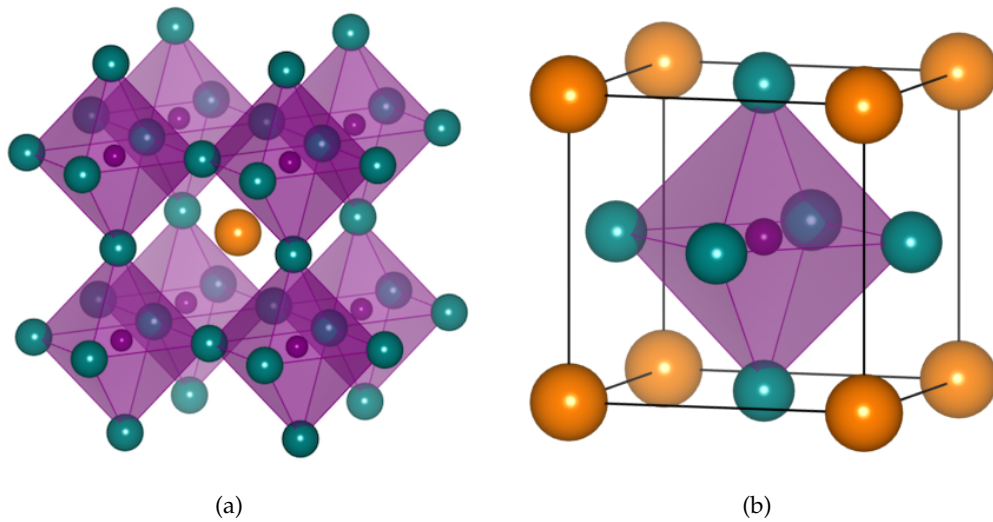


FIGURE 2.4: The cubic $ABO_{3-\delta}$ perovskite structure with space group $Pm\bar{3}m$. (a) Focused on the A-site. (b) Focused on the B-site. The green atoms are oxygen, the purple cobalt and the orange either lanthanum or strontium. Illustrations are created using the Vesta software.^[41]

The doped composition's tolerance factor can help indicate when the strain caused by the difference in ionic radii leads to distortions of the cubic structure. The crystal lattice will try to oppose the strain caused by cation substitution by tilting the corner shared oxygen octahedra (visible in Figure 2.4) causing a distortion or elongation of the lattice. The distorted structures most commonly have an orthorhombic or a rhombohedral symmetry at ambient temperature, but transform to the cubic structure at high temperatures.^[42]

In addition to distortions of the lattice caused by differences in ion size, defects in the structure can occur when there is a deficiency of cations or anions. Of these, oxygen vacancies are the most common and are generally introduced when the dopant cations have a different valency than those in the base structure. Due to electroneutrality concerns, doping with aliovalent cations at the A-site may also cause a change in valence state of the B-site cation. The change in valence can greatly affect the material's magnetic and electrical properties.^[42]

Crystal structure and the effect of doping

As mentioned previously, various doped $\text{LaCoO}_{3-\delta}$ based perovskites are being investigated for use as cathodes in IT-SOFCs due to their promising properties. As highly customisable MIECs, the substitution of cations makes it possible to tailor both the electronic and ionic conductivity, as well as the mechanical and thermal stability of the materials in this group.^[7,40]

At elevated temperatures, $\text{La}_{1-x}\text{A}_x\text{CoO}_{3-\delta}$ with $\text{A} = \text{Sr}^{2+}$ or Ca^{2+} has the ideal cubic perovskite structure with space group $Pm\bar{3}m$, as illustrated in Figure 2.4. At lower temperatures the structure undergoes a phase transition to the rhombohedral structure with space group $R\bar{3}c$, illustrated in Figure 2.5, due to a tilting of the CoO_6 -octahedra. Mastin et al.^[43] found that this transition temperature lowers with an increasing degree of doping. Their findings are reported in the phase diagram for the $\text{La}_{1-x}\text{Sr}_x\text{CoO}_{3-\delta}$ -system in Figure 2.6.

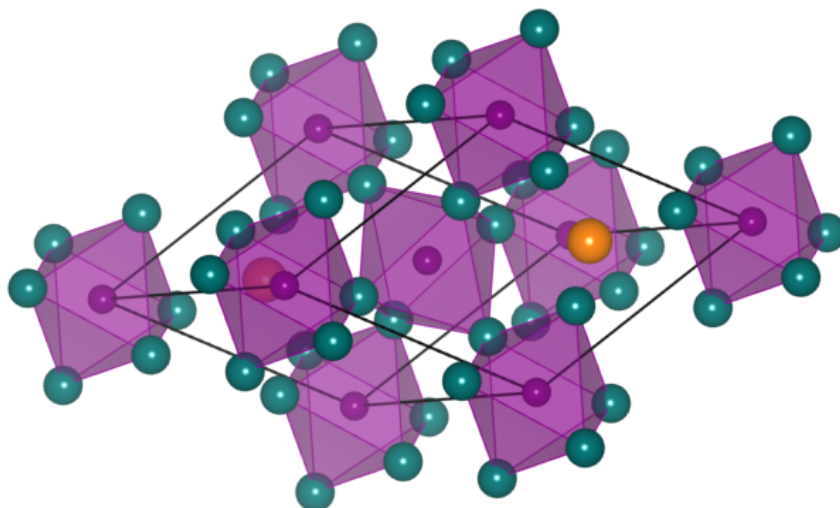


FIGURE 2.5: The rhombohedral $\text{La}_{1-x}\text{Sr}_x\text{CoO}_{3-\delta}$ crystal structure, with space group $R\bar{3}c$. The green atoms are oxygen, the purple cobalt and the orange either lanthanum or strontium. Illustration is created using the Vesta software.^[41]

The substitution of La^{3+} (ionic radii 1.36 Å) by smaller amounts of the divalent ions Sr^{2+} or Ca^{2+} (ionic radii 1.44 Å and 1.33 Å respectively)^[44] does not cause a phase transition, and is mainly compensated by the creation of oxygen vacancies in the LaCoO_3 lattice, or by a change in the valence state of cobalt from Co^{3+} to Co^{4+} . The latter is most predominant for $x \leq 0.3$, while the formation of oxygen vacancies becomes more favourable with increasing degree of doping.

The Goldschmidt tolerance factor for LSC increases gradually from 0.987 for $x = 0$, to 1.015 for $x = 0.5$ because of the large difference in ionic radii of Sr^{2+} and La^{3+} .^[43]

The combined effect of the differences in ion size and the creation of oxygen vacancies pushes the rhombohedral structure toward the cubic. And as indicated in the phase diagram in Figure 2.6, $\text{La}_{1-x}\text{Sr}_x\text{CoO}_{3-\delta}$ (LSC) transitions from the rhombohedral structure towards a cubic structure at ambient temperatures when the degree of doping reaches $x > 0.55$.

Properties and the potential of LSC as a cathode

Material properties are highly dependent on synthesis routes and resulting particle size. This relationship was investigated by Kumar et al.^[45] for various doped lanthanum-based oxides, including $\text{La}_{0.90}\text{Sr}_{0.10}\text{CoO}_{2.95}$, prepared using different wet chemical routes. Other relevant investigations of LSC include the performance of flame-made nanoscale $\text{La}_{0.6}\text{Sr}_{0.4}\text{CoO}_{3-\delta}$ by Heel et al.^[46], and the investigation of mechanical properties conducted by Orlovskaya et al.^[47]

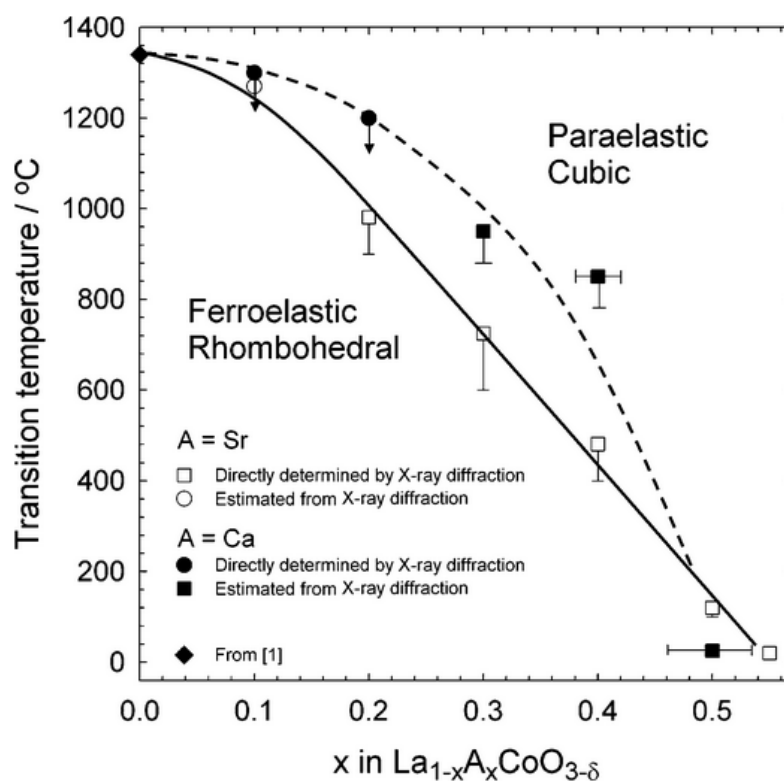


FIGURE 2.6: Phase diagram of the $\text{La}_{1-x}\text{Sr}_x\text{CoO}_{3-\delta}$ system, as reported by Mastin et al.^[43] The phase diagram for $\text{La}_{1-x}\text{Ca}_x\text{CoO}_{3-\delta}$ is shown in comparison.^[34]

The thermal expansion and electronic conductivity of LSC are listed in Table 2.3. As a Mixed ionic and electronic conductor, LSC has high enough electronic and ionic conductivity to function as a cathode, however, the thermal expansion coefficient is much larger than the reported values for that of the standard YSZ electrolyte, (10.5×10^{-6}).^[21] Additionally, previous investigations of LSC-cathodes indicate that lanthanum reacts with the YSZ electrolyte, leading to the formation of insulating phases which limit the efficiency of the cell.^[7] The lower operating temperatures of IT-SOFCs reduces the reactivity somewhat, but the mismatch in thermal expansion still makes LSC problematic to use with the most common electrolytes due to delamination and layer cracking.^[48]

When comparing LSC to the other candidates for use as cathodes in IT-SOFCs, mentioned in Section 2.1, some important points stand out; LSC has been reported to have better catalytic properties than LSCF. Additionally, no reports of degradation of the cathode due to carbonate formation when CO_2 is present in air, as is the issue with BSCF.^[49] The same resistance to degradation of the cathode was reported by Heel et al.^[46], who investigated flame-made nanoscale $\text{La}_{0.6}\text{Sr}_{0.4}\text{CoO}_{3-\delta}$. They found no evidence for the formation of carbonate, even in 5% CO_2 -containing atmosphere. Their investigations also looked at the formation of the insulating secondary phases; SrZrO_3 and $\text{La}_2\text{Zr}_2\text{O}_7$, when LSC was used in combination with YSZ, and found that the synthesis route of the LSC powder appeared to have an effect on the amount of undesired phase that formed.

Due to the strong tendency for secondary phase formation with YSZ, various research has investigated the chemical compatibility of lanthanum based cathodes with CGO electrolytes, or with CGO as a barrier layer.^[50] Li et al.^[51] reports of the mutual diffusion of cations across the interface of the LSCF cathode and the CGO electrolyte. Their results indicate that all cations diffuse into adjacent grains and substitute for each other, forming a solid solution between the two materials. The length of diffusion appears similar for all cations and the width of the diffusion zone seems to increase with increasing sintering temperature. This mutual diffusion can potentially have a negative effect on fuel cell performance due to formation of superstructures at the interface. It is reasonable to expect similar behaviour at LSC/CGO interfaces.

Compatibility with gadolinium-doped ceria electrolytes

Hayd et al.^[49] investigated the properties of $\text{La}_{0.6}\text{Sr}_{0.4}\text{CoO}_{3-\delta}$ thin films on electrolyte pellets of the composition $\text{Ce}_{0.90}\text{Gd}_{0.10}\text{O}_{1.95}$. The symmetric cells were heat treated at different temperatures, heating rates and annealing times, and the differences in resulting microstructure was related to the cathode effectiveness. They found that the cathode with the smallest grain size and highest porosity had the lowest value for area specific polarisation resistance (ASR) measured at 600 °C. The relationship between grain size/porosity and measured ASR, indicates that the operation temperature for the cell should be kept below temperatures that cause coarsening of the microstructure.

An overview of ASR values measured in air for CGO/LSC symmetric cells are

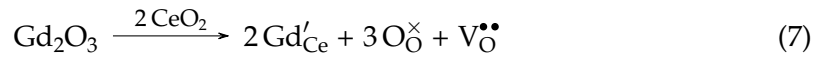
listed in table 2.4. The electrolytes are of the composition $\text{Ce}_{0.90}\text{Gd}_{0.10}\text{O}_{1.95}$ and are sandwiched between cathodes of the composition $\text{La}_{0.6}\text{Sr}_{0.4}\text{CoO}_{3-\delta}$. The values were collected from various sources and the different methods and conditions employed are included to give an indication of the ASR that can be expected for this type of cell.

TABLE 2.4: Overview of the area specific resistances for $\text{La}_{0.6}\text{Sr}_{0.4}\text{CoO}_{3-\delta}$ cathodes on $\text{Ce}_{0.90}\text{Gd}_{0.10}\text{O}_{1.95}$ electrolytes reported by various sources.

Cathode application	Sintering program	Electrolyte thickness [mm]	ASR [Ωcm^2]			Reference
			Measuring temperature	600 °C	700 °C	
Spray deposition	950 °C, 2 h	0.2	-	0.17	0.07	[52]
Screen printed	900 °C	1.5	0.96	0.14	-	[46]
Dip coating	700 °C, 0 h	0.8	0.023	-	-	[49]

2.3 Gadolinium-doped ceria

$\text{CeO}_{2-\delta}$ crystallises in the cubic fluorite structure as illustrated in Figure 2.7. Doping ceria with Gd causes small distortions of the lattice due to the difference in ionic radii of Gd^{3+} (1.053 Å) and Ce^{4+} (0.97 Å)^[44]. The doping additionally leads to the creation of oxygen vacancies following the reaction;



The created oxygen vacancies make it possible for O^{2-} to diffuse through the vacant sites, giving CGO good ionic conductivity, also in the lower temperature ranges.^[14] This makes CGO a good alternative for use as an electrolyte below temperatures where the conductivity of YSZ drops. The oxygen ion conductivity in CGO depends on the the degree of doping, the concentration of oxygen vacancies, and the microstructure of the fabricated electrolyte.

There are contradictory reports on which degree of doping results in the optimal electrolyte. Steele et al.^[14] report the highest conductivity (10^{-2}Scm^{-1} , at 500 °C) for 10% doping with Gd, while Anjaneya et al.^[53] found that 20% Gd-doping exhibit almost the same conductivity as 10%-Gd doping at lower temperatures (200-350 °C). The reports on the effect of microstructure and grain size have similar conflicting results. However, a systematic investigation by Lenka et al.^[54] indicate that a decrease in grain size gives decreased bulk conductivity while grain boundary conductivity increases. Due to the temperature dependence of the different types conductivity, they concluded

that for low temperature applications, a fine grain size leads to an increase in the total conductivity.

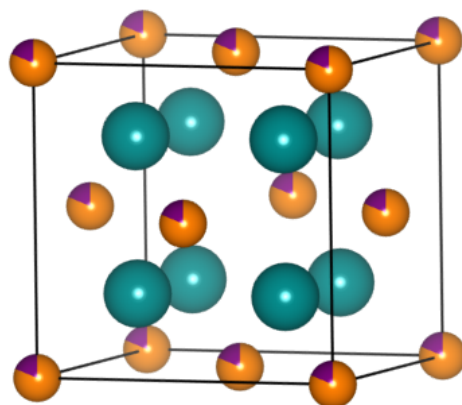


FIGURE 2.7: The cubic $\text{Ce}_{1-x}\text{Gd}_x\text{O}_{2-\delta}$ crystal structure, with space group $Fm\bar{3}m$. The green atoms are oxygen, the purple indicates gadolinium, and the orange cerium. Illustration is created using the Vesta software.^[41]

2.4 Spray pyrolysis

The term spray pyrolysis refers to multiple different aerosol techniques. Common for these techniques is the excellent control over chemical and physical properties that is gained through solution-based preparation methods. Producing ceramic powders using spray pyrolysis can also negate some of the disadvantages of post production heat-treatment and the consequent milling that is common for other solution-based synthesis methods, by integrating these into one continuous process. These advantages makes spray pyrolysis a method well suited for large scale production of well-defined ceramic powders.^[55]

Production process

An illustration of the spray pyrolysis apparatus is shown in Figure 2.8. The apparatus consists of a nozzle at the end of a lance inserted into the furnace tube. The nozzle atomises a cation precursor solution, creating aerosol droplets of the solvent. The droplets undergo evaporation, and subsequent thermolysis and coarsening (these steps are explained in detail below), as they are transported on the air carrier gas through the furnace tube. The powder is then collected in a cyclone situated at the end of the furnace.

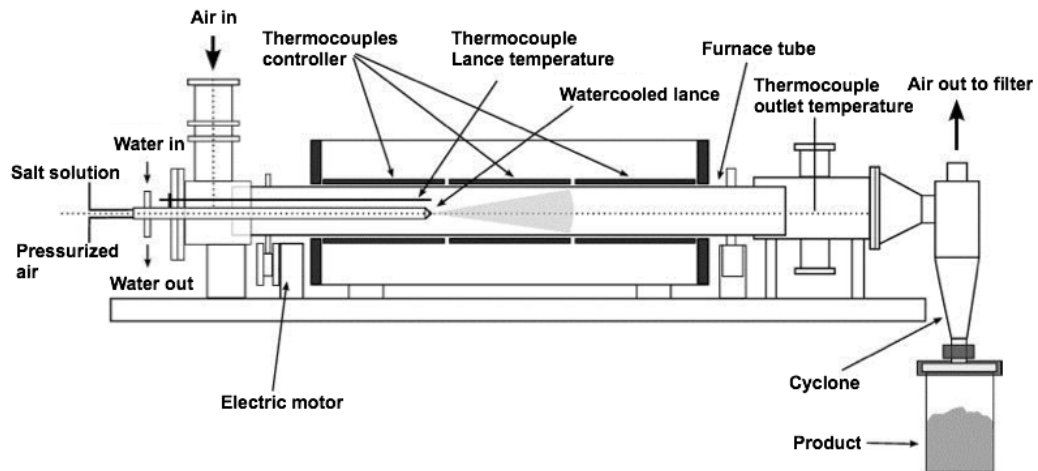


FIGURE 2.8: Illustration of a typical spray pyrolysis apparatus. Illustration borrowed from Moen.^[56]

Atomisation of the precursor

The spray pyrolysis process begins with the atomisation of a precursor solution by subjecting it to a force larger than the solution's surface tension. This is typically done by pressurising the solution through a nozzle. The type of nozzle used affects the droplet size, size distribution, and exit velocity, as well as the minimum and maximum throughput. Additionally, the surface tension, viscosity and density of the precursor, all affect the heating rate and residence time of the droplet through the furnace. This subsequently has an effect on the properties of the final product. For powders to be used in functional ceramic applications, the aim is to produce one particle per droplet. To accomplish this, the employed atomisers should produce small droplets at large quantities with low exit velocities.

Evaporation of the solvent

The atomised solvent is then transported through the furnace by a carrier gas. The high temperature in the furnace causes rapid evaporation of the solvent, while the droplet undergoes multiple simultaneous physical processes that affect particle morphology. These processes include evaporation of the solvent from the droplet surface, shrinkage of the droplet, change in droplet temperature, diffusion of solvent vapours away from the droplet, and diffusion of solute toward the centre of the droplet.

Messing et al.^[55] has summarised experimental data to determine which of these phenomena dominates the resulting particle morphology. They found that the two dominating mechanisms for particle formation depend on the solute concentration at

the centre of the drop. Surface precipitation occurs when the concentration at the centre of the drop is lower than the equilibrium saturation while the concentration at the surface is higher. In contrast, volume precipitation will be catalysed by nucleation at the surface when the concentration at the centre of the drop is equal to or larger than the equilibrium saturation. See Figure 2.9 for an illustration of the precipitation mechanisms.

Thermolysis and sintering

After precipitation the formed particles go through a thermolysis stage where the high temperature ceramic phase forms. The most common design for spray pyrolysis systems is to have one long, tubular chamber where the thermolysis and sintering processes overlap with evaporation stage. Ideally these processes should be separated into different reactors, to increase control of the production parameters. A single chambered furnace has low residence times, and it is therefore common for the precipitates to not have time to fully decompose. Because of this, the reaction to form the expected product might not be complete. Additionally, the collected powder might still contain carbonates formed by reactions with organic additives present in the precursor. This incomplete reaction makes additional heat treatments necessary post spraying to achieve a fully reacted, phase pure product.

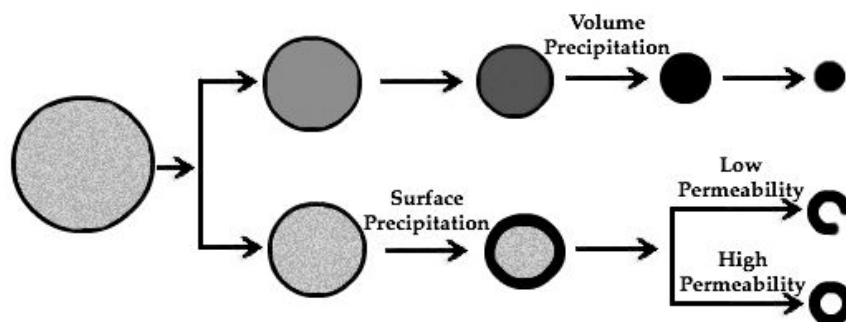


FIGURE 2.9: Illustration of surface and volume precipitation during the evaporation step of the spray pyrolysis process. Adapted from Messing et al.^[55]

Precursor solutions and the role of organic additives

An aqueous solution of metal salts is the most commonly used precursor for spray pyrolysis due to the large number of water-soluble metal salts available. Additional advantages are low cost, safety, and the ease of handling connected to the use of water-based solutions. To increase yield it is important that the metal salt has a high solubility. It is also important to evaluate the effect any impurities introduced with the metal salt

can have on the final product, as carbonates, nitrates, and other undesired contaminations might be present in the as-prepared powders.^[55]

For multicomponent systems the differences in solubilities of the metal salts might cause segregation which alters the composition of the precursor. This will in turn affect the formation of a phase pure product during thermolysis. To ensure that the desired composition is achieved, it is therefore essential to avoid segregation and keep all cations in a stable solution until the spraying is complete. This can be done by mixing the precursor of metal salts with various complexing agents. The complexing agents bind the cations in three dimensional networks and increases the individual cation's solubility. Additionally, the presence of a complexing agent might lead to a rapid increase in the solution viscosity during heating. The total effect of the complexation should ensure preservation of the homogeneity and prevent cation segregation during powder production.^[1] A more detailed explanation of complexation chemistry is given in Section 2.5.

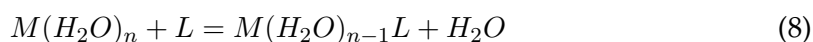
It is important to note that the addition of complexing agents to the precursor solution can affect the thermolysis as well. A large concentration of organics in the precursor will increase the temperature in the furnace and cause rapid gas evolution inside the droplets. The presence of CO₂ inside the furnace will increase as the organic compounds combust. This might in turn lead to an increased formation of carbonates, suppress decomposition of the nitrates, and affect the morphology of the particles.

2.5 Solution chemistry

As mentioned in the previous section, the solubility of cations in the precursor solution will affect the formation of the product during the thermolysis step of spray pyrolysis. To obtain the desired phase pure composition it is therefore essential to limit the segregation of cations during production. The following section explains the chemistry behind aqueous solutions and the complexation of metal ions, and is meant to give an understanding of how to prevent this unwanted segregation.

Complexation of an aqueous solution

In aqueous solutions containing metal salts, the metal cations will spread out and become surrounded by solvent molecules. The solvent molecules form bonds of varying strength with the central ion. To form different metal complexes, these solvent groups are replaced according to the following equation,



where M is the metal ion and L is the complexing ligand. The cation complex is formed by a Lewis acid-base interaction, where the ligand functions as a Lewis base, donating one or more of its electron pairs to the metal ion (a Lewis acid).^[57] The number

of ligands that can bind to the central ion corresponds to the coordination number for that specific metal ion. Ligands are classified as unidentate or multidentate depending on the number of donor sites they have. The multidentate ligands can form chelates, which are ring structures in which the cation is bound at several sites to the same ligand.^[57] Multidentate ligands that bind to the same cation through multiple sites will displace multiple water molecules (see Equation 8) and are highly entropy favoured. After one bond has formed, the remaining sites are closer to, and more likely to bind to the same cation, making chelates kinetically favoured as well. These types of ligands commonly have higher formation constants than their unidentate counterparts.

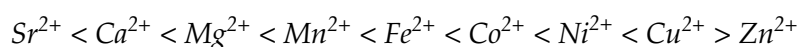
Classification of the ions

The compatibility between the ligand and the metal ion is another factor that determines the stability of the formed complex. This depends on the charge and size of the cations, as well as on the presence of a dipole in the ligand molecule. Schwarzenbach^[58] classified the complexation of various metal ions into three groups;

For strontium and the other alkaline earth metals, belonging to group A, the charge of the ions are the dominant factor for their behaviour. This is explained by the predominantly ionic bonds formed by the members of this group. A general rule for this group is that the tendency to form stable complexes decreases with increasing size of the ions. This rule does have some important exceptions, as when the anion ligands are large, the smaller cations form more stable complexes.^[59]

The second group, group B, consist of cations with completely filled d-subshells. The covalent nature of the bonds causes the strength of the complex to increase, not with the size and charge of the cation, but with the difference in electronegativities between ligand and cation.

Transition metal ions with incomplete d-shells can belong to either group. The stability of the complex increases according to the Irving Williams series (from Mn^{2+} to Zn^{2+}), as shown below. The stability increases as the size of the ion decreases. Note that the formation constants are relatively insensitive to choice of ligands.^[57]



Another important factor for the stability of the metal complex is the behaviour of the ligand itself. Even though the reactions are considered Lewis acid-base reactions, the stability of the complex doesn't show a clear correlation with the strength of the base. It appears that the stability mainly depends on the structure of the ligand and on the nature of the donor atom. Entropy factors are dominant for ionic bonds formed by oxygen donor atoms, whereas the covalent bonds that form with nitrogen atoms are dominated by enthalpy factors.^[59]

Complexing agents

Schwarzenbach indicated that the general trend is for multidentate ligands to be the strongest complexing agents as they form stable chelates. The most effective of these are in turn the ones that contain both oxygen and nitrogen donor atoms. EDTA is a prime example of a very strong complexing agent, and the chemical structure is illustrated and compared with citric acid in Figure 2.10. It is important to note that other factors than the type of donor site might affect bonding as well. These factors include; issues due to steric repulsion, a need for the rearrangement of substituents, and competing reactions in the solvent.

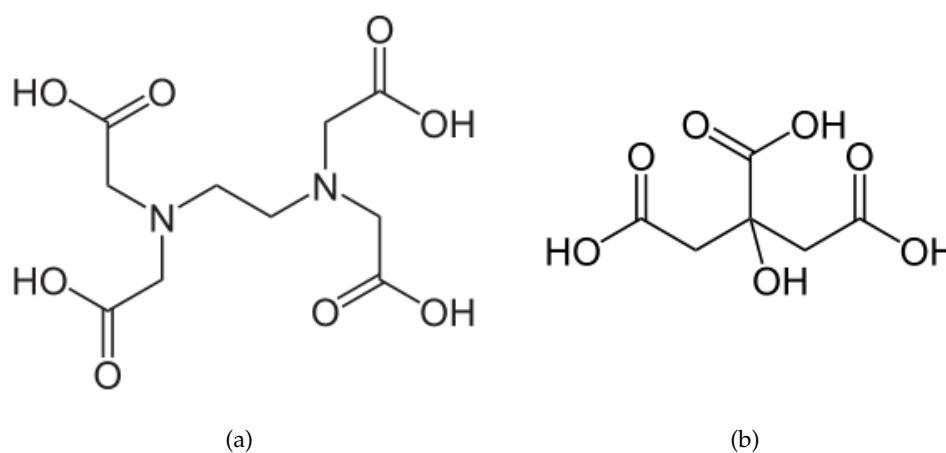


FIGURE 2.10: Chemical structures of commonly used complexing agents (a) EDTA, and (b) citric acid.

Citric acid has three carboxylate groups and is tridentate, while EDTA has a total of six possible points of attachment, four carboxylates and two amines, and is hexadentate. The EDTA chelate is as mentioned very stable, and an illustration of all six donor sites bonded to the same metal cation is shown in Figure 2.11 (a). On the other hand, if the citrate ion were to form a complex using all three carboxylate groups, the chelate would have 7 or 8 membered rings and be relatively unstable. Citric acid is however able to bond with both metal cations and with other citric acid molecules forming 3D networks. Figure 2.11 (b) shows a complex of Sr and citric acid.

To understand the stability of a complex as a whole, regarding the reaction with a Lewis acid/base perspective is helpful. Lewis bases get classified as either soft or hard, where small non polarisable donor atoms are classified as hard, while larger, polarisable atoms are classified as soft. The Lewis acids get classified according to which type of base they have affinities for. A metal ion that prefers a hard base is classified as a hard acid, while an ion that has high affinity for the soft bases is categorised as a soft acid. The stability of the complexes depends on whether the Lewis acid-base

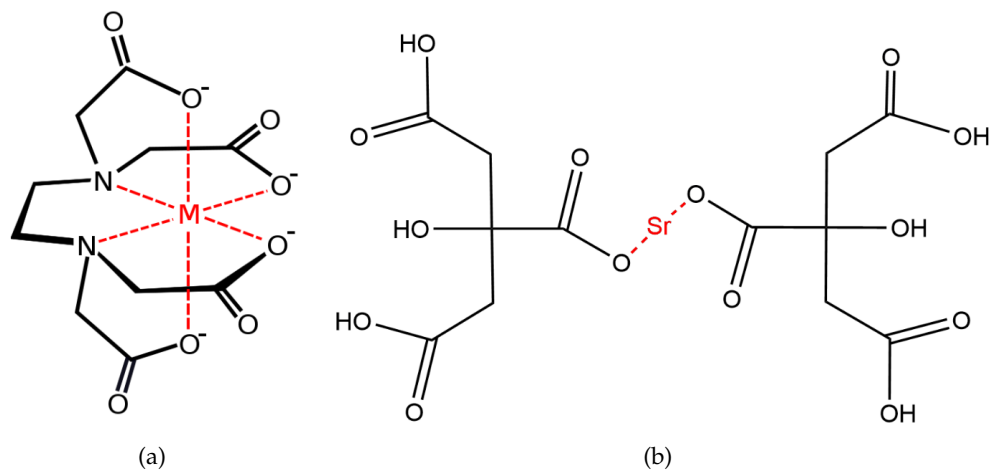


FIGURE 2.11: Illustration of complexes formed with metal cations. (a) EDTA and a 6-fold coordinated metal cation forming a chelate. (b) Citric acid and strontium.

interaction is between hard or soft pairs. This corresponds to the groups suggested by Schwarzenbach, where hard acids form ionic bonds and belong in group A, while soft acids form covalent bonds, group B.

The lithophile elements, La, Ca, and Sr are considered to be hard acids in their ionic state. The transition metal Co on the other hand, is considered to be borderline. Water is counted among the hard Lewis bases due to its strong polarity. The carboxyl- and amine-groups are hard bases, which means that both EDTA and citric acid belong to this group as well.

The stability constant of the complexes formed between the metal cations and EDTA or citric acid, are relatively large due to the hard Lewis acids preference for hard bases. The chelate effect gives EDTA-complexes additional stability.^[60] The total effect of complexation thus increases the cation's solubility, and preserves the homogeneity of the precursor solution as the water evaporates and the ceramic oxide powder is formed during spray pyrolysis.

Powder dispersions

Multiple methods for the preparation of ceramic materials is based on the deposition of a slurry onto a substrate. To achieve the desired properties of the ceramic, it is essential that the suspension of solids remains stable for extended periods of time. A stable slurry will ensure an even distribution of particles, and better control of the microstructure of the final material.

The flow properties and stability of a suspension of solid particles in a liquid is

highly dependent on the viscosity of the dispersion. The viscosity is in turn decided by the volume fraction of solids, their shape, size, surface charge, and degree of agglomeration. In other words; how the particles approach each other, and the degree of attraction or repulsion they experience.^[61] Parameters that affect the properties of the particles themselves is naturally the material's chemical and electronic structure, as well as the presence of any impurities. Additionally the pH of the suspension fluid plays an essential role, due to the interaction between charged particles.

For particles with a significant density difference from the fluid they are dispersed in, gravitational forces will dominate and cause sedimentation. The presence of Brownian motion; the random motion of solid particles in a suspension, caused by collisions with atoms or molecules in the fluid, counter-acts the gravitational forces experienced by the particles. The suspension can thus overcome the gravitational force and remain stable if it satisfies the following criterion;

$$\frac{R^4 \Delta \rho g}{k_b T} < 1 \quad (9)$$

where R is the particle radius, $\Delta \rho$ is the density difference between the fluid and solid, g is the gravitational constant, k_b the Boltzmann constant, and T the absolute temperature.

To maintain stability through Brownian motion, it is essential to prevent agglomeration of the dispersed particles through inter-particle repulsion. The importance of limiting the agglomerate size is evident by Equation 9 which indicates that the influence of gravitational forces scale with increasing particle radius.

There are two main available routes to limit the agglomeration of ceramic particles in a suspension; 1. electrostatic repulsion and 2. steric stabilisation. Determining which of these methods should be used depends entirely on the properties of the suspension in question.

Electrostatic repulsion means that particles are kept apart due to the repulsive forces between similar surface charges, illustrated in Figure 2.12. The degree of dispersion increases with increasing surface charge, which in turn depends on the pH of the liquid the particles are suspended in. The effective repulsion can be adjusted by the addition of charged species that can adsorb on the surface of the particles, creating a charged zone around them. This apparent surface charge is referred to as the zeta potential. The largest absolute value of the zeta potential can be calculated to determine which pH range will achieve maximum dispersion.^[62]

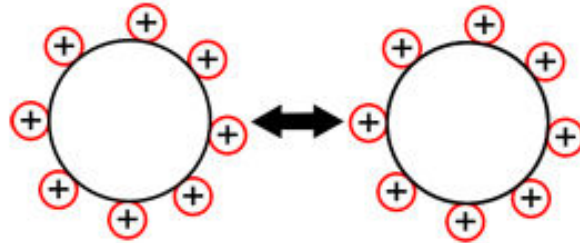


FIGURE 2.12: Illustration of electrostatic stabilisation of particles in a suspension. The positive charges adsorbed on the particle surface causes mutual repulsion. Illustration courtesy of Ayouril.^[63]

The second available route is the use of steric stabilisation. This involves adding a dispersant consisting of polymer chains that adsorb on the ceramic particles and create a physical buffer zone. These organic molecule chains have one end that attaches to the ceramic and has a low solubility in the solvent, and one end that is soluble. The buffer zone allows the ceramic particles to come into closer contact with each other without agglomerating, as illustrated in Figure 2.13. The effectiveness of this steric hinderance depends entirely on the polymer's affinity for the specific ceramic and the suspension fluid. With the help of steric stabilisation, it is possible to keep a suspension well dispersed even when the concentration of solids is high. Steric stabilisation also makes it possible to stabilise suspensions where the zeta potential is reduced close to zero.^[62]

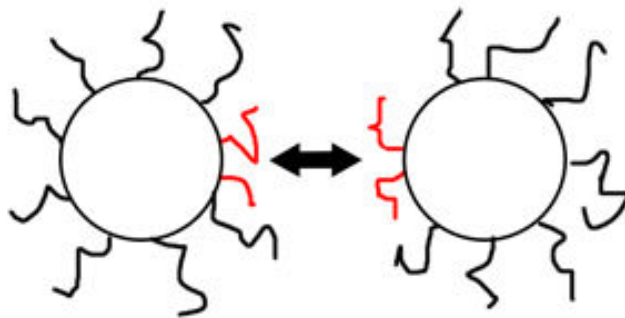


FIGURE 2.13: Illustration of steric stabilisation of particles in a suspension. The polymer chains adsorb on the particle surface and prevent the particles from agglomerating due to steric hinderance. Illustration courtesy of Ayouril.^[63]

Chapter 3

Experimental

3.1 Preliminary investigations

In the preliminary phase of the project, several samples of the nominal composition $(\text{La}_{0.6}\text{Sr}_{0.4})_{0.99}\text{CoO}_3$ (LSC) were prepared by CerPoTech AS, Trondheim. These samples were investigated using X-ray diffraction and thermal analysis to evaluate their phase purity and to identify any secondary phases. Table 3.1 is an overview of the sample compositions used in the preliminary investigations. Abbreviations used to identify samples follow the pattern;

$$CAx - Y$$

where CA means that citric acid was used as a complexing agent, $x = [0.1, 0.5, 1]$ and indicates the molar ratio of citric acid to LSC, and $Y = \text{LC}$ or HC , where LC and HC indicates low and high concentration precursor solutions, respectively.

TABLE 3.1: Overview of the samples in the preliminary investigations. The concentration of the precursor solution used to prepare each sample and the ratio of mole citric acid (CA) to mole $(\text{La}_{0.6}\text{Sr}_{0.4})_{0.99}\text{CoO}_3$ (LSC), are included.

Sample abbreviation	Concentration [g oxide/L]	Molar ratio CA:LSC
CA0.1-LC	~57	0.1:1
CA0.1-HC	~196	0.1:1
CA0.5-LC	~57	0.5:1
CA0.5-HC	~196	0.5:1
CA1-LC	~58	1:1
CA1-HC	~152	1:1

The results of these investigations were used to adjust the concentration of the precursor solution. The adjustments were intended to give a good basis of comparison for parameters relevant for powder production by spray pyrolysis. These parameters include the amount of additive, and the concentration and total volume of the precursor solution.

3.2 Powder preparation

A total of 6 precursor solutions of the nominal composition $(\text{La}_{0.6}\text{Sr}_{0.4})_{0.99}\text{CoO}_3$ (LSC) with varying amounts of citric acid (CA) were prepared. All chemicals used in the synthesis of the $(\text{La}_{0.6}\text{Sr}_{0.4})_{0.99}\text{CoO}_3$ powders are presented in Table 3.2, and an overview of the final powder batches and their abbreviations is given in Table 3.3.

TABLE 3.2: Overview of the chemicals used during synthesis of the $(\text{La}_{0.6}\text{Sr}_{0.4})_{0.99}\text{CoO}_3$ -powder.

Chemical	Supplier	Purity grade
$\text{La}(\text{NO}_3)_3 \cdot 6 \text{H}_2\text{O}$	REEttec	99.995 %
$\text{Sr}(\text{NO}_3)_2$	Alfa Aesar	98 %
$\text{Co}(\text{NO}_3)_2 \cdot 6 \text{H}_2\text{O}$	VWR	GPR RECTAPUR®
Citric acid (anhydrous)	Ensign	≥ 99.5 %

The cation solution of La^{3+} was prepared by the supplier. Two other cation solutions, one for each of the cations Sr^{2+} and Co^{2+} , and a solution of citric acid were prepared by dissolving $\text{Sr}(\text{NO}_3)_2$, $\text{Co}(\text{NO}_3)_2 \cdot 6 \text{H}_2\text{O}$, and citric acid in distilled water. All three solutions were then stirred until clear. The solution containing Co^{2+} , and the industrially made La^{3+} solution were thermogravimetrically standardised at 800 °C, and the cation concentrations calculated to 1.4777 mmol/g and 1.5266 mmol/g, respectively. For the solutions of Sr^{2+} and citric acid, the weight percent was used to estimate concentrations of 1.9 mmol/g and 2.6 mmol/g, respectively.

The four solutions of known concentrations were then used to make six separate precursor solution, following the flowchart in Figure 3.1. The three nitrate solutions were mixed at stoichiometric amounts to form $(\text{La}_{0.6}\text{Sr}_{0.4})_{0.99}\text{CoO}_3$. This LSC-solution was divided into six separate batches. Each batch was added citric acid, and finally diluted by adding distilled water to reach the predetermined volumes and CA:LSC-ratios listed in Table 3.3. All solutions were stirred continuously until spraying, to ensure preservation of the precursor's homogeneity.

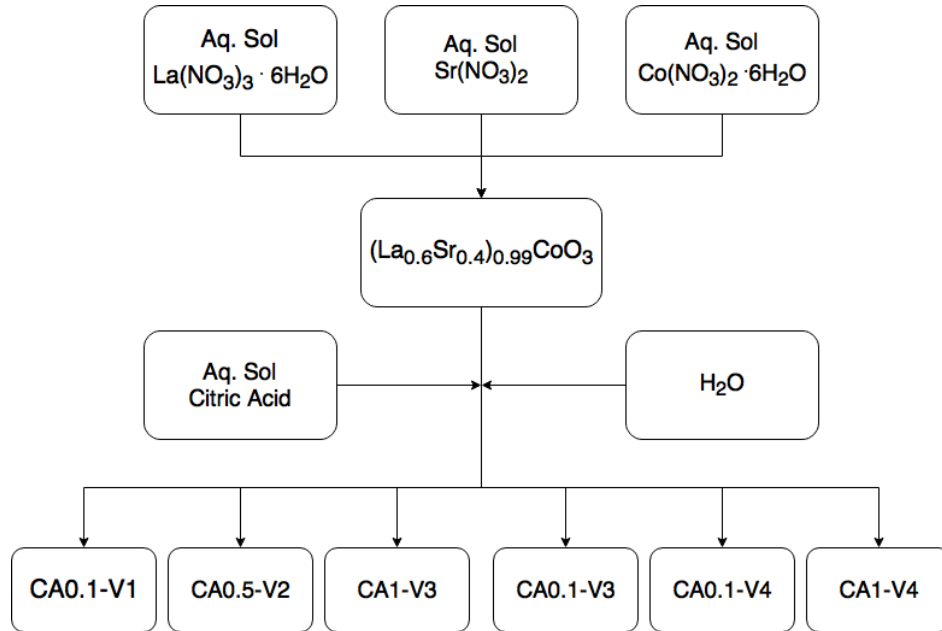


FIGURE 3.1: Flowchart for the synthesis route of the precursor solutions used to make $(\text{La}_{0.6}\text{Sr}_{0.4})_{0.99}\text{CoO}_3$ -powder (LSC). In the sample names, CA means citric acid was used as a complexing agent. 0.1, 0.5, and 1 is the molar ratio of citric acid to LSC. V_z is the volume of the precursor solution, determined by the amount of H_2O added. V_1 is the highest concentration, and V_4 is the lowest concentration.

Spray pyrolysis

All powders were prepared from the aqueous precursor solutions by spray pyrolysis at a set temperature of 1000 °C, an operating pressure of 4 bar and with a solution flow rate of 95 mL/min through a co-current nozzle with 1.5 bar pressurised air. The powder was collected in a cyclone and transferred to containers before the next batch was started. The collected powder that received no further treatment will be referred to as "as-prepared powder".

Heat treatment

Samples (2 g) from the high concentration batch CA1- V_3 and the low concentration batch CA0.1- V_4 , were calcined at varying temperatures between 700 and 1200 °C for 6 hours to investigate the development of phases. A temperature of 750 °C was determined to be sufficient to ensure a phase pure powder, and a sample (4 g) from each batch was then calcined at this temperature with a heating rate of 3.33 °C/min and a hold time of 6 hours. These samples will be referred to as "calcined powder".

Milling







The samples calcined at 750 °C were ball milled for 48 hours using YSZ grinding media. The powders were first dry-milled for 1 hour, following a procedure determined by Cerpotech AS. Isopropanol was then added to the flask, and the samples were milled for an additional 47 hours. The grinding media was removed, and the isopropanol evaporated from the slurry using a hot plate and a magnetic stirrer. The dried slurry was crushed in a mortar using a pestle, and subsequently sieved with a final mesh size of 180. Additionally, after 6, 12, 24, and 48 hours of milling, small samples of slurry (3 mL) were removed from the bottles to investigate the evolution of the powder's particle size distribution. Both the samples taken from the slurry, and the sieved powder will be referred to as "milled powder".

3.3 Samples

All prepared samples were of the nominal composition $(\text{La}_{0.6}\text{Sr}_{0.4})_{0.99}\text{CoO}_3$ (LSC). They were synthesised using varying amounts of citric acid in precursor solutions with different concentrations. The various samples are listed in Table 3.3 with information about the concentration of each precursor solution, the molar ratio of citric acid to LSC, and the abbreviations and colours used to distinguish them throughout this text.

The samples were named following the same pattern as in Section 3.1. But for the new samples, $Y = V_z$ denotes the volume of the precursor solution, determined by the amount of H_2O added. V_1 is the highest concentration, and V_4 is the lowest concentration.

TABLE 3.3: Overview of the different samples investigated in this work and their respective abbreviations throughout this text. The concentration of the precursor solutions, the ratio of mole citric acid (CA) to mole $(\text{La}_{0.6}\text{Sr}_{0.4})_{0.99}\text{CoO}_3$, and the volumes of the precursor solutions are included.

Sample abbreviation	Precursor concentration [g oxide/L]	Molar ratio CA:LSC	Volume [L]
 CA0.1- V_1	222	0.1:1	1.7
 CA0.5- V_2	222	0.5:1	1.8
 CA0.1- V_3	189	0.1:1	2.1
 CA1- V_3	189	1:1	2.1
 CA0.1- V_4	67	0.1:1	6.0
 CA1- V_4	67	1:1	6.0

3.4 Powder characterisation

The as-prepared, calcined, and milled powders were characterised using nitrogen gas adsorption, X-ray diffraction and scanning electron microscopy. Additionally the as-prepared powder was investigated by thermogravimetric analysis, while the particle size distribution was determined for samples of the milled powder using laser diffraction spectrometry. The aim was to investigate how the morphology, surface area, particle size and particle size distribution were affected by variations in precursor concentration and amount of citric acid added to the precursor solutions.

Thermogravimetric analysis

Thermal analysis was performed on samples (~6 mg) of the as-prepared powder using a NETZSCH STA449 Jupiter. All data were collected during heating from 30 to 1000 °C at a heating rate of 3.5 °C/min in 30 mL/min synthetic air, with Al₂O₃ as a reference.

Laser diffraction

Laser diffraction spectrometry was used to measure the particle size distribution (PSD) of the milled powder. Small samples (3 mL) of slurry was removed at intervals throughout the milling procedure, and after milling was completed. The samples were diluted by adding isopropanol (10 mL) and investigated using a Horiba Partica LA-960. The instrument setup was determined by evaluating the behaviour of the dispersed sample at various transmittance ranges. For each of the samples, measurements were conducted on two separate parallels, with two subsequent measurements for each parallel.

Gas adsorption

A Micromeritics TriStar 3000 with nitrogen as the adsorption gas was employed to measure specific surface area (SSA) of the as-prepared, calcined, and milled samples. All samples were degassed at 250 °C overnight before the analysis was conducted. The particles in the samples were assumed to be monodisperse, spherical and non-aggregated, and the BET-equivalent particle size was estimated from the following equation,

$$d_{BET} = \frac{6}{\rho SSA} \quad (10)$$

where ρ is the density of the corresponding phase pure composition, and SSA is the measured specific surface area.

X-ray diffraction

X-ray diffraction patterns of both the as-prepared, calcined, and milled powders were obtained with the use of a Bruker D8 Advance DaVinci X-ray diffractometer. A Cu K_α radiation source (wavelength $\lambda = 1.5418 \text{ \AA}$) with a 0.2 mm slit was employed. The data was collected over a 2θ range between 10-75°, using a step size of 0.013° and a step time

of 0.36 s. The average crystallite size was determined from the XRD pattern using the Scherrer equation^[64],

$$d_{XRD} = \frac{K\lambda}{\beta \cos(\Theta)} \quad (11)$$

where d is the mean size of the crystalline domains, K is a dimensionless shape factor which has a value of 0.9 when the particles are assumed to be spherical, λ is the wavelength of the x-rays, β is the full-width-at-half-maximum value, and Θ is the Bragg angle.

Scanning electron microscopy

A Zeiss Supra 55 VP low vacuum field emission scanning electron microscope was used to investigate the particle morphology and size of both the as-prepared and the milled powder. The as-prepared samples were mounted directly on conductive tape in their dry state. The milled powder was already dispersed in isopropanol from the milling procedure, and one droplet was applied to the holder. The samples were subsequently dried until all isopropanol had evaporated. All powder samples were then coated with gold using an Edwards Sputter Coater S150B at 20mA for 45 seconds. For the SEM micrographs the secondary electron detector and the inlens detector were employed. Both were used at a working distance of 5mm, with an accelerating voltage of 5 kV, and an aperture of 30 μm .

3.5 Preparation of symmetric cells

Spray pyrolysed powder of the nominal composition $\text{Ce}_{0.8}\text{Gd}_{0.2}\text{O}_2$ (CGO) was supplied by CerPoTech AS, Trondheim. The powder had been calcined at 600 °C and milled for 48 hours.

Sintering properties

The sintering properties of the LSC- and CGO-powder were investigated by dilatometry. Pellets with a diameter of 5 mm were fabricated by uniaxial pressing with an applied pressure of 60 MPa for 3 minutes. The pellets were measured using a digital calliper, and the length found to be 3.40 mm and 4.97 mm for the LSC- and CGO-pellet, respectively. The volume change of each pellet during sintering was then measured in air using a Netzsch 402C dilatometer. The investigated temperature ranged from 30 to 1300 °C for LSC, and to 1400 °C for CGO, with an employed heating rate of 3.33 °C/min for both pellets.

Electrolyte

Dense electrolyte pellets of two sizes were fabricated by uniaxial pressing with an applied pressure of 70 MPa for 3 minutes, following the procedure developed by Kjeldby.^[65]

The dimensions of the pellets and the approximate amount of powder used, are listed in Table 3.4. The pellets were placed on a small amount of powder and sintered at 1300 °C for 2 hours, with a heating/cooling rate of 10 °C/min.

TABLE 3.4: Dimensions for the two sizes of CGO pellets fabricated for use as an electrolyte.

Diameter [mm]	Height [mm]	Weight Powder [g]
10	~ 3.2	~ 0.9
20	~ 1.8	~ 2.0

Each pellet's dimensions were measured with a digital calliper before and after sintering. Archimedes' method was used to determine the density of the pellets after sintering. The procedure was performed with isopropanol as the immersion liquid, following ISO 5017:2013. The 10 mm pellets were made to investigate the interface between the cathode and the electrolyte. To ease the process of cleaving the pellet, a cut was made across the diameter, halfway through the pellet. This was meant to give a cleaner cross section to more accurately examine the adhesion and interface between the electrolyte and cathode after application.

All pellets were polished on a Struers LaboPol-21 using SiC-paper with increasingly fine grit size; P500, P800, P1200, and finally P4000, until a reflective surface could be observed. The 20 mm pellets were ground to a thickness of ~0.8 mm and polished on both sides, while the 10 mm pellets were polished only on the side without a cut. Finally all pellets were cleaned with ethanol.

Stability of LSC-dispersion

A larger batch (40 g) of the CA0.1-V₄ sample was calcined and milled, following the procedure described in Section 3.2. As determined by Kjeldby^[65], the stability of a dispersion is essential to be able to deposit an even cathode layer onto an electrolyte. Before attempting the deposition of the cathode, the milled powder was used to investigate the stability of a dispersion of LSC in ethanol with Dolacol D 1003 as a dispersant.

Varying amounts of Dolacol (listed in Table 3.5) was added to ethanol (2 mL) and the solution was mixed thoroughly. Subsequently, powder (0.5 g) was added to each parallel, and the dispersion diluted with ethanol to a total volume of 12 mL. The dispersion was shaken vigorously and placed in an ultrasonic bath for 20 minutes. The dispersion was then transferred to a 10 mL measuring cylinder, avoiding transfer of the final 2 mL, which contained a sediment layer that did not remain dispersed during the ultrasonic treatment. The measuring cylinders were observed for 3 days to investigate which parallels remained stable.

TABLE 3.5: Overview of the investigated compositions used to test the stability of the LSC powder dispersion.

Parallel	Powder [g]	Dolacol D 1003 [g]
1	0.5	0.2
2	0.5	0.3
3	0.5	0.4
4	0.5	0.5
5	0.5	0.6

Cathode

A larger batch of the most stable dispersion (Parallel 3) was made following the same procedure. A small amount (6 mL) of the dispersion was transferred to an Aztek 4709 airbrush. A 9305C nozzle was employed, and the airbrush was connected to argon gas with a pressure of approximately 0.75 bar.

The cathode was then deposited onto the polished electrolyte pellets in thin layers. The ethanol in the dispersion was allowed to evaporate between application of each layer. A total of 30 layers was deemed appropriate to completely cover the electrolyte with a continuous cathode. The 20 mm pellets were turned and placed on two supporting Al_2O_3 rods, to limit the damage to the already applied cathode. The process was then repeated for the other side of the pellet to create a symmetric cell. The 10 mm pellet only had the cathode applied to the uncut side.

One 20 mm and one 10 mm pellet were fired together at three different temperature programs. The annealing parameters for each of the three programs are listed in Table 3.6. For an annealing time of 0 hours, the samples were heated up to T_{max} and immediately cooled down.

3.6 Characterisation of the symmetric cells

The 10 mm pellets were used to investigate the microstructure of the applied cathodes. The pellets were split in two by placing a scalpel directly above the previously made cut, and giving it a small tap. This caused a clean break with minimal damage to the porous cathode. One half of each pellet was cast in epoxy and left to harden for 12 hours. The epoxy units were then ground to expose the pellet's cross section using the procedure described in Section 3.5. This was followed by two polishing steps on a

TABLE 3.6: Annealing programs for the symmetric cells. The annealing time of 0 hours indicates that the cell was heated to T_{max} and immediately cooled down. T_{max} is the temperature listed in the table.

Sample	Temperature [° C]	Time [hours]	Ramp [° C/min]
700c0h	700	0	3
700c1h	700	1	3
800c0h	800	0	3

Struers Tegramin-20 using DiaPro diamond suspensions with appropriate Struers polishing plates; Dur (3 μm), and Mol (1 μm). The other half of the pellets were mounted directly on carbon tape with the cathode surface up.

Both halves of the pellets were sputter coated with gold at 20 mA for 45 seconds. The epoxy unit was then wrapped in aluminium foil, covering as much of the epoxy as possible, while leaving the sample exposed. The foil was secured by carbon tape to ensure contact between the ceramic and the foil.

The cross section was investigated using a Zeiss Ultra, 55 Limited Edition FESEM, employing the secondary and back scatter electron detectors, with an accelerating voltage of 20 kV. Energy-dispersive X-ray spectroscopy was performed using 20 kV accelerating voltage, an aperture of 120 μm , at 10 mm working distance. Both line scans, and element mapping of the interface between electrolyte and cathode were recorded for each sample.

Finally a Zeiss Supra 55 VP LV-FESEM was used to investigate the surface of the cathode. A 20 kV accelerating voltage, with an aperture of 30 μm and a working distance of 5-10 mm was employed. Both the secondary electron and the inlens detector were employed.

3.7 Electrochemical impedance spectroscopy

Electrochemical characterisation was performed by means of impedance spectroscopy on the prepared 20 mm symmetric cells. Using an airbrush to fabricate the cells had left deposited cathode over the entire exposed surface of the electrolyte. To avoid short-circuiting, the circumference of the cell was manually ground on SiC P1200 paper, to remove all direct connection between the two electrodes. The cell was then placed in the furnace between two sheets of platinum foil, and clamped in place with mechanical springs.

The measurements were conducted in the frequency range 3 MHz to 0.1 Hz with an applied AC signal of 1 V. The samples were measured with oxygen as the atmosphere, in a tubular furnace equipped with a ProboStatTM sample holder from NorECs, as seen

in Figure 3.2. An Alpha-A High Performance Frequency Analyser from Novocontrol was used to measure the impedance.

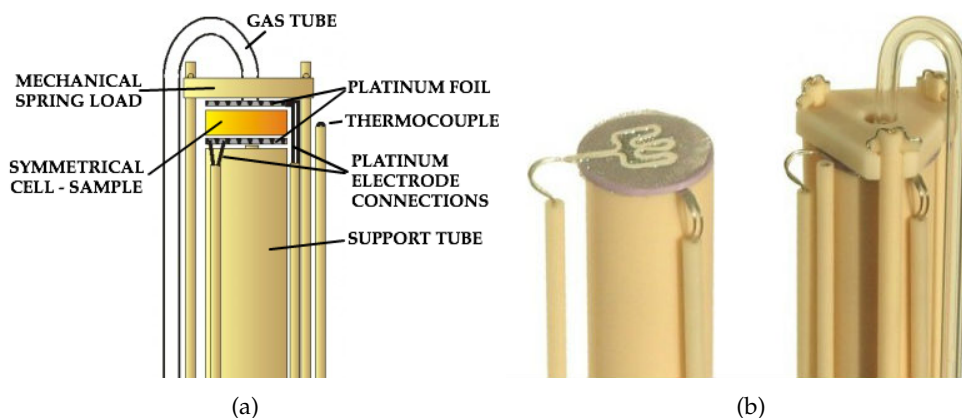


FIGURE 3.2: Schematic of the symmetric cell setup. (a) Cross section of the setup. (b) Image of mounted sample. Illustrations modified from NorECs^[66].

The impedance and conductivity of the cells were measured at 600, 700 and 800 °C with a heating rate of 5 °C/min. One measurement sweep was conducted as soon as the target temperature was reached. The temperature was then allowed to stabilise for an hour before another sweep was recorded. This was repeated for each of the target temperatures. Finally the impedance data was analysed using the software package Z-view® (v3.5a, Scribner Associates Inc.).

The simple circuit shown in Figure 3.3 was used to fit the experimental data from the EIS measurements. $L1$ represents the inductance of the equipment used for the measurements. R_s is the resistance that can be attributed to the electrolyte and includes ohmic losses. $R1$ and $R3$ represent resistances from the chemical processes in the electrodes. Finally, $CPE1$ and $CPE3$ represents the complex capacitance of the model.

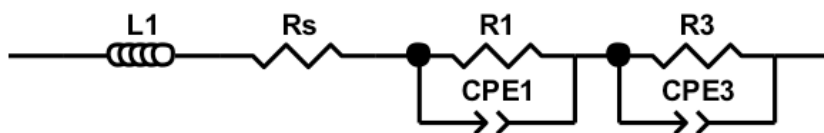


FIGURE 3.3: Schematic of the equivalent circuit used to model the impedance response measured from the symmetric cells.

Chapter 4

Results

4.1 Preliminary analysis

The results reported in this section concern the powder samples prepared by CerPoTech AS, which are described in Section 3.1. The samples were analysed by the author as a part of the preliminary investigations for this project.

Yield

The yield and approximate volume density for the batches investigated in the preliminary analysis is listed in Table 4.1. For samples CA0.1-LC, CA0.1-HC, CA1-LC, and CA1-HC, the yield is plotted against the approximate volume density of the powder in Figure 4.1. The approximate volume densities were calculated using the weight and the estimated volume of the as-prepared powder.

TABLE 4.1: Overview of the estimated volume density and %-yield of the as-prepared powder for each batch.

Sample	Volume density [g/L]	Yield [%]
CA0.1-LC	283	109
CA0.1-HC	354	62
CA0.5-LC	319	22
CA0.5-HC	528	5
CA1-LC	63	81
CA1-HC	165	69

The estimated yield is calculated using the following equation;

$$Yield = \frac{W_{produced}}{W_{theoretical}} \times 100\% \quad (12)$$

where $W_{produced}$ is the actual weight of the produced powder, and $W_{theoretical}$ is the maximum theoretical weight, depending on the composition of the precursor solution. The two samples CA0.5-LC and CA0.5-HC are not included in Figure 4.1 due to the very low yield caused by issues during production.

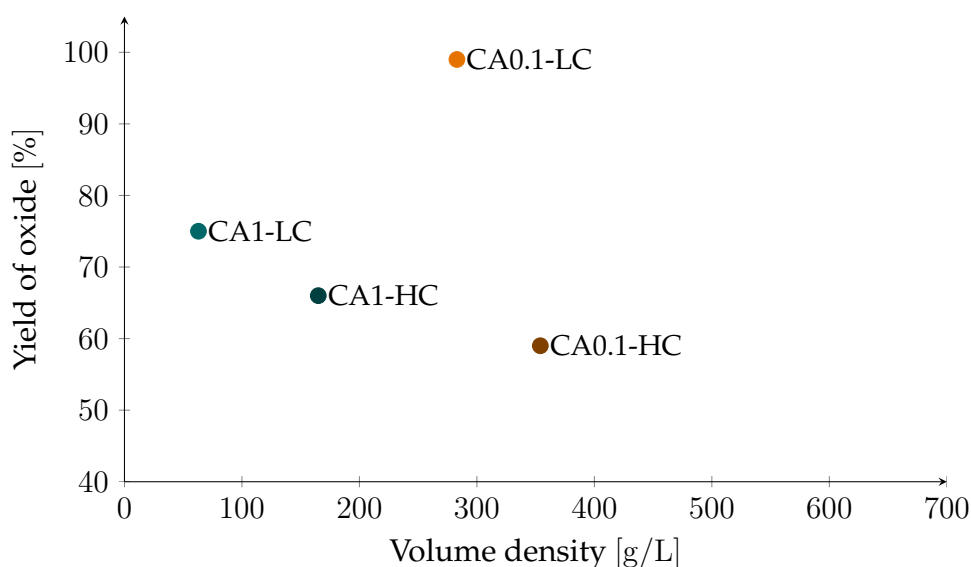


FIGURE 4.1: Total oxide yield for the samples; CA0.1-LC, CA0.1-HC, CA1-LC, and CA1-HC, as a function of the volume density estimated for each sample.

All samples had large variations in volume densities. The powder made with a high amount of citric acid appeared to be fluffier than the powder made by adding less. Additionally, powder from the two low-concentration precursor solutions was more fluffy than that from the high-concentration solutions. The yield was highest for the low concentration batches; CA0.1-LC and CA1-LC. The high yield (109 %) of batch CA0.1-LC could be explained by remaining moisture.

Phase composition

X-ray diffractograms of all samples in the preliminary analysis are displayed in Figures 4.2 and 4.3, for the as-prepared powder, and for powder calcined at 800 °C, respectively.

The rhombohedral perovskite phase of $\text{La}_{0.6}\text{Sr}_{0.4}\text{CoO}_3$ (PDF card 01-089-5719) is a good match for the primary phase of all samples. Four of the recorded diffractograms in Figure 4.2, sample CA0.1-LC, CA0.1-HC, CA0.5-LC and CA1-LC, show the presence of a secondary phase with a primary diffraction line at approximately 37°. This secondary phase has been identified as Co_3O_4 (PDF card 00-001-1152). The diffraction lines for Co_3O_4 become more intense after calcination at 800 °C, as seen in Figure 4.3, due to an increase in crystallinity.

For the four samples containing the secondary phase, a splitting of the peaks at 41°, 59°, and 69° is observed. The split peak at 59° is caused by the presence of cobalt oxide. The characteristic line for this phase is difficult to spot as it is partly hidden behind the line for LSC in Figure 4.3. The remaining split peaks correspond to the data from PDF card 01-089-5719 and are characteristic for the rhombohedral phase of LSC. The broad peaks for CA1-HC are also believed to belong to the rhombohedral phase of LSC, but with less pronounced splitting due to the sample having a composition with a structure closer to cubic symmetry.

The crystallinity of the primary phase looks similar for five of the samples. It increases after calcination, as can be seen by the increased intensity of the diffraction lines in Figure 4.3. The samples containing the most citric acid, have slightly more intense diffraction lines compared to the other samples. The diffractogram for as-prepared powder of sample CA0.5-HC in Figure 4.2 looks very similar to the diffractograms of the calcined powder in Figure 4.3. A likely explanation is that due to clogging of the air-filter during production, this sample had a longer residence time in the furnace, where it experienced grain growth and an increase in crystallinity as a result. This sample was not evaluated further.

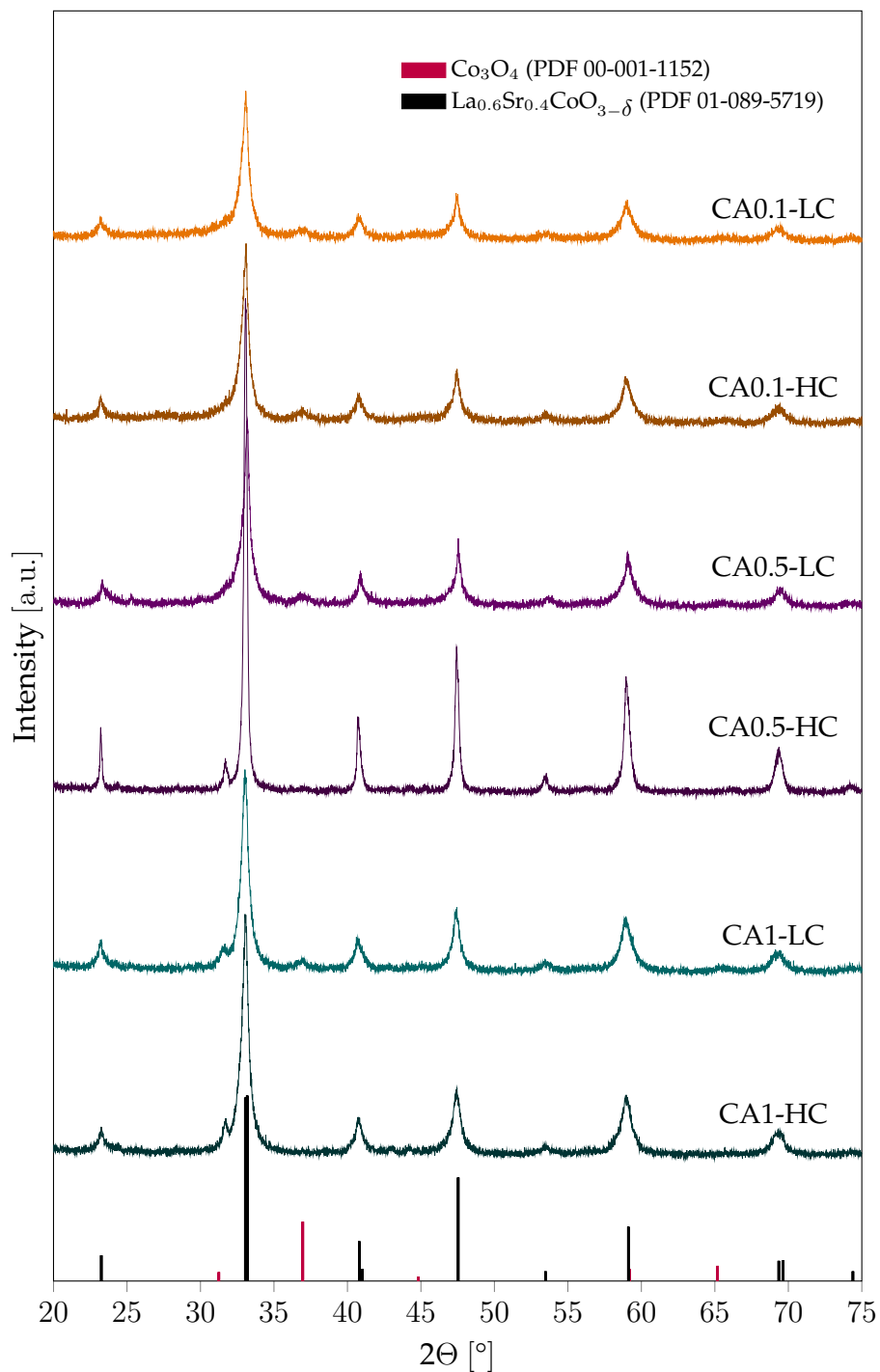


FIGURE 4.2: XRD diffractograms for all as-prepared samples. References are in black; $\text{La}_{0.6}\text{Sr}_{0.4}\text{CoO}_{3-\delta}$ (PDF card 01-089-5719), and red; Co_3O_4 (PDF card 00-001-1152).

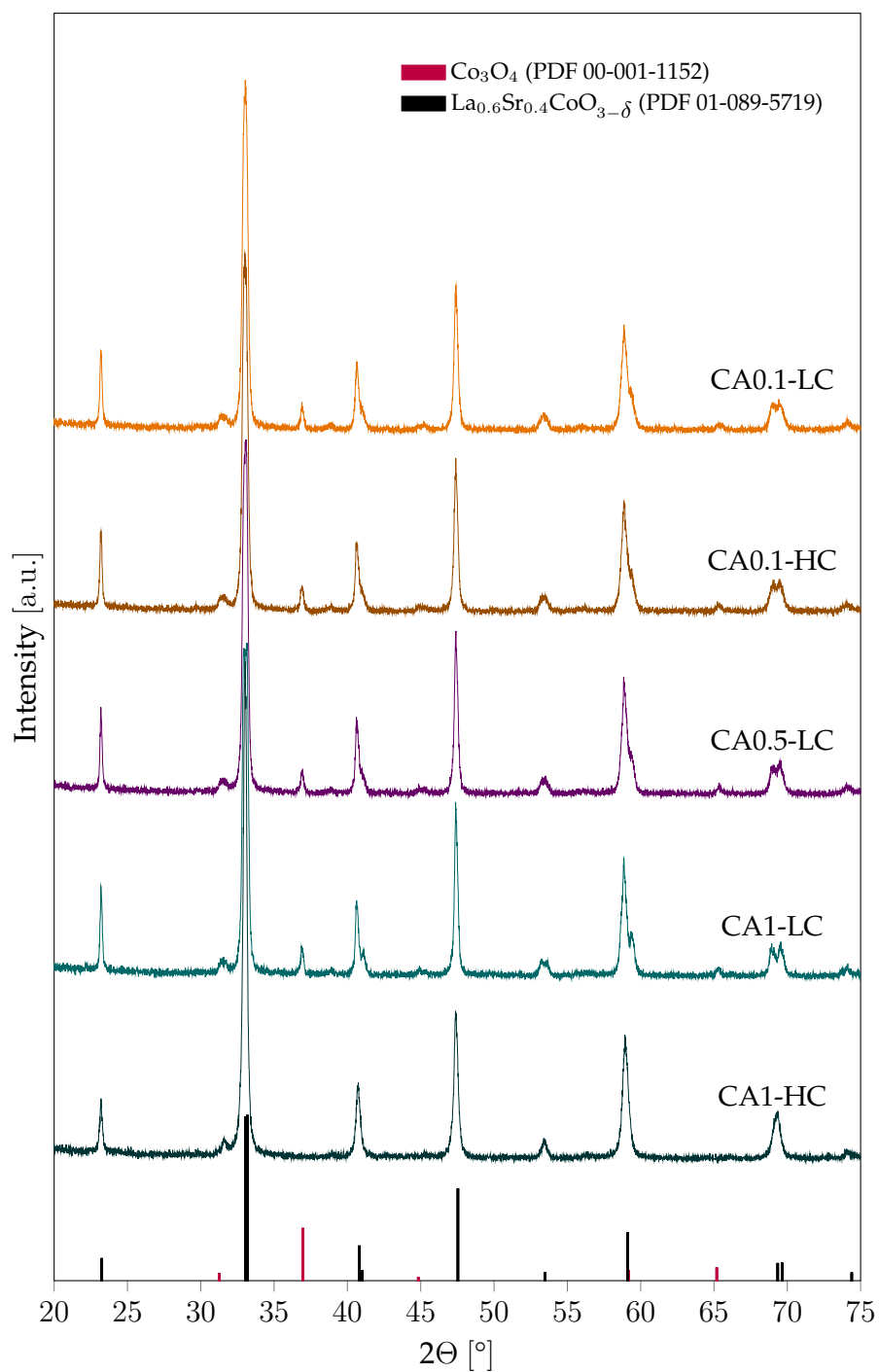


FIGURE 4.3: XRD diffractograms for samples calcined at 800 °C for 6 hours. References are in black; $\text{La}_{0.6}\text{Sr}_{0.4}\text{CoO}_{3-\delta}$ (PDF card 01-089-5719), and red; Co_3O_4 (PDF card 00-001-1152).

Confirmation of the Co_3O_4 secondary phase

Figure 4.4 shows the TG data for three of the samples from the preliminary analysis; CA0.1-HC, CA0.1-LC, and CA0.5-LC. The weight loss happens in several steps, where the first, which occurs below 200 °C, is due to dehydration of the sample, and evaporation of volatile organic compounds. Between 300 and 400 °C, the weight loss is related to the decomposition of remaining organic matter still present in the powder.

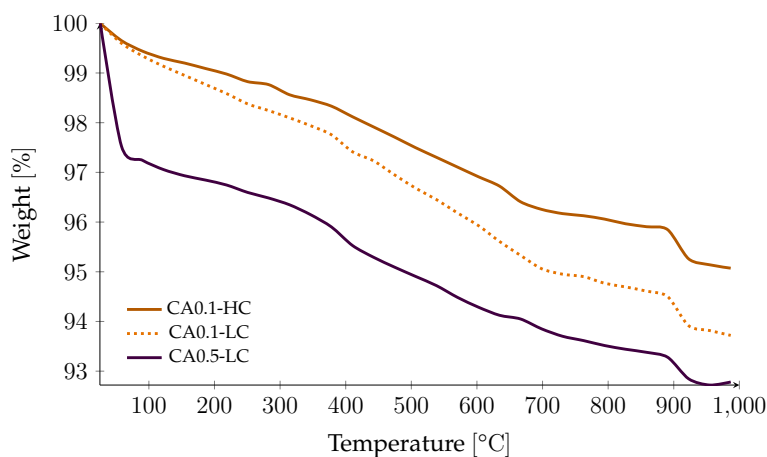
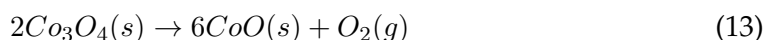


FIGURE 4.4: Thermogravimetric analysis curves for the as-prepared samples CA0.1-HC, CA0.1-LC, and CA0.5-LC, showing the weight loss during heating. The samples were heated up to 1000 °C with a ramp of 3.33 °C/min.

At 900 °C a sudden decline in sample weight (~ 0.6 wt%) represents the phase transition of Co_3O_4 to CoO , with the evolution of oxygen gas as described by the following equation;



Based on the assumption that the entire weight loss is caused by oxygen evolution, the total amount of the secondary Co_3O_4 phase present in the as-prepared samples was found to be approximately 9 wt%.

The recorded weight loss in the first step is somewhat larger for the CA0.5-LC sample. This might be because the sample contained more moisture, or because the increased CA concentration lead to a higher presence of remaining organic compounds. The high yield of sample CA0.1-LC was previously linked to the presence of moisture in the sample. From the data in Figure 4.4, this does not appear to be the case. However, as the powder was stored for an extended period of time, the water has most likely evaporated before the TG data were recorded.

4.2 Powder appearance and yield

The presence of the Co_3O_4 secondary phase in the preliminary batches made them unsuitable for continued evaluation. Because of this, new samples were prepared as described in Section 3.2. The results reported from this section onward all concern the new samples.

All six powder batches were black. The yield for each batch was calculated using Equation 12, and is listed with the approximate volume density for each sample in Table 4.2. The yield is plotted against volume density in Figure 4.5 for five of the samples. The approximate volume density was calculated using the weight and an estimate of the volume of the prepared powder.

TABLE 4.2: Apparent volume density and %-yield of as-prepared powder for each batch.

Sample	Volume density [g/L]	Yield [%]
CA0.1-V ₁	150	65
CA0.5-V ₂	360	10
CA0.1-V ₃	120	72
CA1-V ₃	110	77
CA0.1-V ₄	650	45
CA1-V ₄	70	100

The batches had large variations in volume densities. Powder made with a 1:1 ratio of citric acid:LSC appeared to be fluffier than the powder made using a ratio of 0.1:1. Additionally, the volume density of the powder gradually increased as the concentration of the precursor solution increased. The powder from batch CA1-V₄ had the lowest apparent volume density. This batch also appeared to contain the most moisture, which explains the >100 % yield. In general the yield appears to increase as the concentration of the precursor solution is lowered. A higher amount of citric acid in the precursor solution seems to have the same effect.

CA0.1-V₄ had the highest volume density, but also the lowest yield of the successfully prepared batches. The yield of this sample was low due to issues with the air filter, and the difference in air flow through the furnace is the suspected cause for the large difference in volume density compared to the other samples. Sample CA0.5-V₂ clogged the furnace and the very low yield of 10% left too little powder to complete a full characterisation of the sample. It is therefore not included in the figure.

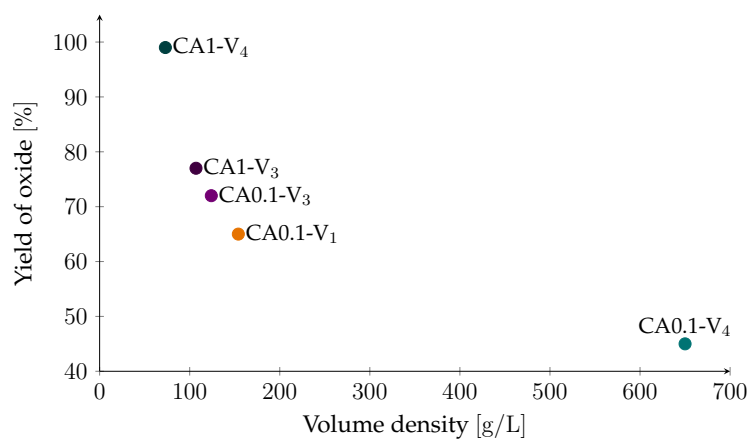


FIGURE 4.5: Total oxide yield for the samples; CA0.1-V₁, CA0.1-V₃, CA0.1-V₄, CA1-V₃, and CA1-V₄, as a function of the volume density estimated for each sample.

4.3 Weight loss of the as-prepared powder

Figure 4.6 shows the TG data of the as-prepared samples, with the exception of sample CA0.5-V₂.

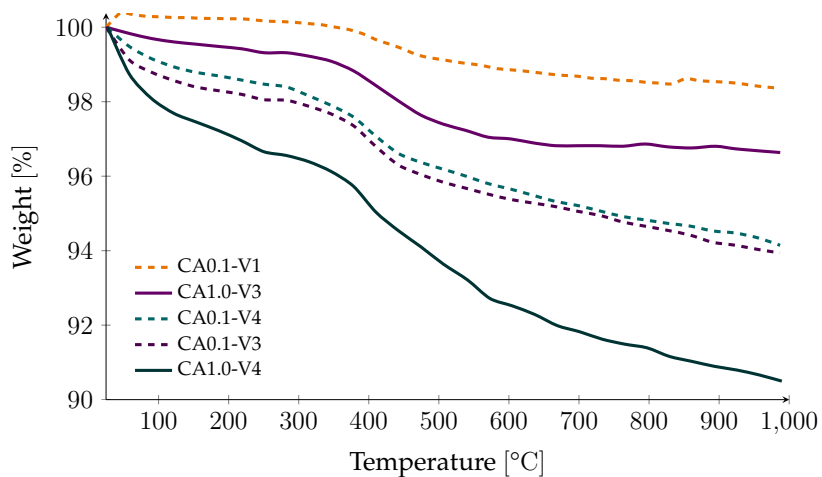


FIGURE 4.6: Thermogravimetric analysis curves for all as-prepared samples, showing the weight loss during heating. The samples were heated up to 1000 °C with a ramp of 3.33 °C/min.

The weight loss occurs in several steps, where the first, below 200 °C, is due to dehydration of the sample and evaporation of volatile organic components. Between 300 and 450 °C, the weight loss is related to the decomposition of remaining organic matter still present in the powder. The sample CA1.0-V3 appears to regain weight at around 600 °C, this is believed to be noise in the recorded data.

4.4 Phase purity

X-ray diffractograms of all samples are shown in Figures 4.7, and 4.8. Figure 4.7 contains data for the as-prepared samples, while Figure 4.8 contains the diffractograms of all samples that were calcined at 750 °C for 6 hours and subsequently milled for 48 hours.

The rhombohedral perovskite phase of $\text{La}_{0.6}\text{Sr}_{0.4}\text{CoO}_3$ (PDF card 01-089-5719) is a good match for the primary phase in all samples. No secondary phases are detected for sample CA0.1-V₁, CA0.1-V₃, CA0.1-V₄, and CA1-V₃. However, a low intensity diffraction line is visible at 25° for the sample CA1-V₄. This phase is believed to be SrCO_3 (PDF card 04-013-9700). The diffraction line for SrCO_3 disappears after calcination, and the phase pure composition is presented with the rest of the calcined samples in Figure 4.8. All samples have increased crystallinity after calcination, which is related to particle growth at high temperature.

The diffractograms recorded for sample CA0.1-V₄ and CA1-V₃ after calcination at various temperatures are presented in Figure 4.9 and 4.10, respectively. The as-prepared powder for both samples has broader, less defined peaks, which become more intense at higher calcination temperatures. The diffractograms after calcination at 1200 °C show a splitting of the peaks for both samples. The evolution of crystallinity is similar for both samples and the slight variations in peak height is suspected to be due to preferential packing during sample preparation.

The diffractogram for sample CA0.5-V₂ in Figure 4.7 shows that the sample contains contaminations, identified as $\text{Sr}(\text{NO}_3)_2$ (PDF card 00-025-0746). The sample experienced some issues during production, and it is possible that the nitrate salts have not fully reacted. The sample was not evaluated further.

The diffractogram recorded for the $\text{Ce}_{0.8}\text{Gd}_{0.2}\text{O}_2$ electrolyte powder that was delivered by CerPoTech AS is presented in Figure 4.11. It is phase pure and matches PDF card 04-011-7336.

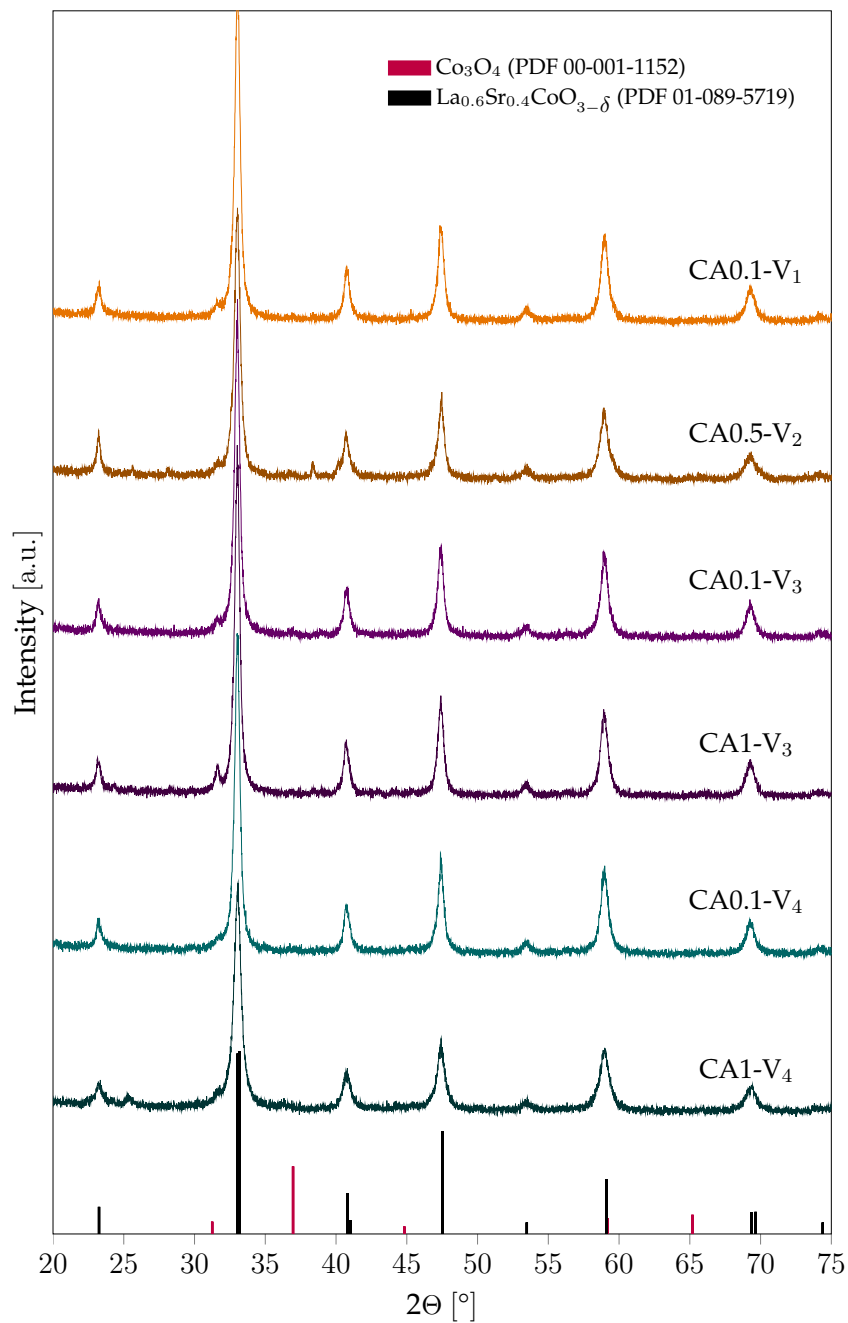


FIGURE 4.7: XRD diffractograms for all as-prepared samples. References are in black; La_{0.6}Sr_{0.4}CoO_{3-δ} (PDF card 01-089-5719), and red; Co₃O₄(PDF card 00-001-1152).

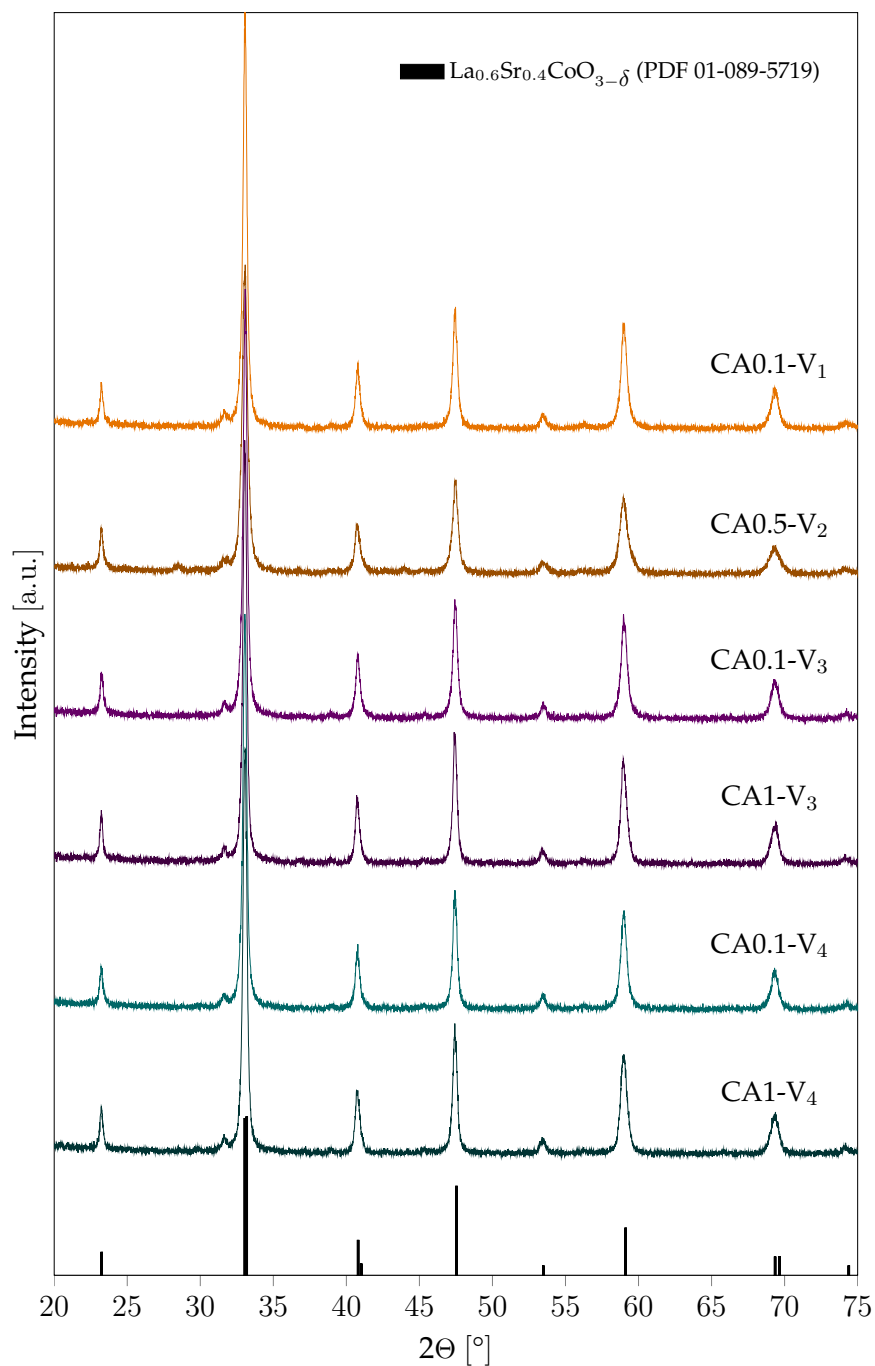


FIGURE 4.8: XRD diffractograms for all samples after calcination at 750 °C for 6 hours. Reference; $\text{La}_{0.6}\text{Sr}_{0.4}\text{CoO}_{3-\delta}$ (PDF card 01-089-5719).

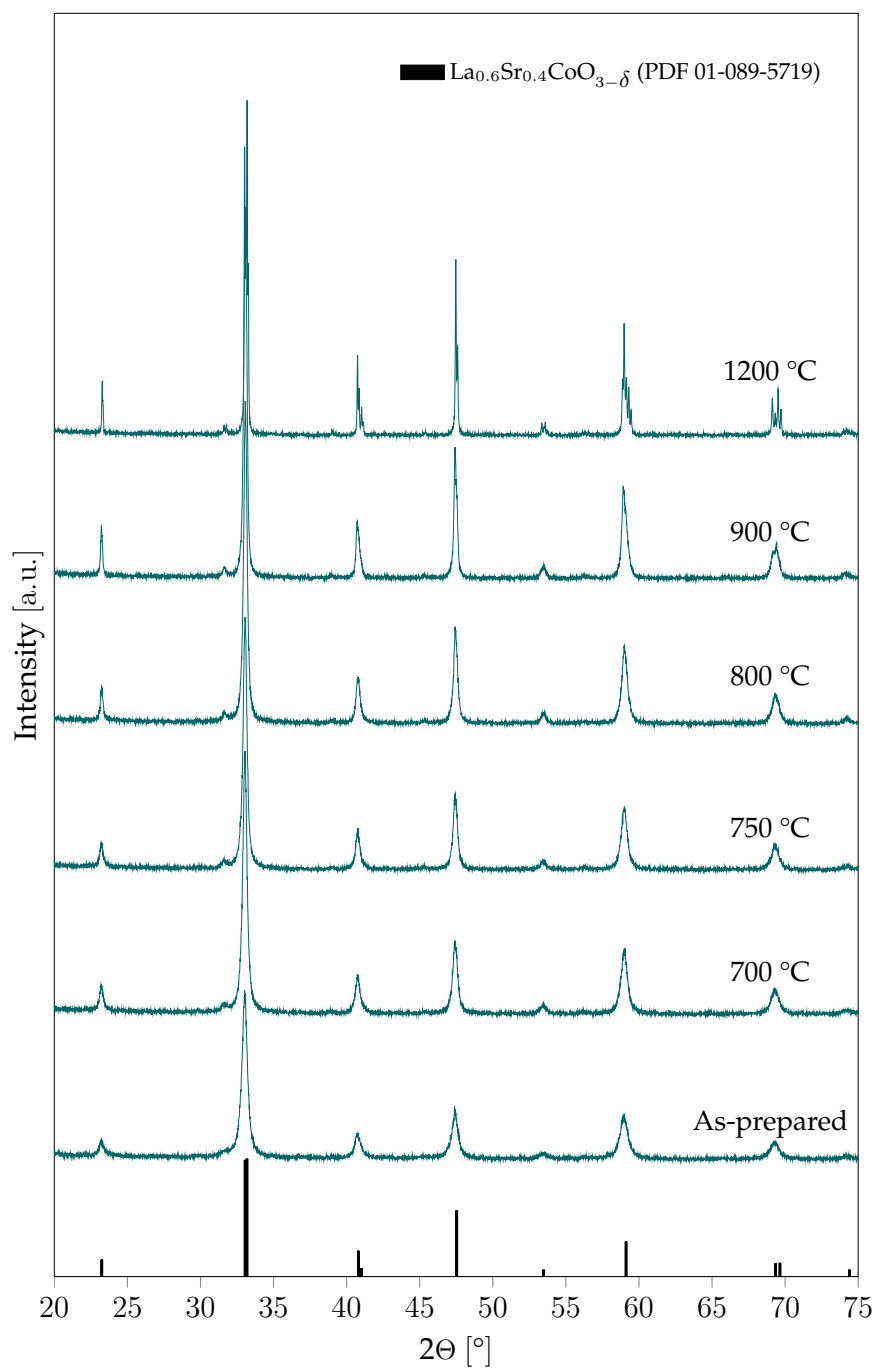


FIGURE 4.9: XRD diffractograms for sample CA0.1-V₄. The diffractograms were recorded for the as-prepared powder and after calcination at 750, 800, 850, 900, and 1200 °C for 6 hours. Reference; $\text{La}_{0.6}\text{Sr}_{0.4}\text{CoO}_{3-\delta}$ (PDF card 01-089-5719).

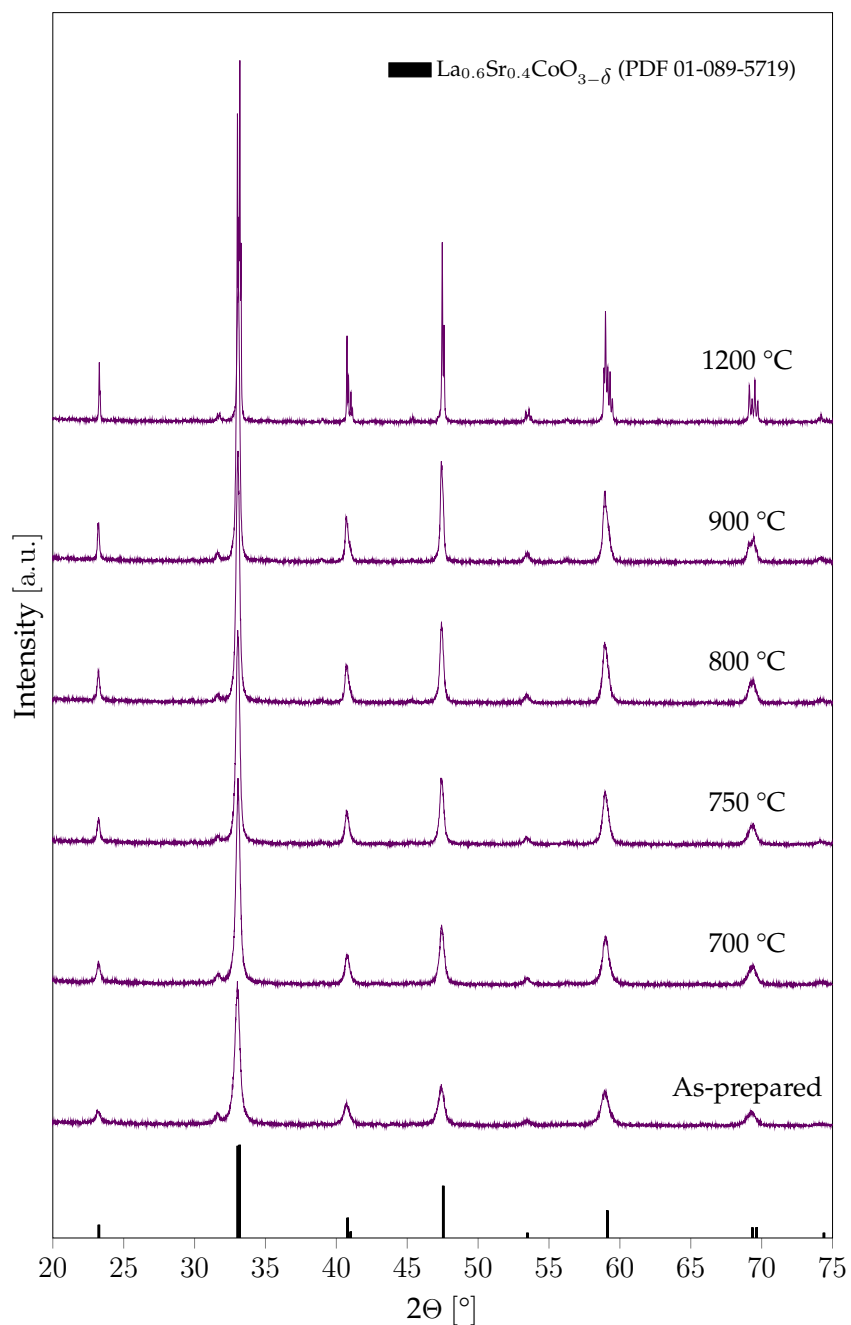


FIGURE 4.10: XRD diffractograms for sample CA1-V₃. The diffractograms were recorded for the as-prepared powder and after calcination at 750, 800, 850, 900, and 1200 °C for 6 hours. Reference; $\text{La}_{0.6}\text{Sr}_{0.4}\text{CoO}_{3-\delta}$ (PDF card 01-089-5719).

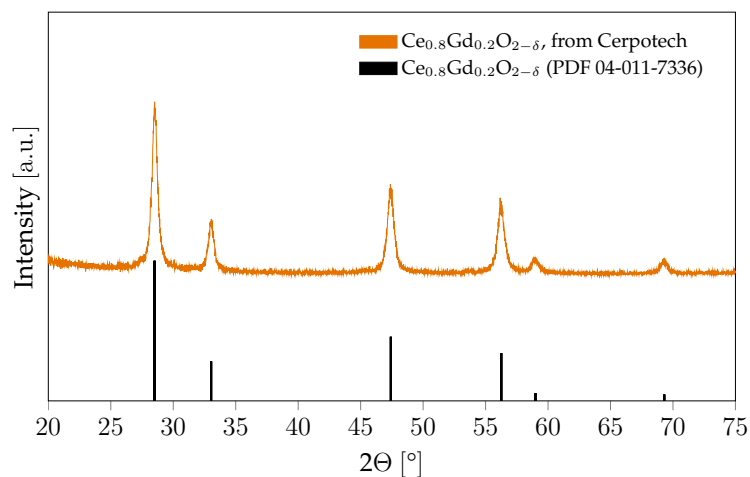


FIGURE 4.11: XRD diffractograms for CGO. Reference; $\text{Ce}_{1-x}\text{Gd}_x\text{O}_{2-\delta}$ (PDF card 04-011-7336).

4.5 Morphology

Scanning electron micrographs of the as-prepared powders are shown in Figure 4.12. The micrographs for the samples calcined at 750 °C and milled for 48 hours are shown in Figure 4.13.

As-prepared samples

The SEM images of the as-prepared powders show hollow eggshells of varying densities and agglomerate sizes. The samples prepared with a 1:1 molar ratio of citric acid to powder have a combination of thin, more broken down shells, and irregular, thicker spheres. These samples appear to have a more uniform size distribution than samples prepared using less citric acid. The three samples with a ratio of citric acid to powder of 0.1:1, indicate that lowering the concentration of the precursor leads to the formation of thinner core shells.

CA0.1-V₁, which is the sample with the smallest volume, and lowest ratio of citric acid to LSC, is pictured in Figure 4.12 (a). The image exhibits an inhomogeneous powder, ranging from small, hollow spheres of about 3 μm, to irregular 3D shapes of approximately 30 μm diameter.

CA0.5-V₂ in Figure 4.12 (b), clearly stands out as most of the powder does not have the characteristic eggshell morphology, but is organised in random fragile networks. The few spheres that are present have an average size of 6 μm.

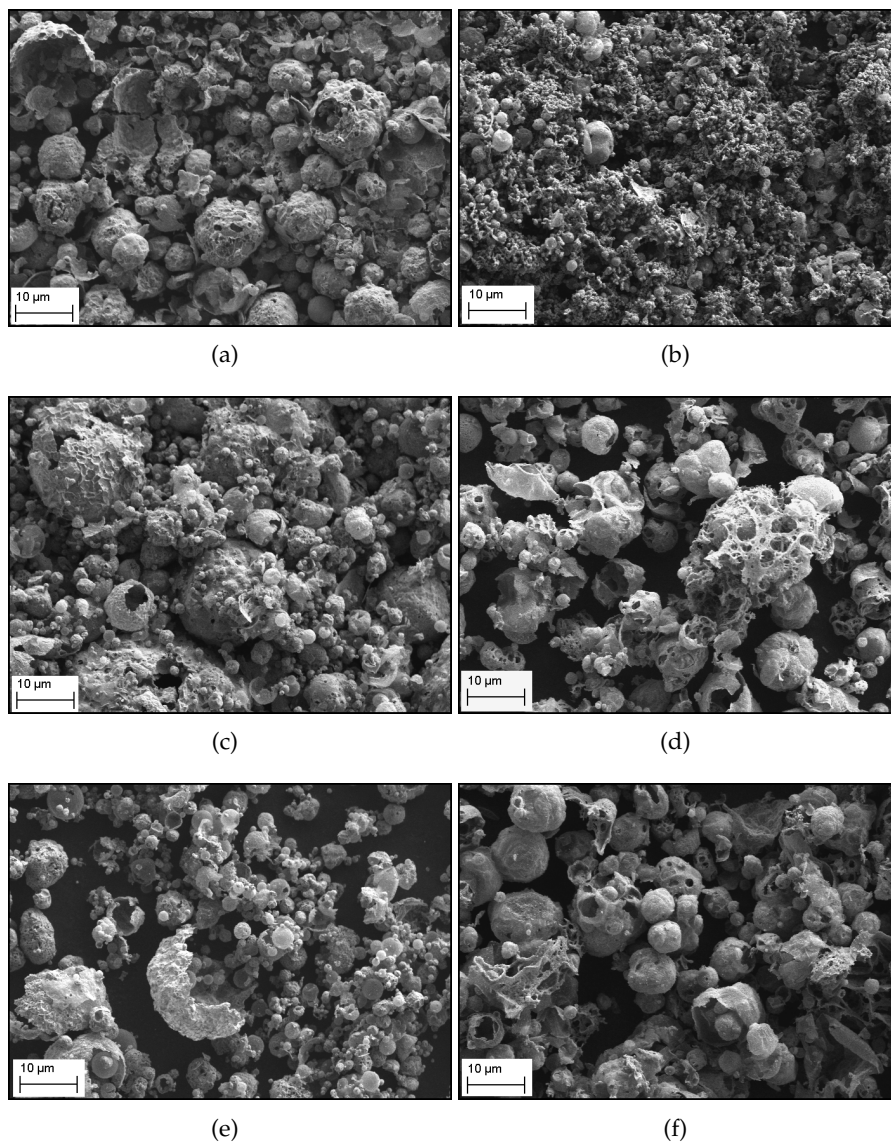


FIGURE 4.12: SEM micrographs of as-prepared samples: a) CA0.1-V₁, b) CA0.5-V₂, c) CA0.1-V₃, d) CA1-V₃, e) CA0.1-V₄, f) CA1-V₄.

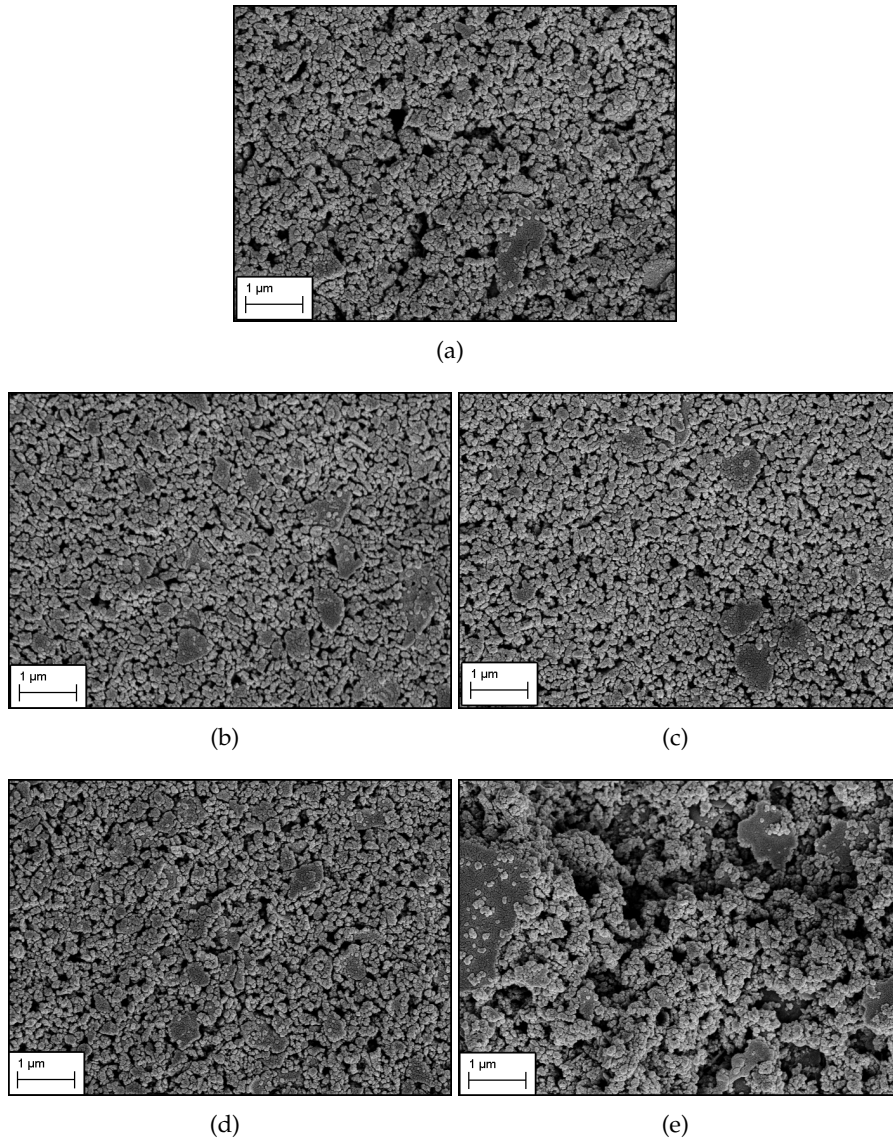


FIGURE 4.13: SEM micrographs of samples calcined for 750 °C for 6 hours and subsequently milled for 48 hours: a) CA0.1-V₁, b) CA0.1-V₃, c) CA1-V₃, d) CA0.1-V₄, e) CA1-V₄.

CA0.1-V₃ in Figure 4.12 (c), also exhibits a very inhomogeneous powder, but the densities of the core shells in this sample are more similar than the densities of those of CA0.1-V₁ in Figure 4.12 (a). The size distribution varies between spheres of 1 μm and 30 μm , and the shapes are less irregular than for CA0.1-V₁.

CA1-V₃ in Figure 4.12 (d), has more even spheres with sizes ranging from 3 μm to 18 μm in diameter. This sample also has a large amount of partly broken down shells, possibly due to the very thin walls most spheres appear to have.

CA0.1-V₄, pictured in Figure 4.12 (e), is the sample with the largest variations in agglomerate size. The sample mostly consists of very small spheres of approximately 1 μm , but contains the occasional large sphere, measuring up to 50 μm .

Finally, the sample CA1-V₄, pictured in Figure 4.12 (e), looks very similar to CA1-V₃ in Figure 4.12 (d). This sample also consists of more evenly sized spheres ranging from 3 μm to 18 μm diameter, with most of the spheres appearing to have very thin shells.

Calcined and milled samples

The SEM images of the samples calcined at 750 $^{\circ}\text{C}$ for 6 hours, and subsequently milled for 48 hours, in Figure 4.13, all show that the characteristic core shells have been mostly broken down. However, all samples contain some large agglomerates assumed to be pieces of core shells not broken down by the the milling procedure. All images exhibit relatively even particles with an average size of approximately 100 nm.

CA0.1-V₃ and CA1-V₃ in Figure 4.13 (b) and (c) respectively, have a higher amount of partly unbroken agglomerate shells than the other samples. It is important to note that the sample CA1-V₄, pictured in Figure 4.13 (e), looks different from the other samples. This is only a result of the sample preparation and does not indicate that the sample is different from the others in any other way.

4.6 Specific surface area

The specific surface area (SSA) measured for the as-prepared, calcined, and milled samples are listed in Table 4.3. Calcination at 750 $^{\circ}\text{C}$ decreases the SSA compared to the as-prepared samples. After milling, all samples have a strongly increased SSA, which is even higher than the SSA measured for the as-prepared powder. CA0.1-V₁, CA1-V₃, and CA1-V₄ are the samples with the highest SSA after milling, all above 18 m^2g^{-1} , with CA1-V₄ as high as 21 m^2g^{-1} . Note the large SSA for the as-prepared sample of CA1-V₄; 41.9 m^2g^{-1} .

TABLE 4.3: Values measured for the specific surface area of the as-prepared, calcined and milled samples, as measured by nitrogen adsorption.

Sample	As-prepared [m ² g ⁻¹]	Calcined 750 °C [m ² g ⁻¹]	Milled 48 hours [m ² g ⁻¹]
CA0.1-V ₁	7.0	5.6	18.1
CA0.5-V ₂	8.0	6.2	-
CA0.1-V ₃	10.1	6.3	15.5
CA1-V ₃	14.9	8.2	18.1
CA0.1-V ₄	12.9	7.0	17.7
CA1-V ₄	41.9	11.5	21.2

4.7 Particle size calculations

Crystallite size was calculated for the as-prepared, calcined, and milled samples by measuring the most intense diffraction line (at approximately 33°) from the XRD patterns, and employing Equation 11. The BET equivalent particle size was calculated for the as-prepared, calcined, and milled samples using Equation 10, the SSA values listed in Table 4.3, and the La_{0.6}Sr_{0.4}CoO₃ theoretical density of 6.72 g/cm³ from PDF card 01-089-5719. The particle size estimated from the SEM images was found by counting and measuring 50 particles in a line. The measurement was repeated several times for each sample, finally calculating the average particle size. All calculated values are listed in Table 4.4.

TABLE 4.4: Average particle (d_{SEM} , d_{BET}) and crystallite size (d_{XRD}) calculated for the as-prepared, calcined and milled samples, using the SEM images, and Equations 10 and 11 respectively.

Sample	As-prepared		Calcined 750 °C		Milled 48 hours		
	d_{XRD} [nm]	d_{BET} [nm]	d_{XRD} [nm]	d_{BET} [nm]	d_{XRD} [nm]	d_{BET} [nm]	d_{SEM} [nm]
CA0.1-V ₁	36	128	49	160	45	49	85
CA0.5-V ₂	32	112	38	145	-	-	-
CA0.1-V ₃	38	88	50	141	45	58	113
CA1-V ₃	39	60	51	109	43	49	121
CA0.1-V ₄	36	69	54	127	44	50	95
CA1-V ₄	27	21	49	78	42	42	103

4.8 Particle size distribution

The particle size distributions (PSD) for samples taken from the milling slurries after 48 hours are listed in Table 4.5. The PSD was measured using volume distribution. Four values are reported for each sample to fully describe the distribution.

TABLE 4.5: Particle size distribution of the samples milled for 48 hours. D_{50} is the median particle size, while D_{10} and D_{90} indicate the size which 10% and 90% of the population lies below, respectively. Mode is the peak of the frequency distribution. All values are reported from the volume distribution of the sample.

Sample	D_{10} [μm]	D_{50} [μm]	D_{90} [μm]	Mode [μm]
CA0.1-V ₁	0.61	1.05	2.13	0.94
CA0.1-V ₃	0.54	2.10	5.32	3.63
CA1-V ₃	0.23	0.50	0.98	0.54
CA0.1-V ₄	0.20	0.42	0.84	0.42
CA1-V ₄	0.22	0.49	1.23	0.48

A plot of the particle size distribution for all samples is shown in Figure 4.14. Both the cumulative particle size and the percentage of particles of a given size are included.

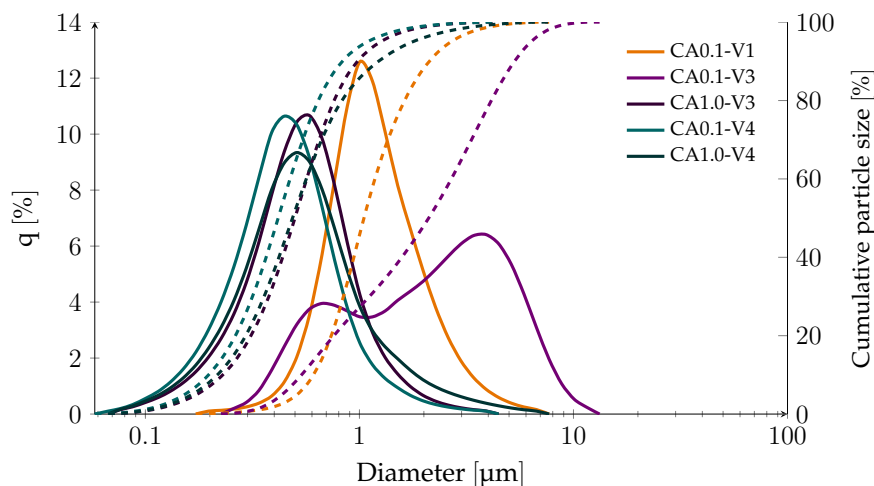


FIGURE 4.14: Particle size distribution for all samples after milling for 48 hours. Solid lines, plotted on the primary y-axis, while dashed lines are plotted on the secondary y-axis.

As the figure shows, most of the samples have particle size distributions of relatively similar sizes, with the exception of CA0.1-V₁ and CA0.1-V₃. CA0.1-V₁ has a slightly narrower distribution than the other samples, but has larger particles. CA0.1-V₃ has a bimodal distribution, and is the only sample to exhibit that type of behaviour.

4.9 Evaluation of milling procedure

Particle size distribution

The particle size distributions that were measured for the samples taken from the CA0.1-V₄, and CA0.1-V₃ milling slurries after 6, 12, 24, and 48 hours are listed in Table 4.6 and Table 4.7, respectively. The PSD was measured using volume distribution.

TABLE 4.6: Particle size distribution of the CA0.1-V₄ sample, milled for 6, 12, 24, and 48 hours. D₅₀ is the median particle size, while D₁₀ and D₉₀ indicate the size which 10% and 90% of the population lies below, respectively. Mode is the peak of the frequency distribution. All values are reported from the volume distribution of the sample.

Sample	Milling time [h]	D ₁₀ [μm]	D ₅₀ [μm]	D ₉₀ [μm]	Mode [μm]
CA0.1-V ₄	6	0.27	0.61	2.05	0.54
CA0.1-V ₄	12	0.28	0.59	1.30	0.62
CA0.1-V ₄	24	0.32	0.64	1.26	0.63
CA0.1-V ₄	48	0.34	0.64	1.14	0.63

TABLE 4.7: Particle size distribution of the CA0.1-V₃ sample, milled for 6, 12, 24, and 48 hours. D₅₀ is the median particle size, while D₁₀ and D₉₀ indicate the size which 10% and 90% of the population lies below, respectively. Mode is the peak of the frequency distribution. All values are reported from the volume distribution of the sample.

Sample	Milling time [h]	D ₁₀ [μm]	D ₅₀ [μm]	D ₉₀ [μm]	Mode [μm]
CA0.1-V ₃	6	0.36	0.76	1.70	0.72
CA0.1-V ₃	12	0.28	0.57	1.10	0.62
CA0.1-V ₃	24	0.38	0.79	1.96	0.72
CA0.1-V ₃	48	0.74	2.22	6.64	2.78

The PSD for the sample CA0.1-V₄ is plotted in Figure 4.15. As shown in the figure there is a continuous evolution of the particle size distribution, which becomes narrower, but with slightly larger median particles as the duration of milling increases.

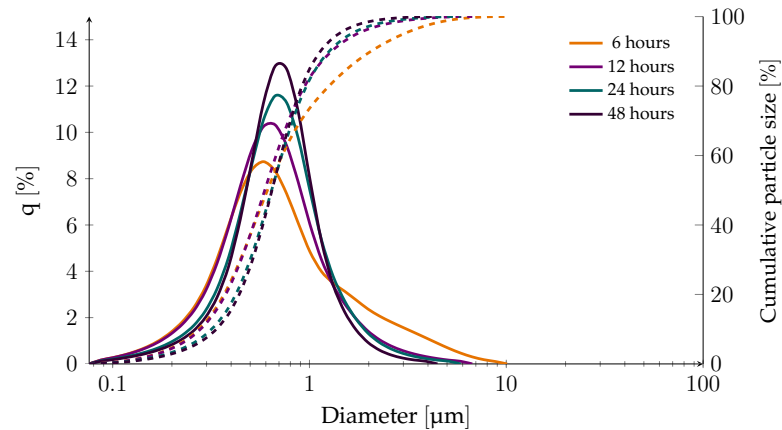


FIGURE 4.15: Plot of the volume particle size distribution measured for sample CA0.1-V₄, after milling for 6, 12, 24, and 48 hours.

The PSD for the sample CA0.1-V₃ is plotted in Figure 4.16. There appears to be no systematic evolution of the particle size distribution for this sample. The flattened shape of the curve for 48 hours corresponds to the bimodal distribution for the same sample in Figure 4.14.

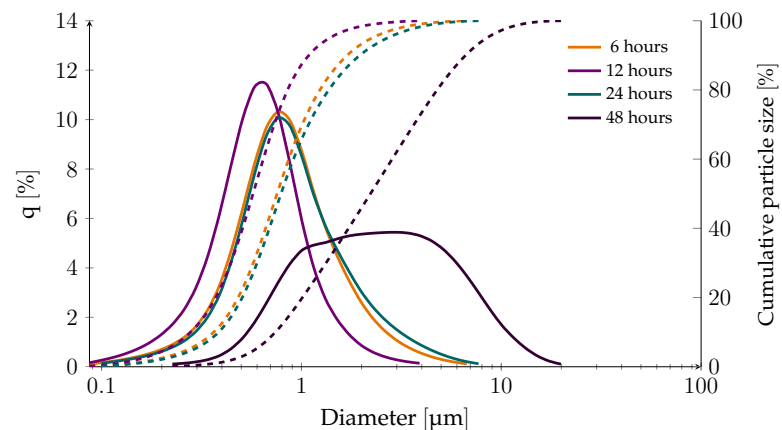


FIGURE 4.16: Plot of the volume particle size distribution measured for sample CA0.1-V₃, after milling for 6, 12, 24, and 48 hours.

Morphology and size

The SEM-images of the samples taken from the milling slurries after 6, 12, 24, and 48 hours, are shown in Figure 4.17 (a) for CA0.1-V₄, and (b) for CA0.1-V₃. The milling time increases from top to bottom in the images.

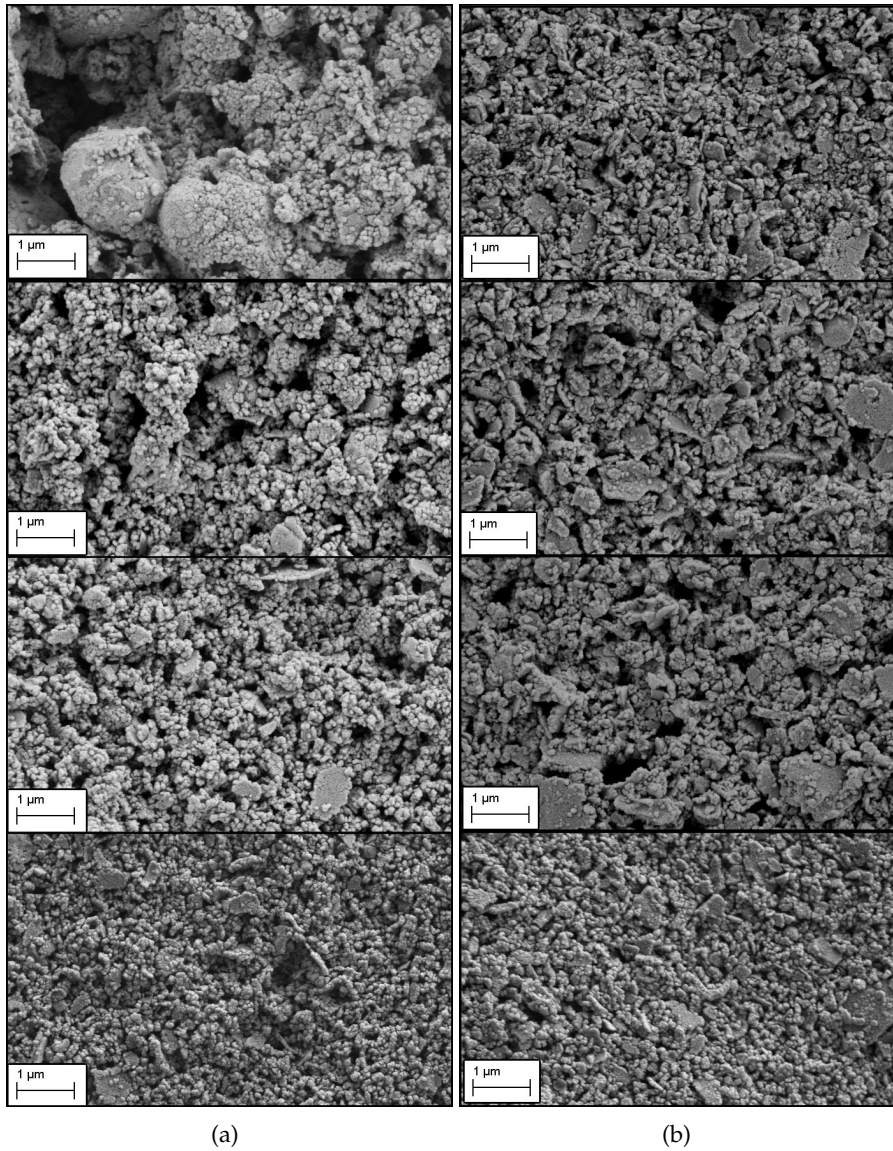


FIGURE 4.17: SEM micrographs of samples a) CA0.1-V₄ and b) CA0.1-V₃ taken from the slurry during milling at 6, 12, 24, and 48 hour intervals. The milling time increases from top to bottom in the figure.

For sample CA0.1-V₄ in (a) there appears to be a gradual evolution of the particle size towards smaller particles, as the duration of milling increases. For the image taken after 6 hours there is still a large presence of unbroken agglomerates. Most of these have been broken down in the image taken after 12 hours, but some large core shell pieces are still visible. After 24 hours these pieces have decreased in size. Finally the particle size distribution is the most even, with on average smaller particles in the image taken after 48 hours.

For sample CA0.1-V₃ in (b) a similar trend does not exist, as the particles appear smaller and more even for the image taken after 6 hours than for those at 12 and 24 hours. The particle sizes in the image taken after 48 hours appears to be somewhat finer than in the previous images. When comparing the images for sample CA0.1-V₄ and CA0.1-V₃ taken after a milling time of 48 hours, the shell structures in the latter seem to be less broken down, and the particle size distribution appears broader as a result.

4.10 Sintering kinetics

The volume change that was measured by dilatometry for $(\text{La}_{0.6}\text{Sr}_{0.4})_{0.99}\text{CoO}_3$ (LSC) and $\text{Ce}_{0.8}\text{Gd}_{0.2}\text{O}_2$ (CGO) is shown as a function of temperature in Figures 4.18 and 4.19, respectively. For LSC, the figure shows that densification initiates at 700 °C and continues until 1175 °C. The maximum sintering rate occurs at approximately 1000 °C.

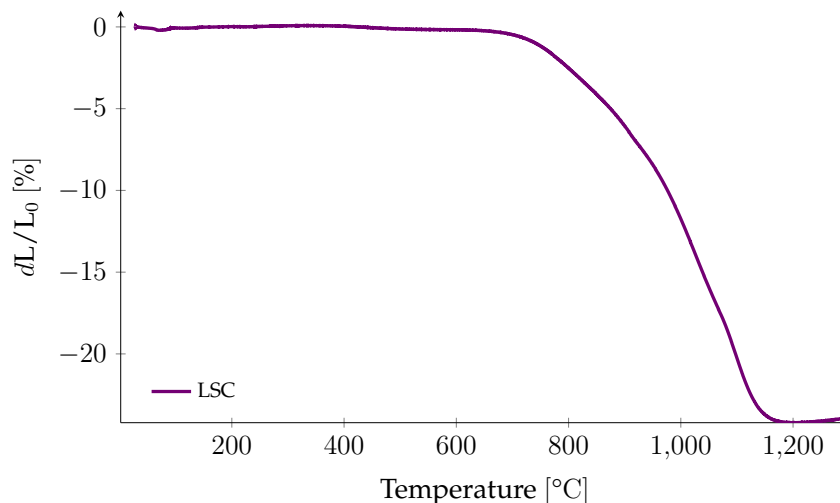


FIGURE 4.18: Volume change as a function of temperature for $(\text{La}_{0.6}\text{Sr}_{0.4})_{0.99}\text{CoO}_3$ heated to 1300 °C.

In Figure 4.19 densification of CGO initiates at 700 °C and continues at a weak rate until approximately 1100 °C. After 1100 °C the rate increases, and densification continues past 1400 °C. The maximum sintering rate occurs between 1300 and 1400 °C.

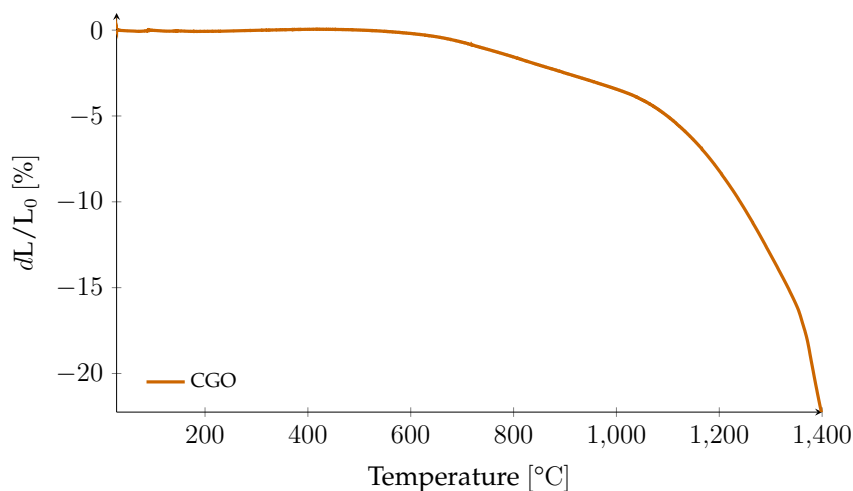


FIGURE 4.19: Volume change as a function of temperature for $\text{Ce}_{0.8}\text{Gd}_{0.2}\text{O}_2$ heated to 1400 °C.

4.11 Characterisation of symmetric cells

Cross section and cathode surface

The SEM micrographs taken of the fabricated symmetric cells are shown in Figure 4.20 and 4.21, where the images are of the surface and cross section of the cathode respectively. The scale bars vary between images.

The images of the cathode surface in Figure 4.20 show a relatively porous cathode. Image (a), (c), and (e) show a part of the cathode surface that has been damaged, exposing the electrolyte underneath. Image (b), (d), and (f) show a representative part of the even surface of the cathode layer.

Subfigure (a) and (b) show the sample fired at 700 °C with no hold time. The cathode is delaminated and appears to have fallen off completely in some sections of the surface, visible along the top edge in image (b). The images in (c) and (d) are from the sample fired at 700 °C for 1 hour. The surface is relatively even and the electrolyte is not visible. Finally the sample fire at 800 °C with no hold time, is pictured in subfigure (e) and (f). This sample also appears to have an even layer of porous cathode with little damage and good adhesion.

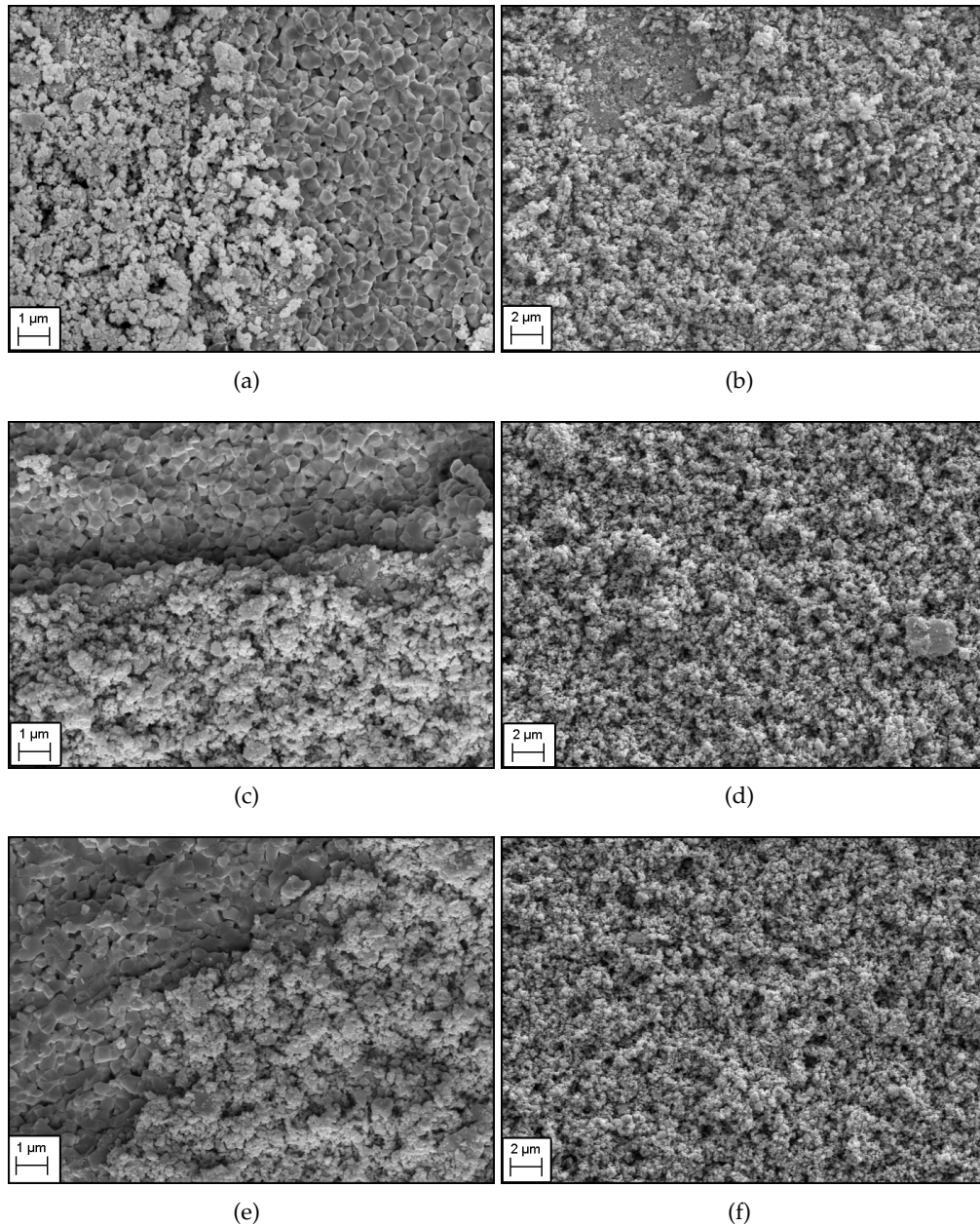
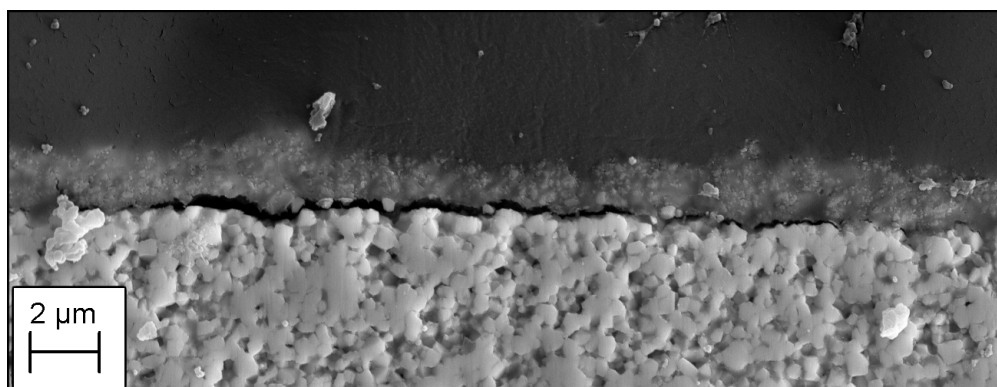
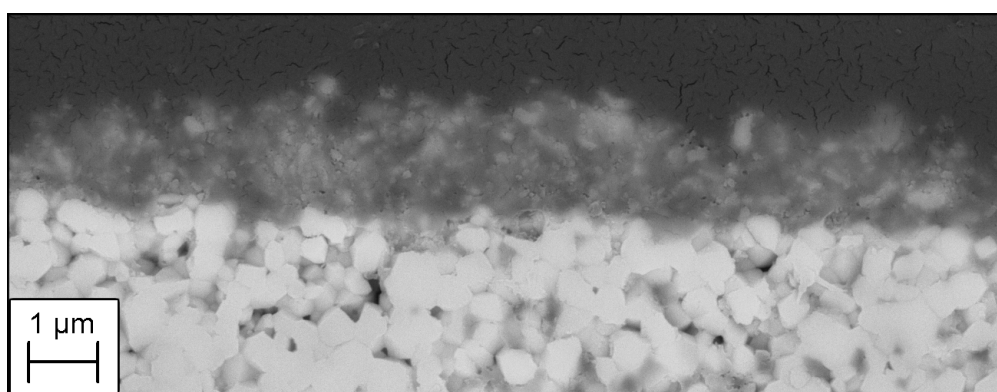


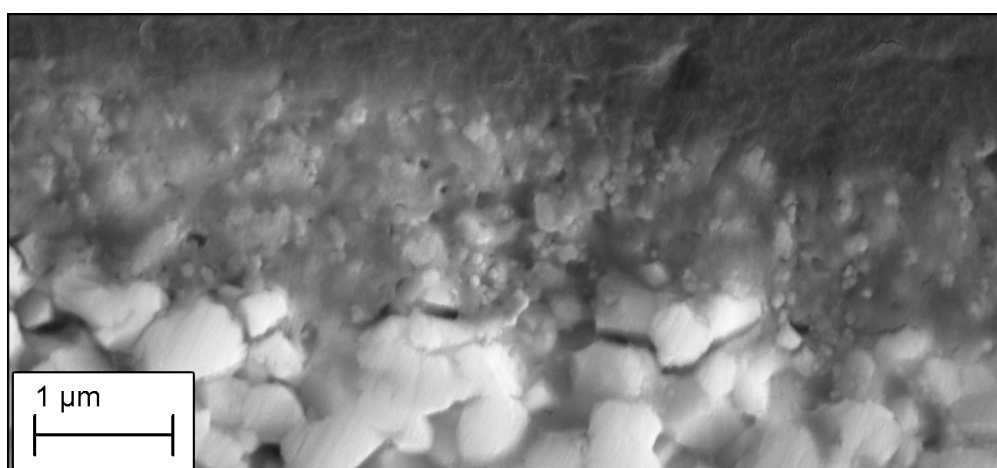
FIGURE 4.20: SEM micrographs of the cathode surface: a) and b) 700 °C, no hold time. c) and d) 700 °C, 1 hour hold time. e) and f) 800 °C, no hold time. Image a), b), and c) picture the border where the cathode meets the electrolyte, while image b), d), and f) picture the surface of the applied cathode. The scale bars in the images are different.



(a)



(b)



(c)

FIGURE 4.21: SEM micrographs of a cross section of the cathode-electrolyte interface. The samples pictured were fired at; a) 700 °C with no hold time, b) 700 °C for 1 hour, and c) 800 °C with no hold time. The scale bars in the images are different.

For the cross section images in Figure 4.21, the light layer at the bottom is the CGO electrolyte, the thin layer is the cathode, and the darker area at the top of each image is the epoxy the pellet was cast in before imaging. The cathode appears to be 1 to 2 μm thick. The thickness varies, but overall the layer is continuous in all samples. Due to the samples being cast in epoxy, the porosity of the cathode is difficult to evaluate from these images. The electrolyte however, appears sufficiently dense, which corresponds to the 94% density measured by Archimedes' method.

Figure 4.21 (a) shows the cross section of the sample fired at 700 $^{\circ}\text{C}$ with no hold time. The delamination of the cathode from the electrolyte is clearly visible as a darker line at the interface. Despite delamination from the electrolyte, the cathode layer still appears continuous. The sample imaged in Figure 4.21 (b) was also fired at 700 $^{\circ}\text{C}$, but for a duration of 1 hour. There appears to be no delamination, and the interface between cathode and electrolyte is even and well adhered. The image in Figure 4.21 (c) is of the sample fired at 800 $^{\circ}\text{C}$ with no hold time. The cathode is well adhered to the electrolyte and any difference from the sample fired at 700 $^{\circ}\text{C}$ for 1 hour is difficult to detect.

Distribution of cations at the interface

The recorded energy-dispersive X-ray spectroscopy line scans for the three fabricated symmetric cells are shown in Figure 4.22, 4.23, and 4.24 for the samples fired at 700 $^{\circ}\text{C}$ with no hold time, 700 $^{\circ}\text{C}$ for 1 hour, and 800 $^{\circ}\text{C}$ with no hold time, respectively. The scans are recorded across the interface between cathode (left) and electrolyte (right).

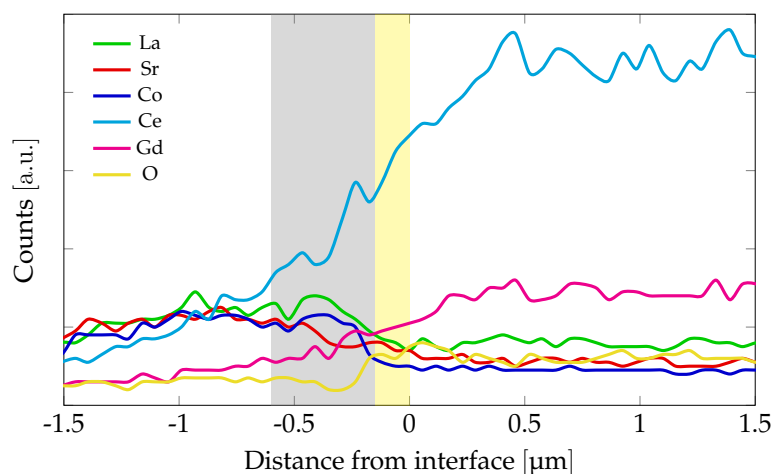


FIGURE 4.22: Line scan of the symmetric cell fired at 700 $^{\circ}\text{C}$ with no hold time. The cathode is on the left side and the electrolyte is on the right. The mutual diffusion zone is shaded grey. The yellow shading indicates the gap between the cathode and electrolyte due to delamination.

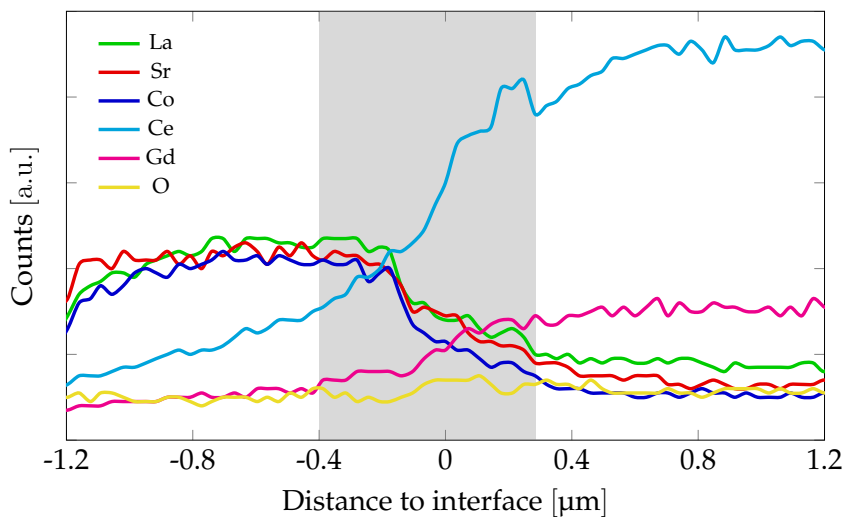


FIGURE 4.23: Line scan of the symmetric cell fired at 700 °C for 1 hours. The cathode is on the left side and the electrolyte is on the right. The mutual diffusion zone is shaded grey.

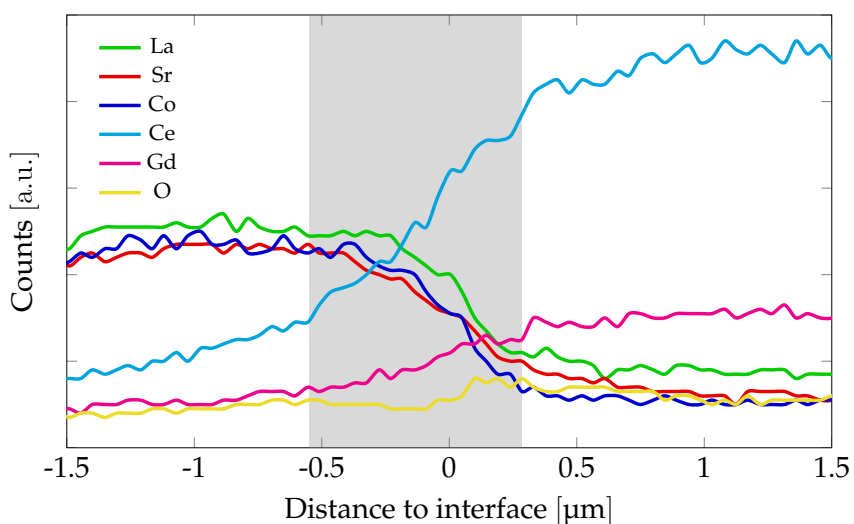


FIGURE 4.24: Line scan of the symmetric cell fired at 800 °C with no hold time. The cathode is on the left side and the electrolyte is on the right. The mutual diffusion zone is shaded grey.

All line scans appear to show the mutual diffusion of the various elements present in the cell. The interior of the cathode and electrolyte both have homogenous chemical compositions. However, the area on either side of the interface consists of a region in which the cations migrate across the grain boundaries and into adjacent grains. All elements have similar diffusion lengths, and this forms a mutual diffusion zone, which is shaded grey in the figures. The length of diffusion varies with the firing temperature and time used to fabricate each cell. The diffusion zone is approximately 400, 700, and 900 nm wide for the samples fired at 700 °C for 0 hours, 700 °C for 1 hour, and 800 °C for 0 hours, respectively. The element maps for each sample are included in Appendix A to give a complete picture of the cathode/electrolyte interface. Formation of secondary phases at the interface was not detected.

4.12 Area specific resistance

The symmetric cells were assessed by electrochemical impedance spectroscopy with a pure oxygen atmosphere. The measurements were conducted at 600, 700 and 800 °C. Figure 4.25 shows the impedance data recorded for the symmetric cell fired at 800 °C with no hold time. To better visualise the effect of temperature on the area specific resistance (ASR), the data in Figure 4.25 have been normalised. The original Nyquist plots for each measurement are included in Appendix B. The ASR estimated from the experimental data (ASR_{exp}) are listed in Table 4.8, and is observed to decrease with increasing measurement temperature.

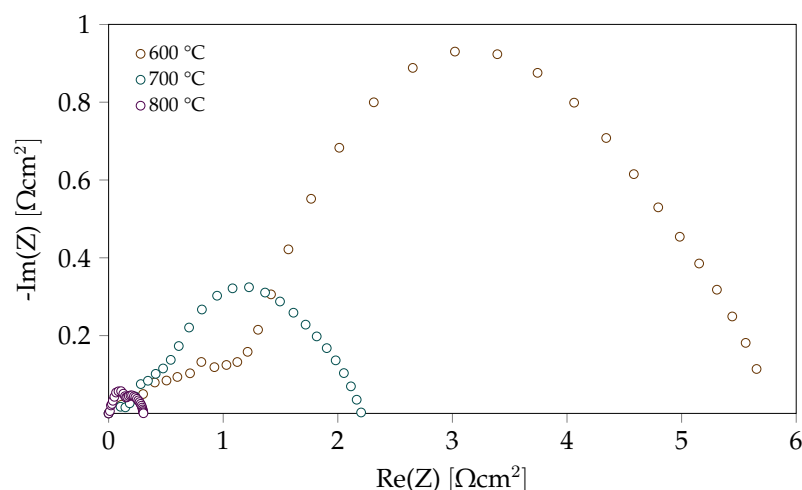


FIGURE 4.25: Electrochemical impedance data recorded at 600, 700, and 800 °C in pure oxygen for a symmetric cell fired at 800 °C with no hold time. The data have been normalised.

TABLE 4.8: Area specific resistance (ASR) calculated for the symmetric cell fired at 800 °C with no hold time. ASR_{exp} is the value determined directly from the Nyquist plots, while ASR_{fit} was determined by fitting the impedance data to equivalent circuits.

Temperature [°C]	ASR_{exp} [Ωcm^2]	ASR_{fit} [Ωcm^2]
600	2.2	3.02
700	1.1	1.27
800	0.2	0.32

A comparison of the measured impedance data and the fit obtained by modelling, using the equivalent circuit in Figure 3.3, is shown in Figure 4.26. The data in the figure was measured at 800 °C. The fitted data for measurement temperatures of 600 and 700 °C are included in Appendix C. The equivalent circuit used to model the data appears to be a good fit and the obtained values from the modelling, ASR_{fit} , are listed in Table 4.8.

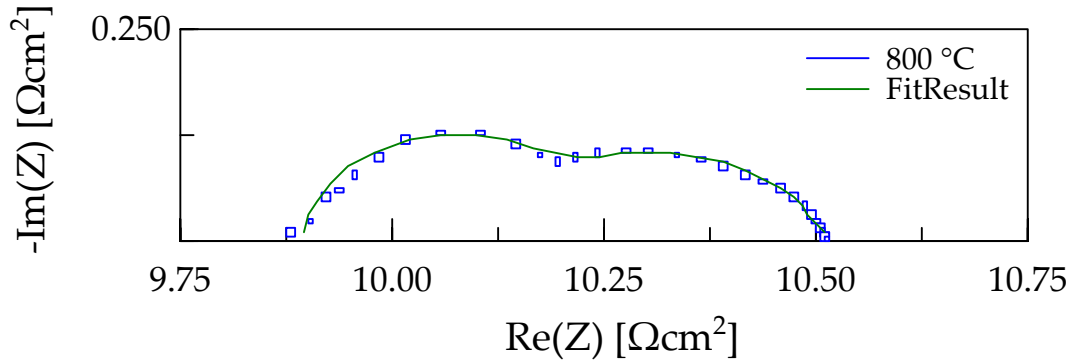


FIGURE 4.26: Comparison of the measured impedance data and the fit obtained using an equivalent circuit. The data were measured at 800 °C, for the symmetric cell fired at 800 °C with no hold time.

Figure 4.27 and 4.28 show Nyquist plots of the impedance data recorded for the same $\text{Ce}_{0.8}\text{Gd}_{0.2}\text{O}_2$ -electrolyte pellet with air and oxygen as the respective atmospheres.

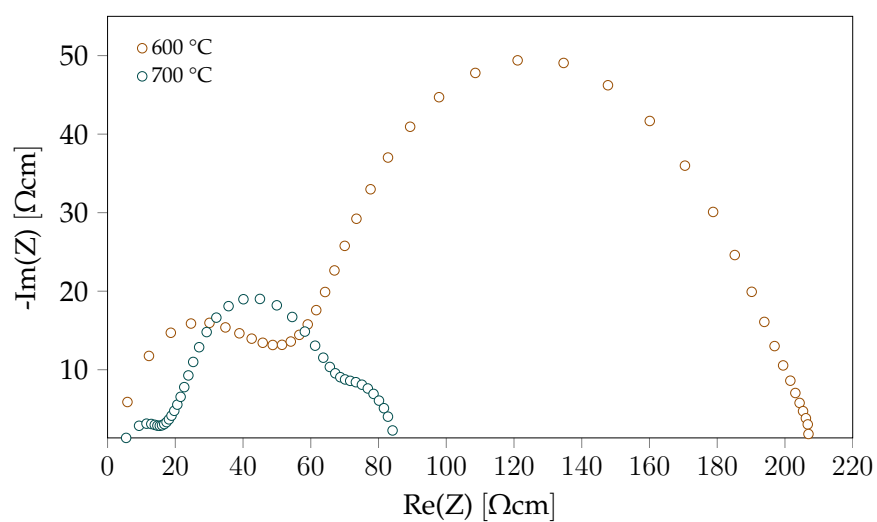


FIGURE 4.27: Electrochemical impedance data recorded at 600 and 700 °C in air for a representative $\text{Ce}_{0.8}\text{Gd}_{0.2}\text{O}_2$ electrolyte pellet.

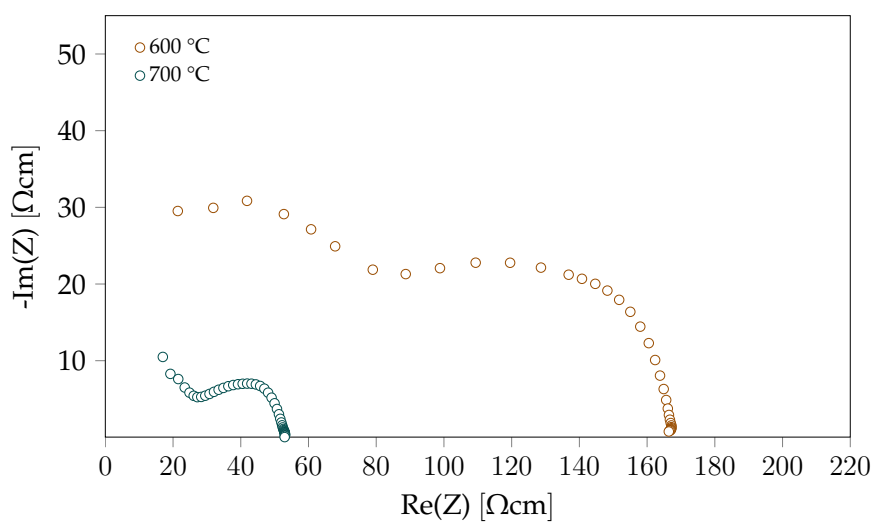


FIGURE 4.28: Electrochemical impedance data recorded at 600 and 700 °C in pure oxygen for a representative $\text{Ce}_{0.8}\text{Gd}_{0.2}\text{O}_2$ electrolyte pellet.

The resistance decreases with increasing temperature for both measurements. In other words, the electrolyte conductivity increases at higher temperatures. Both measurements show the effect of bulk and grain boundary resistance, with some overlap of the respective semi circles.

The different shapes and values in the Nyquist plots are suspected to be due to an instrument calibration performed between the two measurements. It is believed that this calibration affected all subsequent measurements, including those performed on the symmetric cell in Figure 4.25. Acquiring reproducible data for the cells fired at 600 and 700 °C was not possible due to time constraints.

Chapter 5

Discussion

5.1 Phase purity

Preliminary analysis

All powders investigated during the preliminary analysis, except that from batch CA1-HC, contained a secondary phase in addition to the primary $\text{La}_{0.6}\text{Sr}_{0.4}\text{CoO}_3$ -phase. The secondary phase is identified as Co_3O_4 , as indicated in the XRD pattern for the as-prepared powder in Figure 4.2. With the exception of the identified Co_3O_4 -phase, the difference in phase purity appears to be minimal and independent of both the concentration of the precursor solution, and the citric acid concentration. A slight increase in crystallinity for the samples prepared with a citric acid:LSC ratio of 1:1, is visible in the figure.

After calcination at 800 °C for 6 hours, both the primary and secondary phases experience an increase in crystallinity due to grain growth, as seen in Figure 4.3. Additionally, there is a clear splitting of the peaks at higher diffraction angles for the primary phase $\text{La}_{0.6}\text{Sr}_{0.4}\text{CoO}_3$, observed only for samples containing Co_3O_4 .

The formation of secondary phases during spray pyrolysis can be caused by the segregation of the cations in the precursor solution. Cation segregation during powder formation of multicomponent oxides occurs due to differences in solubility. The pH of the solution and the water activity also affect precipitation. It is possible to stabilise the cations in the solution by addition of complexing agents. Complexing agents increase the solubility of the cations, can cause formation of stable three dimensional networks, and increase the viscosity of the precursor solution. If the solution is not stable, the less soluble cations will precipitate, enabling the formation of secondary phases. Additionally, the precipitation of one cation alters the composition of the primary phase.

The results from the preliminary analysis suggest that formation of Co_3O_4 is enabled by the precipitation of Sr, which is the least soluble cation in the $\text{La}_{0.6}\text{Sr}_{0.4}\text{CoO}_3$ composition. The split peaks at 41°, 59°, and 69° (observed in Figure 4.3) after calcination, indicate that the primary phase in samples containing Co_3O_4 has a high degree of rhombohedral symmetry. In comparison, the primary phase in the sample that does not contain Co_3O_4 , has a less distorted structure, closer to cubic symmetry. The difference

in crystal structure indicates that the four samples containing Co_3O_4 have a composition further to the left in the phase diagram in Figure 2.6, due to the segregation of Sr.

One possible explanation for Sr precipitation is that the concentration of the final precursor solution passed the solubility limit of Sr. However, that phase pure $\text{La}_{0.6}\text{Sr}_{0.4}\text{CoO}_3$ has been successfully prepared from solutions of even higher concentration, indicates that a more thorough explanation is necessary.

A critical difference in the synthesis routes appears to be the most likely cause. The batches used in the preliminary analysis were prepared by direct addition of citric acid to the separate nitrate solutions. The dissolution of citric acid in water is an endothermic reaction. As solubility decreases at lower temperatures, this could be the potential cause for precipitation of Sr. A direct addition of citric acid would also cause the water activity to diminish, which in turn lowers the solubility of Sr-ions in the solution further.

Additionally, the precursor solutions were left uncovered during production of samples used in the preliminary analysis. It is possible that the evaporation of water could cause a slight increase in concentration. This could in combination with the previously mentioned effects, cause the solution to pass the solubility limit for strontium. The phase pure batch CA1-HC was 25 times larger than the other batches, and was the first to be produced. It is possible that the large volume of the batch and the short time available for evaporation of water, limited the segregation of Sr and ensured the phase purity of this batch.

Which factor had the largest total effect on the formation of the secondary phase is difficult to determine, and adjustments should be made to limit each of these factors when dealing with low solubility cations in the future.

Phase purity of final batches

The XRD patterns for all as-prepared samples are shown in Figure 4.7. The final samples were all identified as phase pure $\text{La}_{0.6}\text{Sr}_{0.4}\text{CoO}_3$ (LSC), with the exception of a small peak at 25° for CA1-V₄, identified to be SrCO_3 . Calcination at 750°C for 6 hours increased the crystallinity of all samples, and removed the carbonate present in sample CA1-V₄, as shown in Figure 4.8.

The concentration of the precursor and the ratio of citric acid used in each batch appears to have little effect on the phase purity, as even a CA:LSC ratio of 0.1:1 is sufficient to achieve phase pure powder. This follows the trend previously reported by Høyem.^[4] She found that increasing the citric acid ratio from 1 to 5 appeared to have no effect on the phase purity of $\text{La}_{0.6}\text{Ca}_{0.4}\text{CoO}_3$ -powder prepared by spray pyrolysis.

When comparing the diffraction patterns for the final samples to those in the preliminary analysis, it is evident that the final samples are similar to sample CA1-HC with a slight broadening, but no splitting of the high angle peaks. This suggests a rhombohedral symmetry, close to the phase boundary, which corresponds to the symmetry

expected for $\text{La}_{0.6}\text{Ca}_{0.4}\text{CoO}_3$ according to the phase diagram in Figure 2.6.

The carbonate in sample CA1-V₄ is most likely caused by the increased amount of CO_2 present in the furnace due to combustion of the larger amount of organic additive in this sample. Aiming to reduce the amount of organic material in the precursor could limit the formation of carbonates, and additionally reduce the emissions caused by powder production. Additionally, the reduced need for post production heat treatment would increase the cost efficiency of spray pyrolysis.

The diffraction patterns for the samples calcined at various temperatures, shown in Figure 4.9 and 4.10 have identical phase compositions. However a slightly higher crystallinity is recorded for sample CA01-V₄. The most likely explanation is that the morphology of the powder causes preferential packing during sample preparation. Both samples remain phase pure up to and including calcination temperatures of 900 °C. However, there appears to be a phase transition at temperatures close to 1200 °C. The XRD pattern recorded at this temperature exhibits some additional peaks, and a clear distortion of the high angle reflections. The alumina crucible used during calcination at this temperature had blue discolouration where it had been in contact with the powder. This suggests that diffusion of cobalt could be the cause for the structural change.

5.2 Yield and volume density

The resulting yield for each batch varied greatly, both for the samples analysed in the preliminary investigations and for the final samples. The values are listed in Table 4.1 and 4.2. Compared to the expected yield for spray pyrolysis (70% for large volumes of precursor, and 50 % for smaller volumes), most of these values are reasonable. The batches with the lowest yield (under 25%) all experienced issues during production that explains the loss.

There appears to be some trends in the resulting yield and volume density that are shared by both the preliminary and final samples. An increase in the amount of citric acid results in a slightly lower volume density. Additionally a precursor solution of lower concentration results in lower volume density and a higher yield. The effect on volume density corresponds to the trends in the morphology of the eggshell-agglomerates observed by SEM. The samples with thinner core shells and a more homogenous size distribution have a higher apparent volume density than those with denser shells.

The low yield for sample CA0.1-V₄ is explained by a necessary change of the air filter in the middle of the spraying. It is uncertain why this affected the volume density to such an extent. The very high yield of CA1-V₄ could be attributed to the presence of carbonate in the sample, contributing additional weight from the carbon that would normally leave the furnace as gas. Additionally, the recorded thermogravimetric data in Figure 4.6 shows a larger weight loss for this sample before the temperature reached ~100 °C, which corresponds to a higher water content.

5.3 Morphology of the as-prepared powder

The SEM images in Figure 4.12 show the morphology of the as-prepared powder agglomerates. All samples contained the characteristic eggshell-morphology of spray pyrolysed powder, but had core shells of varying thickness and different size distributions.

The general trend indicates that the lower concentration precursor solutions form thinner shells. A similar effect on the core shells is observed when increasing the amount of citric acid in the precursor. The samples containing a low amount of CA exhibit thin core shells only for the smallest particles, while the samples with a 1:1 CA:LSC ratio appears to have thinner shells on particles of all sizes. Additionally, these samples have noticeably fewer large, uneven agglomerates.

This appears to be in contrast to the findings for $\text{La}_{0.6}\text{Ca}_{0.4}\text{CoO}_3$ (LCC), reported by Høyem^[4]. She found that a higher concentration of complexing agents gave denser, more uniform spheres when the citric acid:LCC ratio was increased from 1 to 5. However, she also reported that powder made without the addition of citric acid, had thicker shells, with a less homogenous size distribution than the powder made with a CA:LCC ratio of 1:1.

A comparison of the findings reported by Høyem to the results presented in this work, suggests that the addition of citric acid to the precursor has a positive effect on the particle morphology until a threshold concentration is reached. Increasing the CA concentration beyond this point causes the formation of thicker crusts and increasingly uniform agglomerates, which are more difficult to break down in subsequent milling steps.

There are multiple mechanisms during the evaporation step of the spray pyrolysis process that affect size, size distribution, porosity and shape of the resulting powder agglomerates. Which mechanisms that are dominant will vary depending on solute concentration and evaporation rate, the size of the droplets, and the precursor's critical supersaturation. The dominating mechanisms can therefore be difficult to identify.

Formation of a crust, rather than uniform volume precipitation, is because solute diffusion is slower than the evaporation rate at the temperatures that was used during powder production. This difference causes the solute concentration on the surface of the droplet to reach a critical supersaturation, causing the cations on the surface to precipitate out, while the core remains liquid. The hollow spheres may then be explained by the formation of bubbles as the liquid core experiences a steep rise in temperature after surface precipitation has formed an outer crust.^[67]

The varying sizes of powder agglomerates in the samples could be related to the ease at which a nozzle atomises solutions of different viscosities, as the size of the droplet entering the furnace could have a direct effect on the size of the resulting agglomerate. The droplet size does however not affect whether the final agglomerates are

solid or hollow, because the diffusion and evaporation time constants are proportional to the square of the droplet radius.^[67]

Chen et al.^[68] investigated the effect of the precursor solution concentration on particle morphology for ZrO_2 - and CeO_2 -powder prepared by spray pyrolysis. They concluded that the solubility of the precursor largely affected the particle morphology, but that a reduction of the precursor concentration to 0.01 wt% resulted in spherical, monodispersed particles, regardless of solubility. None of the batches investigated in this work had precursor solutions of such low concentrations, and it could be worth investigating if a similar effect is observed for LSC. A larger volume of the precursor solution would mean longer production times, and an eventual positive effect on the powder morphology should be weighed against the increased production cost.

5.4 Particle size and surface area

Effect on specific surface area

The specific surface area (SSA) for the as-prepared powders increases with decreasing concentration of the precursor solution showing a clear trend, as seen in Figure 5.1.

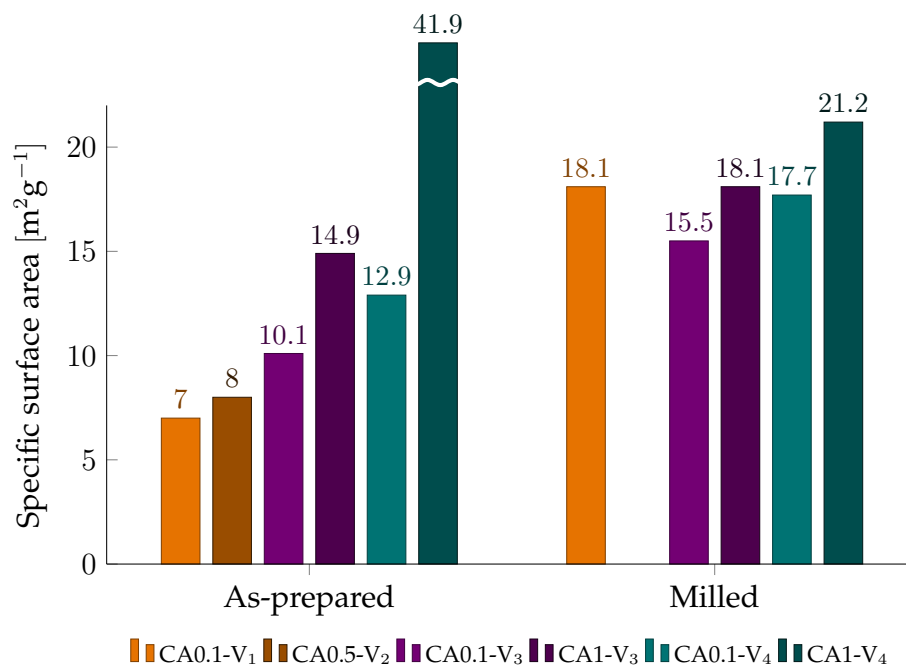


FIGURE 5.1: Comparison of the variations in specific surface area measured for the as-prepared and milled powder.

When comparing the samples made from equal precursor concentrations, it is evident that the SSA also increases with increasing concentration of citric acid. The variation in SSA for the as-prepared powder ranges between 7.0 and 41.9 m²g⁻¹, where CA1-V4 has the largest observed SSA of all samples.

After calcination the trend remains similar, but with decreased SSA for all samples. The decrease in SSA is due to the coarsening caused by particle growth at high temperatures, and is as expected for ceramic oxide powders.^[61]

After milling for 48 hours, the SSA appears independent of precursor concentration. However the samples made from precursors with the most citric acid, still have the highest SSA, as seen in Figure 5.1. The variation in SSA after milling ranges between 15.5 and 21.2 m²g⁻¹, where CA1-V4 is the sample with the largest measured SSA.

Effect on crystallite and particle size

As expected, the crystallite size calculated from the XRD patterns using Equation 10, is smaller than the size of the particles measured by gas adsorption. After calcination and milling, the values (listed in Table 4.4) become very similar for most samples. The values indicate that each powder particle might consist of 2-4 crystallites, and that nanometer sized powder was obtained for all samples. This is supported by the average particle diameter calculated from the SEM images in Figure 4.13, which varies between 85 and 121 nm, for sample CA0.1-V₁ and CA0.1-V₃, respectively.

Particle size distribution and an evaluation of the milling procedure

The SEM image in Figure 4.13 shows that most of the core shells have been broken down during milling. The small particles appear relatively even in size with little variation between the samples. However some unbroken agglomerates of different sizes are present in all samples, with the largest amount found in sample CA0.1-V₃.

The particle size estimated from the SEM image of the milled powder for this sample in (Figure 4.13 (b)) was the largest of all samples. It is possible that the milling procedure was less effective for this sample, possibly due to the morphology of the as-prepared powder agglomerates. As Figure 4.12 shows, the as-prepared powder from batch CA0.1-V₃ had the largest, most uneven powder agglomerates. Additionally, the evaluation of the particle size distribution (PSD) in Figure 4.14 shows that this sample stands out having a bimodal distribution confirming the presence of large, unbroken agglomerates.

The SEM images in Figure 4.12 show that the sample CA0.1-V₁ has the most similar appearance to sample CA0.1-V₃. The PSD measured for this sample has a broader volume distribution, with larger particles than the three remaining samples, which, as seen in Figure 4.14, all have relatively similar distributions. These results indicate that smooth spheres, with thin shells and a uniform size distribution could be easier to mill down than large, uneven ones.

As this could reduce the time needed for milling and improve the cost efficiency of the post production of powders prepared by spray pyrolysis, the effect was investigated further, by evaluating the evolution of the particle size distribution for sample CA0.1-V₄ and comparing it to CA0.1-V₃.

Figures 4.15 and 4.16 show the respective particle size distributions. For sample CA0.1-V₄ the PSD became narrower, and the median particle size increased evenly with the duration of milling. However, for CA0.1-V₃ a large increase in PSD was observed after 48 hours, probably due to agglomeration of the powder during sample preparation. If this is the case, this could also be the explanation for the bimodal distribution observed for this sample in Figure 4.14. The SEM images taken of the measured samples are shown Figure 4.12. The gradual evolution from partly broken down shells to fine powder is observed for CA0.1-V₄ in (a), but a similar trend can not be observed for CA0.1-V₃ in (b). However, the image taken after 48 hours shows the smallest particles for this sample as well.

As all samples were measured using the particle volume distribution, the results are difficult to compare directly to the previously calculated values from the BET, XRD, and SEM results. The reported volume distribution instead gives a good indication of which particle size holds the most volume for each sample.

In the evaluation of these results it is important to consider that this type of analysis is highly susceptible to sampling errors, as only one sample was taken from each batch at each interval. The result is possibly affected by how homogenous the milling slurry was at the point the sample was collected. Additionally, reproducible PSD measurements were difficult to achieve due to observed agglomeration of the powder, if too much was added to the measuring instrument. The ease of agglomeration for particles of nanometer scale could easily affect the result during measurements, and it is possible that agglomeration was already present in the samples at earlier stages.

To properly evaluate the milling procedure, a better method (primarily aimed at increasing the reproducibility of the results and avoiding sampling errors) should be considered.

5.5 Evaluation of airbrushing as a deposition method

To ensure even deposition of the LSC-cathode, the stability of a dispersion of LSC-powder was investigated. The prepared dispersions were all relatively stable for 6 hours. However, after 6 hours, a sediment layer was visible. After evaluating the cathode, it is believed that sedimentation might have occurred earlier, but that this was difficult to detect due to the large degree of very small particles remaining in the upper layer of the dispersion. As it was this upper layer that was transferred to the airbrush, the dispersion had a very low wt% particles. This resulted in a very thin cathode measuring 1-2 μm , one tenth of the expected thickness.

It is possible that Dolacol was unsuited as a dispersant for LSC and that the lack of steric stabilisation caused the particles to agglomerate, and subsequently form a sediment layer. Another factor on dispersion stability is the pH. The dispersion pH was not evaluated in this work. It is possible that an adjustment of the pH might have caused an increase in dispersion stability.

To gain better control over the preparation of the cathode, an evaluation of the suspension pH, viscosity, and the use of other dispersants should be conducted. Finding the right parameters for a stable suspension of appropriate particle size and wt% could aid in the preparation of thicker, more uniform cathodes.

As the deposition of the cathode was done by manual airbrushing several parameters are introduced that could affect the thickness of the cathode. The deposition distance and speed of application is difficult to control and could vary between layers. Using a mounted airbrush with set movement and a proper sample holder would make it possible to duplicate the symmetric cells, and ensure minimal difference between cells fabricated at different times. Another deposition method that could be investigated is simply using a paint brush to apply the cathode layer onto the electrolyte.

5.6 Evaluation of firing temperature for symmetric cells

Three symmetric cells were fabricated and fired using different temperature programs. The deposited cathode layer was found to be continuous for all three cells, despite being only 1-2 μm thick. However, the different temperature programs caused a different degree of adhesion between the cathode and the electrolyte.

The SEM image in Figure 4.21 shows that the lowest firing temperature of 700 °C with no hold time was not sufficient for proper adhesion, and the cathode in this cell had delaminated from the electrolyte. It is uncertain whether delamination was caused by the impact when the pellet was cleaved, by epoxy penetrating the pores, or for other reasons. The other firing programs show well adhered cathodes and are deemed to be sufficient.

The results from EDS indicate the possible cation diffusion, with increasing diffusion lengths at higher temperatures. This widening of the diffusion zone is expected when temperature increases. However, due to the nature of the measurement, where the EDS measures a broad area of the sample, an overlap will be created at the interface. It is possible that the diffusion zone observed in Figures 4.22, 4.23, and 4.24 is caused by this overlap in the measured data for each point, and that diffusion at the interface does not occur.

Alternatively, the observed effect could be caused by the morphology at the interface. An uneven electrolyte surface would appear like the graded zone observed in the figures, and the contribution of nearby grains would be detected on the EDS scan. A more accurate analysis could be conducted by STEM EDX. This would make it possible

to confirm if diffusion takes place between grains in the cathode and electrolyte.

5.7 Area specific resistance

The area specific resistance (ASR) for the LSC cathodes were calculated from the equivalent circuit used to fit the measured impedance data. The fitted data for the symmetric cell fired at 800 °C is shown in Figure 4.26, and matches the measured data reasonably well. To obtain a better fit, additional circuit elements could be included. However attributing these elements to real processes in the material would be difficult.

The ASR from the fitting of the impedance data was determined to 3.02, 1.27, and 0.32 Ωcm^2 when measured at 600, 700, 800 °C respectively. The ASR is observed to decrease with increasing measurement temperature, as expected due to the high activation energy of the oxygen reduction reaction. The values are higher than what is expected for LSC cathodes.

The high ASR could be explained by the thickness of the cathode, as a thickness as low as 1-2 μm would mean fewer available reaction sites for the oxygen reduction reaction. As the porosity of the cathode was difficult to evaluate from the SEM image 4.21, it is possible that undiscovered variations in the porosity affected the result as well.

Table 2.4 contains some reported values measured for symmetric cells fabricated by various methods. Due to the direct effect of the cathode's microstructure on its properties,^[7] a direct comparison of the values is difficult. However, the ASR reported by Tao et al.^[52] was measured for spray deposited cathodes which are similar to those prepared in this work. They reported values for the ASR of 0.17 Ωcm^2 measured at 700 °C, and 0.07 Ωcm^2 measured at 750 °C. These values are lower than those determined in this work. However, the cathodes prepared by Tao et al. had smaller particle sizes and a thickness of 10 μm , increasing the amount of available reaction sites. They also fired the cell at a higher temperature for a longer duration (950 °C for 2 hours). The increased sintering of these cathodes could be the cause of better adhesion to the electrolyte and as a consequence a lower interface resistance.

The dilatometry curve for the spray pyrolysed LSC in Figure 4.18 shows that sintering initiates around 800 °C. Hayd et al.^[49] observed sintering of LSC nanopowders at temperatures as low as 700 °C, but for a particle size of 17 nm. This is considerably smaller than the powder used in this work and would have an effect on the observed sintering behaviour.^[61]

A comparison of the ASR determined in this work, and that reported by Tao et al. suggests that the firing temperature and time should be increased to ensure sintering and a good connection between the cathode and the electrolyte. As the cross section images in Figure 4.21 (c) shows, there is a presence of small cracks at the interface, which could explain the higher ASR.

The shape of the Nyquist plots in Figure 4.25 are different for the various measurement temperatures. This indicates that different chemical processes dominate the resistance of the cathode at different temperatures. Identifying each of these processes requires further investigation and is beyond the scope of this work.

For the electrolyte in Figure 4.27 and 4.28, the two observed semi circles are expected to be due to the bulk (high frequency) and grain boundary resistance (low frequency) of the material.^[53] The measured electrolyte had a thickness of 0.8 mm and a relatively high resistance. The ohmic loss in the electrolyte can be reduced by fabrication of thinner disks. As a shorter migration distance for the oxygen ions is beneficial to the properties of the cell.

Chapter 6

Concluding remarks and further work

6.1 Conclusion

The effect of the precursor concentration and the concentration of citric acid (CA) on the properties of $(\text{La}_{0.6}\text{Sr}_{0.4})_{0.99}\text{CoO}_3$ (LSC), prepared by spray pyrolysis, has been investigated.

The morphology of the as-prepared powders was found to vary with precursor concentration and amount of citric acid used. More evenly sized agglomerates, and thinner core shells were observed for powders produced from low concentration precursor solutions with high CA:LSC ratios.

Post calcination, all samples were found to be phase pure LSC with rhombohedral symmetry. The highest surface area, with a value of $21.2 \text{ m}^2\text{g}^{-1}$, was measured for the sample made from the precursor solution with the lowest concentration and highest CA:LSC ratio. The particle size distribution was found to be the most narrow for the high concentration sample with the highest CA:LSC ratio. This sample also had the lowest median particle size. The crystallite size calculated from the XRD patterns varied from 42 to 45 nm. The particle size measured from SEM images had larger variations with the smallest value, 85 nm, measured for the sample from the high concentration batch with the lowest ratio of CA:LSC.

Symmetric cells with LSC cathodes on $\text{Ce}_{0.8}\text{Gd}_{0.2}\text{O}_2$ (CGO) electrolytes were fabricated by spray deposition and fired at various temperature programs. The deposited cathodes were uniform, with a thickness of 1-2 μm . A firing temperature of 800 °C with no annealing time was found to give good adhesion between cathode and electrolyte. The cell was analysed by electrochemical impedance spectroscopy in oxygen atmosphere at 600, 700, and 800 °C, and the area specific resistance was determined to 3.02, 1.27, and 0.32 Ωcm^2 respectively.

The obtained results indicate that LSC powders produced by spray pyrolysis are suitable as cathode materials for use in intermediate temperature solid oxide fuel cells.

However, the evaluation of the symmetric cells in this work has severe limitations and further investigations into the fabrication and properties of such cells are needed.

6.2 Further work

Evaluation of milling procedure

To properly evaluate the milling procedure used for ceramic powders, several steps should be taken to avoid sampling errors and ensure good reproducibility of the results. Comparable powder samples should be prepared and accurately weighed, so the same amount of powder is milled for each sample. The number of milling balls and the amount of fluid added to the flask should be identical between the samples. Additionally, preparing several parallels for each powder sample would limit the potential sampling errors. When removing slurry from the flasks, several samples should be taken, ideally from both the top and bottom of the slurry, to ensure that they are representative. The conducted measurements by laser diffraction should be performed according to a suitable ISO-standard, to ensure good reproducibility and accuracy.

Fabrication of symmetric cells

The low thickness of the cathodes prepared in this work suggests that a improving the method for fabrication of the symmetric cells should be investigated. The problems encountered in this work are attributed to the stability of the powder dispersion used to airbrush the cathodes and to the limitations of airbrushing as a technique.

Further investigation of dispersion stability should be performed. Determining the compatibility of the dispersing agents with the ceramic powder is essential for good steric stabilisation. Additionally the pH and viscosity of the dispersion could be adjusted to determine the effect these factors have on the stability of the dispersion.

Improving the thickness and porosity of the cathode, and ensuring a more even cathode layer should be in focus when preparing symmetric cells. Investigating other deposition methods, or varying the parameters used with the hand held airbrush could achieve a higher quality cathode.

Evaluation of symmetric cells

A larger number of cells should be fabricated and characterised to ensure reproducible results. A wider range of temperature programs used to fire the cells could be investigated to evaluate the effect of fabrication temperature on the area specific resistance of the cathode. Firing temperatures between 800 and 950 °C, with a hold time of 1-2 hours appears to be sufficient to ensure good adhesion between an LSC cathode and a CGO electrolyte.

The impedance measurements for the cells could be performed at even lower temperatures (500 °C) and in different atmospheres, either air, or with varying oxygen partial pressures to investigate the effect this has on the cell properties.

Bibliography

- [1] Z. P. Shao, W. Zhou, and Z. H. Zhu. "Advanced synthesis of materials for intermediate temperature solid oxide fuel cells". In: *Progress in Materials Science* 57.4 (2012).
- [2] A. Kumar, P. S. Devi, A. Das Sharma, and H. S. Maiti. "A novel spray-pyrolysis technique to produce nanocrystalline lanthanum strontium manganite powder". In: *Journal of the American Ceramic Society* 88.4 (2005).
- [3] T. Kinoshita, A. Arastoo, H. Maruko, and M. Adachi. "Synthesis of Porous Particles of SOFC Anode and Cathode Materials by Citric Acid-Addition Ultrasonic Spray Pyrolysis (CA-USP)". In: *Aerosol Science and Technology* 48.10 (2014).
- [4] S. S. Høyem. *Optimised microstructure of La_{0.6}Ca_{0.4}CoO₃ for solid oxide fuel cell cathodes*. 2015.
- [5] W. R. Grove. "On a new voltaic combination". In: *Philosophical Magazine Series 3* 13.84 (1838).
- [6] H. H. Mobius. "On the history of solid electrolyte fuel cells". In: *Journal of Solid State Electrochemistry* 1.1 (1997).
- [7] J. A. Kilner and M. Burriel. "Materials for Intermediate-Temperature Solid-Oxide Fuel Cells". In: *Annual Review of Materials Research*. Ed. by D. R. Clarke. Vol. 44. Annual Review of Materials Research. 2014.
- [8] B. C. H. Steele. "Material science and engineering: The enabling technology for the commercialisation of fuel cell systems". In: *Journal of Materials Science* 36.5 (2001).
- [9] S. C. Singhal. "Advances in solid oxide fuel cell technology". In: *Solid State Ionics* 135.1-4 (2000).
- [10] D. J. L. Brett, A. Atkinson, N. P. Brandon, and S. J. Skinner. "Intermediate temperature solid oxide fuel cells". In: *Chemical Society Reviews* 37.8 (2008).
- [11] J. B. Hansen, F. Fock, and H. H. Lindboe. "Biogas Upgrading: By Steam Electrolysis or Co-electrolysis of Biogas and Steam?" In: *Solid Oxide Fuel Cells* 13. Ed. by T. Kawada and S. C. Singhal. Vol. 57. ECS Transactions. 2013.
- [12] A. Lashtabeg and S. J. Skinner. "Solid oxide fuel cells - a challenge for materials chemists?" In: *Journal of Materials Chemistry* 16.31 (2006).

- [13] University of Cambridge. *Fuel Cells*. 2006. URL: <http://www.doitpoms.ac.uk/tlplib/fuel-cells/printall.php> (visited on 07/07/2016).
- [14] B. C. H. Steele. "Appraisal of $\text{Ce}_{1-y}\text{Gd}_y\text{O}_{2-y/2}$ electrolytes for IT-SOFC operation at 500 °C". In: *Solid State Ionics* 129.1-4 (2000).
- [15] T. Ishihara, H. Matsuda, and Y. Takita. "Doped LaGaO_3 perovskite-type oxide as a new oxide ionic conductor". In: *Journal of the American Chemical Society* 116.9 (1994).
- [16] J. Larminie and A. Dicks. *Fuel Cell Systems Explained*. John Wiley and Sons Ltd, 2003.
- [17] S. W. Tao and J. T. S. Irvine. "Discovery and characterization of novel oxide anodes for solid oxide fuel cells". In: *Chemical Record* 4.2 (2004).
- [18] I. Kivi, P. Moller, H. Kurig, S. Kallip, G. Nurk, and E. Lust. "Development of porous cathode powders for SOFC and influence of cathode structure on the oxygen electroreduction kinetics". In: *Electrochemistry Communications* 10.10 (2008).
- [19] L. Baque, A. Caneiro, M. S. Moreno, and A. Serquis. "High performance nanostructured IT-SOFC cathodes prepared by novel chemical method". In: *Electrochemistry Communications* 10.12 (2008).
- [20] S. Pathak, J. Kuebler, A. Payzant, and N. Orlovskaya. "Mechanical behavior and electrical conductivity of $\text{La}_{1-x}\text{Ca}_x\text{CoO}_3$ ($x = 0, 0.2, 0.4, 0.55$) perovskites". In: *Journal of Power Sources* 195.11 (2010).
- [21] S. Uhlenbruck and F. Tietz. "High-temperature thermal expansion and conductivity of cobaltites: potentials for adaptation of the thermal expansion to the demands for solid oxide fuel cells". In: *Materials Science and Engineering B-Solid State Materials for Advanced Technology* 107.3 (2004).
- [22] D. A. Osinkin, D. I. Bronin, S. M. Beresnev, N. M. Bogdanovich, V. D. Zhuravlev, G. K. Vdovin, and T. A. Demyanenko. "Thermal expansion, gas permeability, and conductivity of Ni-YSZ anodes produced by different techniques". In: *Journal of Solid State Electrochemistry* 18.1 (2014).
- [23] A. Berenov, H. Wood, and A. Atkinson. "Evaluation of $\text{La}_{0.8}\text{Sr}_{0.2}\text{Cu}_{1-x}\text{Mn}_x\text{O}_y$ double perovskite for use in SOFCs". In: *Journal of the Electrochemical Society* 154.12 (2007).
- [24] E. O. Ahlgren and F. W. Poulsen. "Thermoelectric power and electrical conductivity of strontium-doped lanthanum manganite". In: *Solid State Ionics* 86-8 (1996).
- [25] R. A. De Souza and J. A. Kilner. "Oxygen transport in $\text{La}_{1-x}\text{Sr}_x\text{Mn}_{1-y}\text{Co}_y\text{O}_{3\pm\delta}$ perovskites - Part I. Oxygen tracer diffusion". In: *Solid State Ionics* 106.3-4 (1998).
- [26] K. Q. Huang and J. B. Goodenough. "A solid oxide fuel cell based on Sr- and Mg-doped LaGaO_3 electrolyte: the role of a rare-earth oxide buffer". In: *Journal of Alloys and Compounds* 303 (2000), pp. 454-464.

- [27] L. G. Cong, T. M. He, Y. A. Ji, P. F. Guan, Y. L. Huang, and W. H. Su. "Synthesis and characterization of IT-electrolyte with perovskite structure $\text{La}_{0.8}\text{Sr}_{0.2}\text{Ga}_{0.85}\text{Mg}_{0.15}\text{O}_{3-\delta}$ by glycine-nitrate combustion method". In: *Journal of Alloys and Compounds* 348.1-2 (2003).
- [28] L. W. Tai, M. M. Nasrallah, H. U. Anderson, D. M. Sparlin, and S. R. Sehlin. "Structure and electrical-properties of $\text{La}_{1-x}\text{Sr}_x\text{Co}_{1-y}\text{Fe}_y\text{O}_3$. 1. The system $\text{La}_{0.8}\text{Sr}_{0.2}\text{Co}_{1-y}\text{Fe}_y\text{O}_3$ ". In: *Solid State Ionics* 76.3-4 (1995).
- [29] D. Marinha, J. Hayd, L. Dessemond, E. Ivers-Tiffée, and E. Djurado. "Performance of $(\text{La,Sr})(\text{Co,Fe})\text{O}_{3-x}$ double-layer cathode films for intermediate temperature solid oxide fuel cell". In: *Journal of Power Sources* 196.11 (2011).
- [30] A. Esquirol, J. Kilner, and N. Brandon. "Oxygen transport in $\text{La}_{0.6}\text{Sr}_{0.4}\text{Co}_{0.2}\text{Fe}_{0.8}\text{O}_{3-\delta}/\text{Ce}_{0.8}\text{Ge}_{0.2}\text{O}_{2-x}$ composite cathode for IT-SOFCs". In: *Solid State Ionics* 175.1-4 (2004).
- [31] J. F. Vente, S. McIntosh, W. G. Haije, and H. J. M. Bouwmeester. "Properties and performance of $\text{Ba}_{1-x}\text{Sr}_x\text{Co}_{0.8}\text{Fe}_{0.2}\text{O}_{3-\delta}$ materials for oxygen transport membranes". In: *Journal of Solid State Electrochemistry* 10.8 (2006).
- [32] B. Wei, Z. Lu, X. Q. Huang, J. P. Miao, X. Q. Sha, X. S. Xin, and W. H. Su. "Crystal structure, thermal expansion and electrical conductivity of perovskite oxides $\text{Ba}_x\text{Sr}_{1-x}\text{Co}_{0.8}\text{Fe}_{0.2}\text{O}_{3-\delta}$ ($0.3 \leq x \leq 0.7$)". In: *Journal of the European Ceramic Society* 26.13 (2006).
- [33] L. Wang, R. Merkle, J. Maier, T. Acarturk, and U. Starke. "Oxygen tracer diffusion in dense $\text{Ba}_{0.5}\text{Sr}_{0.5}\text{Co}_{0.8}\text{Fe}_{0.2}\text{O}_{3-\delta}$ films". In: *Applied Physics Letters* 94.7 (2009).
- [34] J. Mastin, M. A. Einarsrud, and T. Grande. "Crystal structure and thermal properties of $\text{La}_{1-x}\text{Ca}_x\text{CoO}_{3-\delta}$ ($0 \leq x \leq 0.4$)". In: *Chemistry of Materials* 18.6 (2006).
- [35] A. J. Jacobson. "Materials for Solid Oxide Fuel Cells". In: *Chemistry of Materials* 22.3 (2010).
- [36] K. T. Lee and A. Manthiram. "Comparison of $\text{Ln}_{0.6}\text{Sr}_{0.4}\text{CoO}_{3-\delta}$ ($\text{Ln} = \text{La, Pr, Nd, Sm, and Gd}$) as cathode materials for intermediate temperature solid oxide fuel cells". In: *Journal of the Electrochemical Society* 153.4 (2006).
- [37] A. N. Petrov, O. F. Kononchuk, A. V. Andreev, V. A. Cherepanov, and P. Kofstad. "Crystal-structure, electrical and magnetic-properties of $\text{La}_{1-x}\text{Sr}_x\text{CoO}_{3-\delta}$ ". In: *Solid State Ionics* 80.3-4 (1995).
- [38] Y. Teraoka, T. Nobunaga, K. Okamoto, N. Miura, and N. Yamazoe. "Influence of constituent metal cations in substituted LaCoO_3 on mixed conductivity and oxygen permeability". In: *Solid State Ionics* 48.3 (1991).

- [39] J. Hayd, L. Dieterle, U. Guntow, D. Gerthsen, and E. Ivers-Tiffee. "Nanoscaled $\text{La}_{0.6}\text{Sr}_{0.4}\text{CoO}_{3-\delta}$ as intermediate temperature solid oxide fuel cell cathode: Microstructure and electrochemical performance". In: *Journal of Power Sources* 196.17 (2011).
- [40] A.R. West. *Solid State Chemistry and its applications*. John Wiley and Sons Ltd, 2014.
- [41] K. Momma and F. Izumi. "VESTA: a three-dimensional visualization system for electronic and structural analysis". In: *Journal of Applied Crystallography* 41 (2008).
- [42] M. A. Peña and J. L. G. Fierro. "Chemical Structures and Performance of Perovskite Oxides". In: *Chemical Reviews* 101.7 (2001).
- [43] J. Mastin, M. A. Einarsrud, and T. Grande. "Structural and thermal properties of $\text{La}_{1-x}\text{Sr}_x\text{CoO}_{3-\delta}$ ". In: *Chemistry of Materials* 18.25 (2006).
- [44] R. D. Shannon. "Revised effective ionic-radii and systematic studies of interatomic distances in halides and chalcogenides". In: *Acta Crystallographica Section A* 32 (1976).
- [45] M. Kumar, S. Srikanth, B. Ravikumar, T. C. Alex, and S. K. Das. "Synthesis of pure and Sr-doped LaGaO_3 , LaFeO_3 and LaCoO_3 and SrMg-doped LaGaO_3 for ITSOFC application using different wet chemical routes". In: *Materials Chemistry and Physics* 113.2-3 (2009).
- [46] Andre Heel, Peter Holtappels, and Thomas Graule. "On the synthesis and performance of flame-made nanoscale $\text{La}_{1-x}\text{Sr}_x\text{CoO}_{3-\delta}$ and its influence on the application as an intermediate temperature solid oxide fuel cell cathode". In: *Journal of Power Sources* 195.19 (2010).
- [47] N. Orlovskaya, K. Kleveland, T. Grande, and M. A. Einarsrud. "Mechanical properties of LaCoO_3 based ceramics". In: *Journal of the European Ceramic Society* 20.1 (2000).
- [48] M. Prestat, A. Morandi, A. Heel, L. Holzer, P. Holtappels, and T. J. Graule. "Effect of graphite pore former on oxygen electrodes prepared with $\text{La}_{1-x}\text{Sr}_x\text{CoO}_{3-\delta}$ nanoparticles". In: *Electrochemistry Communications* 12.2 (2010).
- [49] J. Hayd, L. Dieterle, U. Guntow, D. Gerthsen, and E. Ivers-Tiffee. "Nanoscaled $\text{La}_{1-x}\text{Sr}_x\text{CoO}_{3-\delta}$ as intermediate temperature solid oxide fuel cell cathode: Microstructure and electrochemical performance". In: *Journal of Power Sources* 196.17 (2011).
- [50] R. Kiebach, W. W. Zhang, W. Zhang, M. Chen, K. Norrman, H. J. Wang, J. R. Bowen, R. Barfod, and P. Y. Hendriksen. "Stability of $\text{La}_{0.6}\text{Sr}_{0.4}\text{Co}_{0.8}\text{Fe}_{0.2}\text{O}_3/\text{Ce}_{0.9}\text{Gd}_{0.1}\text{O}_2$ cathodes during sintering and solid oxide fuel cell operation". In: *Journal of Power Sources* 283 (2015).

- [51] Z. P. Li, M. Toshiyuki, G. J. Auchterlonie, J. Zou, and D. John. "Mutual Diffusion Occurring at the Interface between $\text{La}_{0.6}\text{Sr}_{0.4}\text{Co}_{0.8}\text{Fe}_{0.2}\text{O}_3$ Cathode and Gd-doped Ceria Electrolyte during IT-SOFC Cell Preparation". In: *Acs Applied Materials & Interfaces* 3.7 (2011).
- [52] Y. K. Tao, J. Shao, J. X. Wang, and W. G. Wang. "Synthesis and properties of $\text{La}_{1-x}\text{Sr}_x\text{CoO}_{3-\delta}$ nanopowder". In: *Journal of Power Sources* 185.2 (2008).
- [53] K. C. Anjaneya, G. P. Nayaka, J. Manjanna, G. Govindaraj, and K. N. Ganesha. "Preparation and characterization of $\text{Ce}_{1-x}\text{Gd}_x\text{O}_{2-\delta}$ ($x = 0.1-0.3$) as solid electrolyte for intermediate temperature SOFC". In: *Journal of Alloys and Compounds* 578 (2013).
- [54] R. K. Lenka, T. Mahata, A. K. Tyagi, and P. K. Sinha. "Influence of grain size on the bulk and grain boundary ion conduction behavior in gadolinia-doped ceria". In: *Solid State Ionics* 181.5-7 (2010).
- [55] G. L. Messing, S. C. Zhang, and G. V. Jayanthi. "Ceramic Powder Synthesis by Spray-Pyrolysis". In: *Journal of the American Ceramic Society* 76.11 (1993).
- [56] R. Moen. "Spraypyrolyse av keramiske oksidmaterialer". MA thesis. Norwegian University of Science and Technology, NTNU, 2013.
- [57] D.F. Shriver, P.W. Atkins, T. L. Overton, J.P. Rourke, M. T. Weller, and F. A. Armstrong. *Inorganic Chemistry*. Fourth. Oxford University Press, 2006.
- [58] G. Schwarzenbach. "The General, Selective, and Specific Formation of Complexes by Metallic Cations". In: *Advances in Inorganic Chemistry* 3 (1961).
- [59] A. Ringbom. *Complexation in Analytical Chemistry*. Interscience publishers, 1963.
- [60] M. Nic, J. Jirat, and B. Kosata. *IUPAC. Compendium of Chemical Terminology, 2nd ed. (the "Gold Book")*. 2014. URL: <http://goldbook.iupac.org/C01012.html> (visited on 07/06/2016).
- [61] David. W. Richerson. *Modern Ceramic Engineering*. CRC Press, 2006.
- [62] T. Tadros. "Electrostatic and steric stabilization of colloidal dispersions". In: *Electrical Phenomena at Interfaces and Biointerfaces: Fundamentals and Applications in Nano-, Bio-, and Environmental Sciences*. Ed. by H. Ohshima. John Wiley & Sons, 2012.
- [63] Ayouril. *Electro-steric stabilization*. URL: https://commons.wikimedia.org/wiki/File:Electro-Steric_Stabilization.jpg (visited on 07/07/2016).
- [64] B.D. Cullity. *Elements of X-ray Diffraction*. Addison-Wesley metallurgy series. Addison Wesley Publishing Company, 1956.
- [65] B. Kjeldby. "Effect of Firing Temperature on the Kinetics of Oxygen Reduction in $\text{La}_{0.6}\text{Sr}_{0.4}\text{Co}_{0.2}\text{Fe}_{0.8}\text{O}_{3-\delta}$ (LSCF) Cathodes for Solid Oxide Fuel Cells". MA thesis. Norwegian University of Science and Technology, NTNU, 2015.

- [66] NorECs. *Probostat*. URL: <http://www.norecs.com/index.php?page=ProboStat> (visited on 07/07/2016).
- [67] G. V. Jayanthi, S. C. Zhang, and G. L. Messing. "Modeling of solid particle formation during solution aerosol thermolysis - The evaporation stage". In: *Aerosol Science and Technology* 19.4 (1993).
- [68] C. Chen, T. K. Tseng, S. C. Tsai, C. K. Lin, and H. M. Lin. "Effect of precursor characteristics on zirconia and ceria particle morphology in spray pyrolysis". In: *Ceramics International* 34.2 (2008).

Appendix A

Element maps

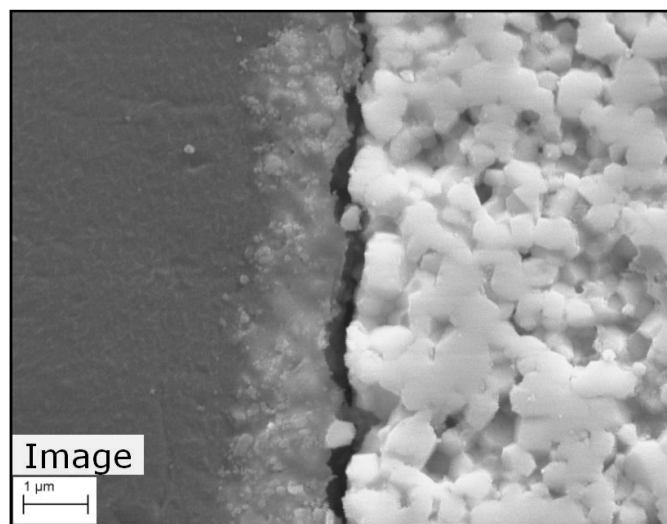
This appendix present element maps recorded by energy-dispersive X-ray spectroscopy as described below.

Symmetric cells with $(\text{La}_{0.6}\text{Sr}_{0.4})_{0.99}\text{CoO}_3$ cathodes on $\text{Ce}_{0.8}\text{Gd}_{0.2}\text{O}_2$ electrolytes were fabricated by spray deposition and fired at various temperature programs. The cross section of the symmetric cells were investigated by energy-dispersive X-ray spectroscopy. The recorded element maps can be seen in Figures A.1, A.2, and A.3, for symmetric cells fired at 700 °C with no hold time, 700 °C for 1 hour, and 800 °C with no hold time, respectively.

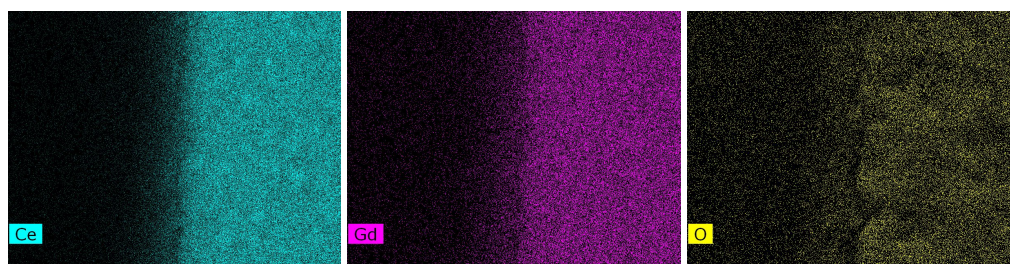
The images were recorded using a Zeiss Ultra, 55 Limited Edition FESEM, employing the secondary electron detector with an accelerating voltage of 20 kV, an aperture of 120 μm , and a working distance of 10 mm.

Image (a) shows the area of the cross section that was mapped. Image (b) and (c) shows the distribution of the elements cerium and gadolinium, respectively. These are mostly located in the electrolyte. Image (d) shows oxygen, which is distributed across the entire cell. Image (e), (f), and (g) are of the elements in the cathode; lanthanum, strontium, and cobalt, respectively.

The cathode appears as a uniform layer in each of the images and there is no indication of the formation of any secondary phases at the interface for any of the investigated samples.



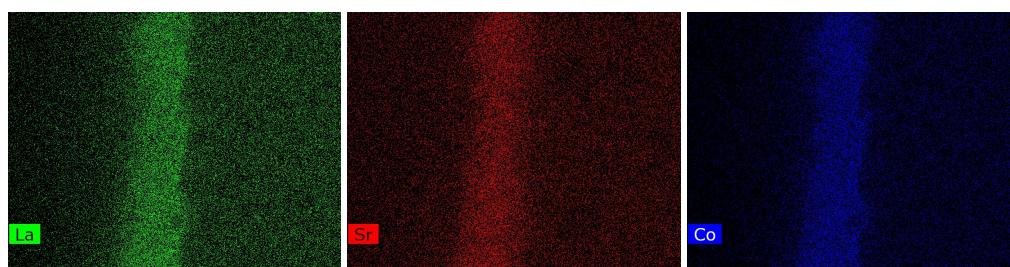
(a)



(b)

(c)

(d)



(e)

(f)

(g)

FIGURE A.1: Element map for the cross section of a symmetric cell of $(\text{La}_{0.6}\text{Sr}_{0.4})_{0.99}\text{CoO}_3$ cathodes on $\text{Ce}_{0.8}\text{Gd}_{0.2}\text{O}_2$ electrolytes fired at 700°C with no hold time.

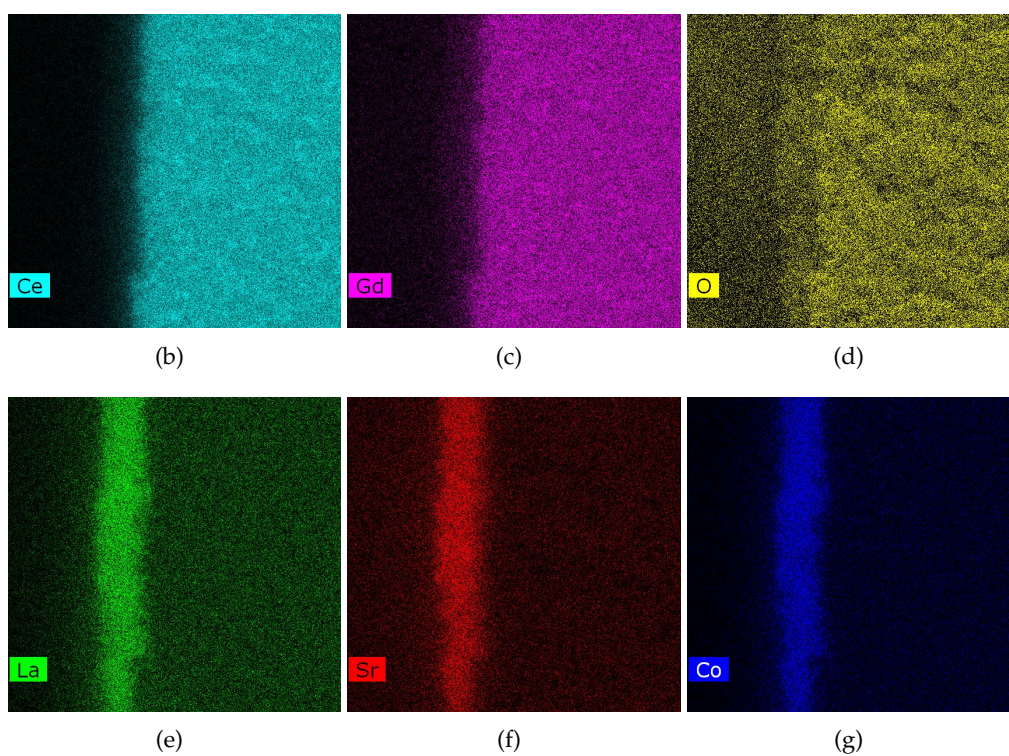
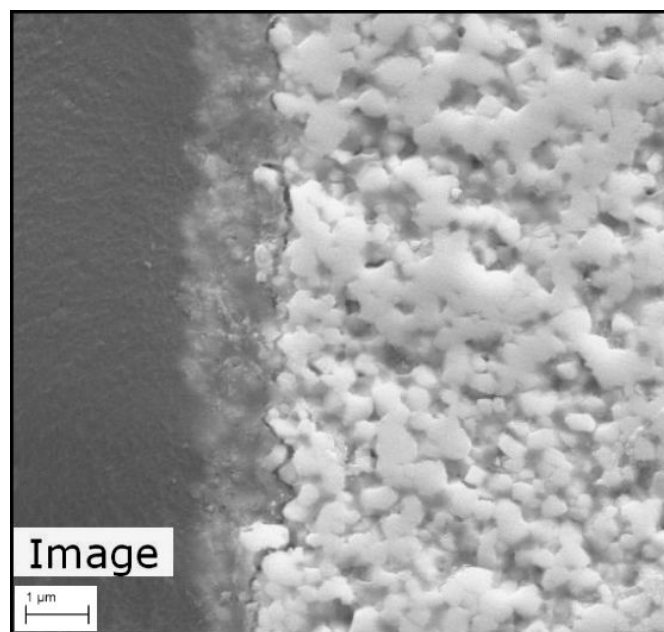


FIGURE A.2: Element map for the cross section of a symmetric cell of $(\text{La}_{0.6}\text{Sr}_{0.4})_{0.99}\text{CoO}_3$ cathodes on $\text{Ce}_{0.8}\text{Gd}_{0.2}\text{O}_2$ electrolytes fired at 700 $^\circ\text{C}$ for 1 hour.

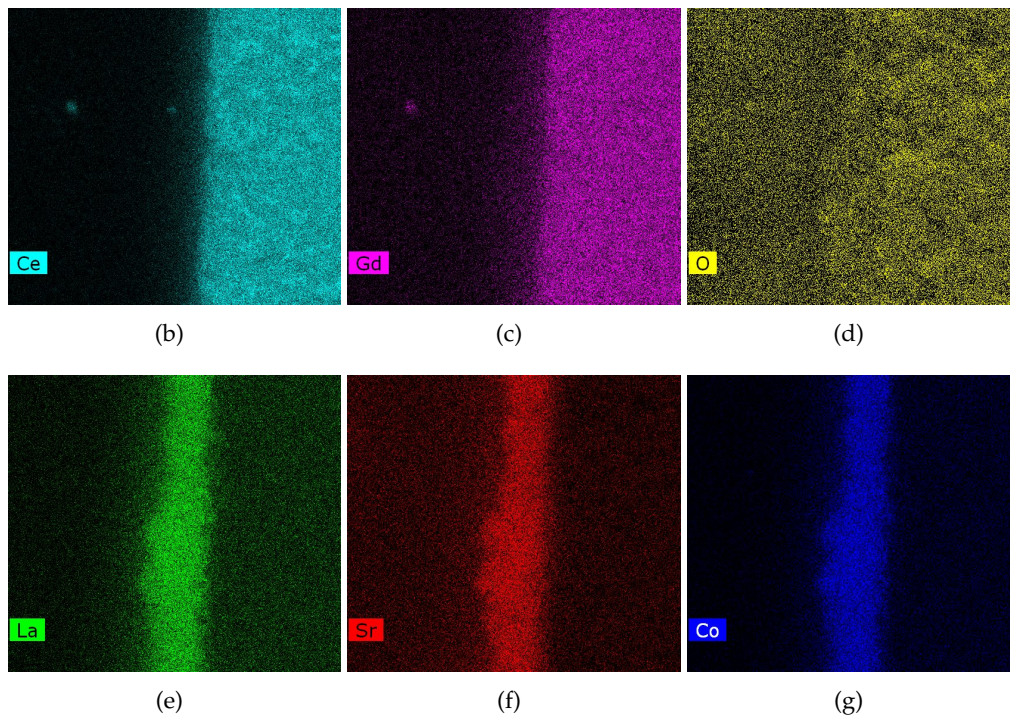
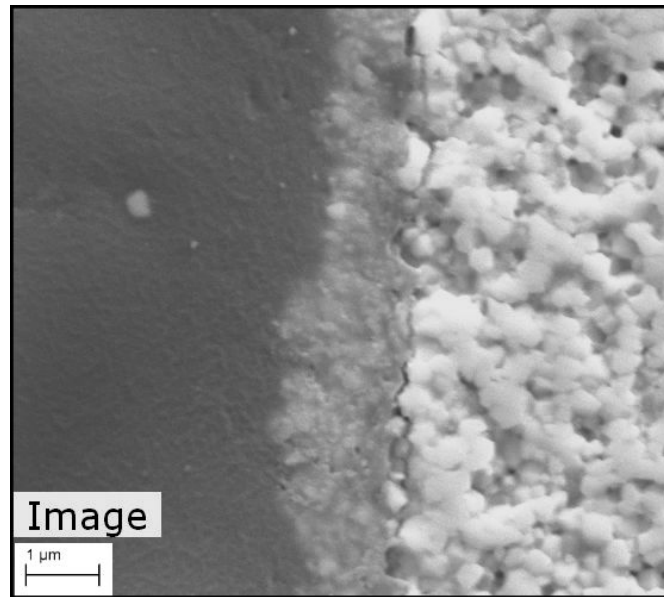


FIGURE A.3: Element map for the cross section of a symmetric cell of $(\text{La}_{0.6}\text{Sr}_{0.4})_{0.99}\text{CoO}_3$ cathodes on $\text{Ce}_{0.8}\text{Gd}_{0.2}\text{O}_2$ electrolytes fired at $800\text{ }^\circ\text{C}$ with no hold time.

Appendix B

Non-normalised Nyquist plots

This appendix shows the non-normalised Nyquist plots for the electrochemical impedance data recorded for a symmetric cell of a $(\text{La}_{0.6}\text{Sr}_{0.4})_{0.99}\text{CoO}_3$ cathode on a $\text{Ce}_{0.8}\text{Gd}_{0.2}\text{O}_2$ electrolyte. The symmetric cell was fired at 800 °C with heating/cooling rate of 3.33 °C/min and immediately cooled. The impedance measurements were conducted in oxygen, at 600, 700, and 800 °C with the respective Nyquist plots in Figure B.1, B.2, and B.3.

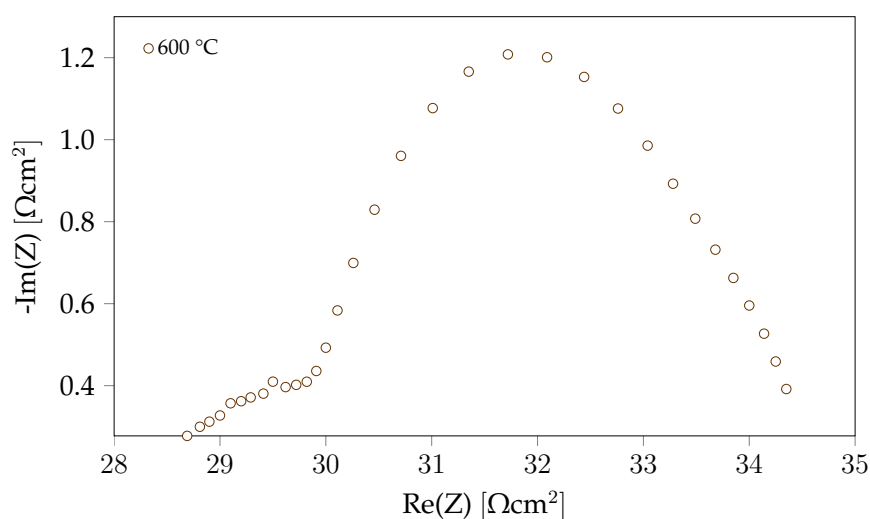


FIGURE B.1: Electrochemical impedance data for a symmetric cell of a $(\text{La}_{0.6}\text{Sr}_{0.4})_{0.99}\text{CoO}_3$ cathode on a $\text{Ce}_{0.8}\text{Gd}_{0.2}\text{O}_2$ electrolyte, recorded at 600 °C in pure oxygen. The symmetric cell was fired at 800 °C with no hold time.

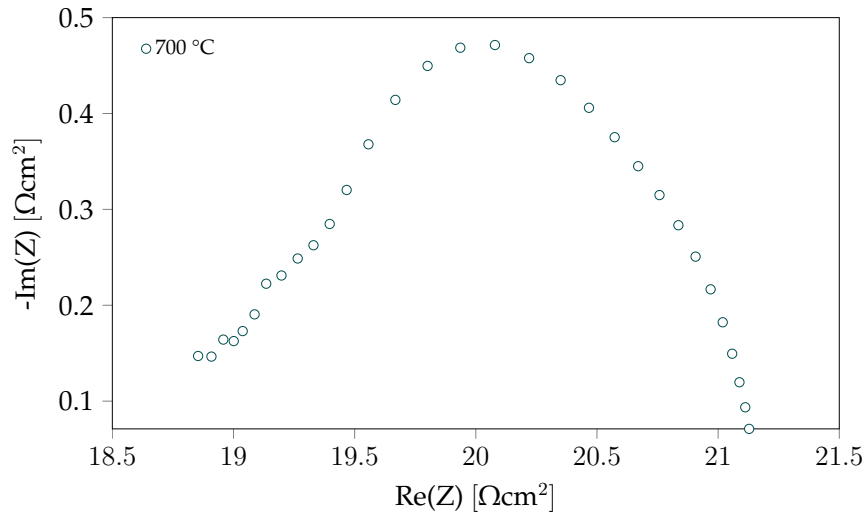


FIGURE B.2: Electrochemical impedance data for a symmetric cell of a $(\text{La}_{0.6}\text{Sr}_{0.4})_{0.99}\text{CoO}_3$ cathode on a $\text{Ce}_{0.8}\text{Gd}_{0.2}\text{O}_2$ electrolyte, recorded at 700 °C in pure oxygen. The symmetric cell was fired at 800 °C with no hold time.

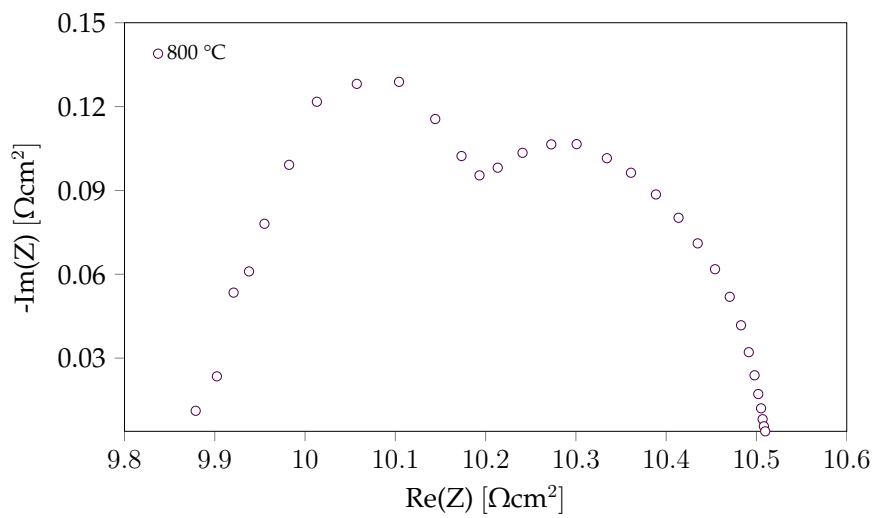


FIGURE B.3: Electrochemical impedance data for a symmetric cell of a $(\text{La}_{0.6}\text{Sr}_{0.4})_{0.99}\text{CoO}_3$ cathode on a $\text{Ce}_{0.8}\text{Gd}_{0.2}\text{O}_2$ electrolyte, recorded at 800 °C in pure oxygen. The symmetric cell was fired at 800 °C with no hold time.

Appendix C

Impedance data modelled by equivalent circuits

This appendix shows the comparison of the measured impedance data and the fit obtained by modelling the equivalent circuit in Figure C.1. L1 represents the inductance of the equipment used for the measurements. Rs is the resistance that can be attributed to the electrolyte and includes ohmic losses. R1 and R3 represent resistances from the chemical processes in the electrodes. Finally, CPE1 and CPE3 represents the complex capacitance of the model.

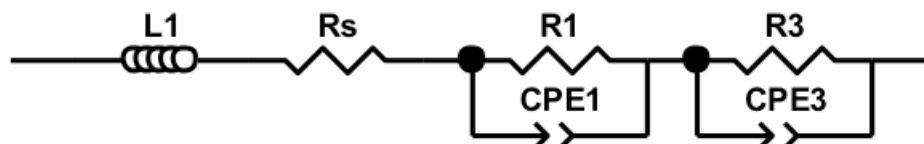


FIGURE C.1: Schematic of the equivalent circuit used to model the impedance response measured for the symmetric cells.

The impedance data was measured for a symmetric cell of a $(\text{La}_{0.6}\text{Sr}_{0.4})_{0.99}\text{CoO}_3$ cathode on a $\text{Ce}_{0.8}\text{Gd}_{0.2}\text{O}_2$ electrolyte. The symmetric cell was fired at 800 °C with heating/cooling rate of 3.33 °C/min and immediately cooled. The impedance measurements were conducted in oxygen, at 600, 700, and 800 °C

The fitted data is shown in Figures C.2, C.3, and C.4 for the measurements at 600, 700, and 800 °C, respectively. The equivalent circuit used to model the data appears to be a good fit in all figures.

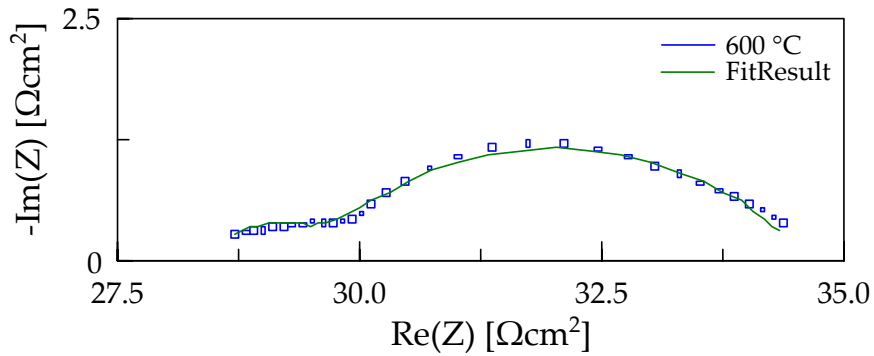


FIGURE C.2: Comparison of the measured impedance data and the fit obtained using an equivalent circuit. The data were measured at 600 °C, for the symmetric cell fired at 800 °C with no hold time.

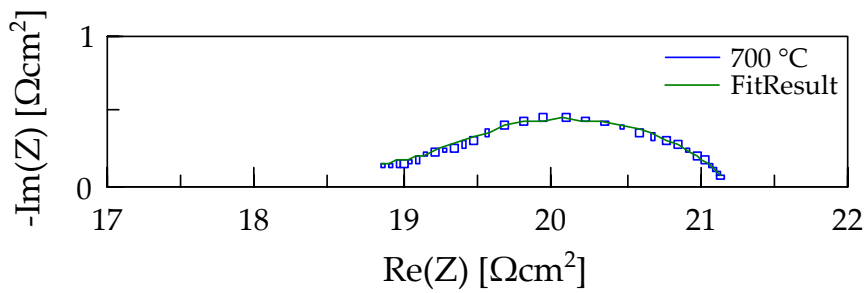


FIGURE C.3: Comparison of the measured impedance data and the fit obtained using an equivalent circuit. The data were measured at 700 °C, for the symmetric cell fired at 800 °C with no hold time.

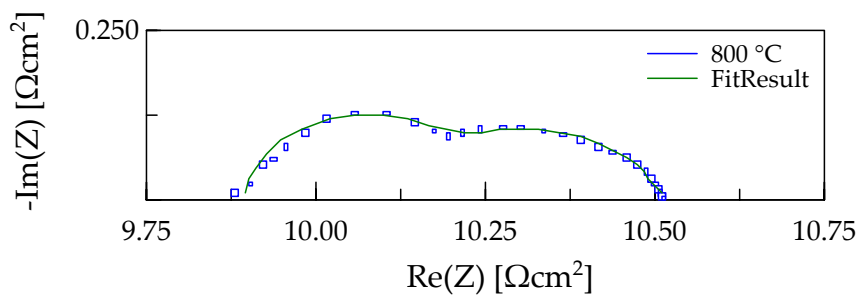


FIGURE C.4: Comparison of the measured impedance data and the fit obtained using an equivalent circuit. The data were measured at 800 °C, for the symmetric cell fired at 800 °C with no hold time.